FAULT DIAGNOSIS OF PERMANENT MAGNET SYNCHRONOUS MOTOR BASED ON MECHANICAL AND MAGNETIC CHARACTERISTIC ANALYSES

YU YINQUAN

NATIONAL UNIVERSITY OF SINGAPORE

2013

FAULT DIAGNOSIS OF PERMANENT MAGNET SYNCHRONOUS MOTOR BASED ON MECHANICAL AND MAGNETIC CHARACTERISTIC ANALYSES

YU YINQUAN

A THESIS SUBMITTED

FOR THE DEGREEM OF DOCTOR OF PHILOSOPHY

DEPARTMENT OF ELECTRICAL AND COMPUTER ENGINEERING

NATIONAL UNIVERSITY OF SINGAPORE

2013

Declaration

I hereby declare that the thesis is my original work and it has been written by me in its entirety. I have duly acknowledged all the sources of information which have been used in the thesis.

This thesis has also not been submitted for any degree in any university previously.

YU YINQUAN

YU YINQUAN

26 December 2013

ABSTRACT

Thanks to the developments of functional materials, power electronics and electrical machine design, the permanent magnet synchronous motor (PMSM) has been used widely in different areas e.g. hard disk drives (HDDs). As its high efficiency and high power density, the PMSM will replace more and more other types of motors in the future. Therefore, in the PMSM research, the pursuit to develop effective diagnostic technology to judge the performance of PMSM is a concern and hot research topic.

The reasons inducing the vibration in the PMSM operation can be categorized into electromagnetic (EM) and mechanical ones. The former could be induced by the unreasonable EM structure, the unreasonable drive modes and the quality of the EM components e.g. winding, magnet, and power electronics, all three of which induce the torque ripple and unbalance-magnetic-pull in the motor operation. The latter could be induced by the quality of bearings, magnets, shaft, rotor and stator yoke of the motor and by problems in the motor assembling. The patterns of the vibration should be different for various EM and mechanical roots. As well known, vibration measurements of the external surface of a machine contain much information on the internal processes and have become an established method of judging the state of the machine. The PMSM internal working state could be checked and predicted by the vibration signal patterns. In the past couple of decades, efforts have been made to derive an effective technique to diagnose motor faults. However, the processing of obtaining the precise fault classifications and predictions remains a challenging task in engineering practice.

This thesis aims to reveal the main vibration consequences induced by the electromagnetic and mechanical interaction in the PMSM. Another goal is to develop a simple and easy-to-implement method to diagnose faults and performances of the PMSM based on the analysis of the EM, of the rotor-dynamics and of the resultant output thus generated, i.e. vibration. In this thesis, two classes of modeling approaches, i.e. analytical model based approach and numerical model approach are applied for the modeling of different types of faulty PMSMs. For the analytical model based approaches, a lumped mass method and a gradient field method are used for mechanical vibration modeling and electrical Unbalanced Magnetic Pull (UMP) modeling respectively. With reference to the lumped mass method, a mechanical parametric model is derived by combining the Jeffcott rotor model with the flexible support model. Whereas, with reference to the gradient field method, four electrical parametric models are derived for UMPs induced by four types of motor faults. For the numerical model approach, the three-dimensional finite element method is adopted in the study of magnetic field distributions and evaluation of the UMPs and UMP-induced vibration under different types of faulty motors. To obtain experimental results, five types with four grades of fault motors were designed and fabricated. Simulation and experimental results verify the effectiveness of the derived parametric models for achieving high accuracy and their respective advantages. With well-studied fault roots and judicious selection of fault features for different types of faulty motors, a classification algorithm could be successfully employed to classify the healthy motors and different types of faulty motor in the future.

A computer simulation platform and an experimental testing platform for the PMSM vibration analysis are developed. The vibration models of the motor are analyzed in the

simulation platform and verified through the testing platform. These platforms can be used to analyze the existing PMSM products and will also play an important role in the PMSM design. As a result, PMSM development cycle time can be shortened, the developmental cost can be reduced, and the quality of the PMSM can be improved.

ACKNOWLEDGEMENTS

I would like to express my profound gratitude and high regards to Adjunct Associate Prof. **Chao BI** from Data Storage Institute, A-star, Singapore and Associate Prof. **A. Al. Mamun** from the department of Electrical Computer Engineering, National University Singapore. Their encouragement, friendship and suggestions during the course of this Research experiment have played a vital role; it is my adjective honor to be under their supervision.

I would like to express the feeling of gratitude to Dr. Quan Jiang, Dr. Song Lin, Dr. Hla Nu Phyu and Mr. Nay Lin Htun Aung for their support and cooperation. My appreciation also goes to all the staffs in our motor group in Data Storage Institute who helped me one way or another.

Finally, I wish to express my heartfelt gratitude to my parents, for their affection and support. I would like to thank my wife, Yang Cunyu, for her constant support and encouragement. Last but not at least, I would like to thank my two lovely kids, Yu Shijie and Yu Shihui for their self-discipline and well handling their study in these years. I will never fulfill myself without my loving family. I dedicate this thesis to them.

Contents

List of tables

List of Tables

List of Figures

List of Figures

List of Figures

List of Acronyms

AE	Axial Eccentricity
AUMP	Axial Unbalanced Magnetic Pull
CAD	Computer Aided Design
CAE	Computer Aided Engineering
DC	direct current
DE	dynamic eccentricity
DFT	discrete Fourier transform
DSA	dynamic signal analyzer
DUMP	Dynamic Unbalanced Magnetic Pull
EM	electromagnetic
FEA	Finite Element Analysis
FEM	Finite Element Method
FFT	fast Fourier transform
FT	Fourier transform
HDD	hard disk drive
IE	Inclined Eccentricity
IUMP	Inclined Unbalanced Magnetic Pull
LCF	low cycle fatigue
LDV	Laser Doppler velocimetry

ME	Mechanical Eccentricity
MEC	Magnetic Equivalent Circuit
MMF	magnetic-motive-force
MU	Mechanical Unbalance
NRRO	non-repeatable runout
PWM	Pulse-width modulation
RPM	Revolutions Per Minute
RRO	repeatable runout
SE	Static Eccentricity
STFT	Short-Time Fourier Transform
SUMP	Static Unbalanced Magnetic Pull
UMP	Unbalanced Magnetic Pull
VSI	Voltage-source-inverter

CHAPTER 1

INTRODUCTION

1.1 Background

The first electric motors were invented independently in 1831 by the British physicist Michael Faraday and the American scientist Joseph Henry. Today, most electric motors, like the first electric motors, are still based on electromagnetic reaction principle. However, with the rapid development of electromagnetic materials, power electronics, digital technology and computer technology, motor technology has been undergoing dramatic changes and development in recent years.

Currently, rotating electrical machines generate almost all of the world's electricity. It is estimated that rotating machines (motors) consume approximately 70 percent of all electrical power [1]. Given the fact that the most of the moving parts of equipment are driven by different types of electrical motors, such motors are prevalent in our life. However, electric generators or motors also generate heat, vibration, and acoustic noise while converting either electrical power to mechanical power (motors) or vice versa (generators). Such phenomena would gradually turn the motor or generator condition into a faulty one. Eventually, the whole rotating system could break down, leading to the necessity of maintenance. In this thesis, the Permanent Magnet Synchronous Motor (PMSM) will be analyzed for diagnosis. This kind of motor has been widely used in many areas, especially in high-end products like hard disk drive

(HDD), generators, medical devices and defense-related products. The PMSM is also playing an important role in the area of green energy, and is replacing the traditional induction motor in an increasing number of products. Green concept elevator has been proposed by TOSHIBA, they designed a compact Permanent Magnet Synchronous Motor for space saving. They claimed that compared to conventional electric motor, Over 30 percent lower in power consumption [2]. Electric Vehicle (EV) is a dream for our city traffic without exhausting greenhouse gas and with low noise. Permanent magnet synchronous motor (PMSW) became at the top of AC motors in high performance drive systems of EV [3]. The main advantages of the PMSM are high efficiency, high power density, low noise, and good reliability.

1.1.1 Common motor faults

Some malfunction of PMSM components may occur after the motor has worked for a certain period of time. In this case, the motor may still work, but with low efficiency, over-heating, large vibration and loud acoustic noise. The motor fault can be classified by the following motor states or motor causes.

a) Motor fault classified by running state

- ✓ The motor cannot be started.

  This phenomenon may be caused by electrical or mechanical faults. The electrical faults could be induced by unhealthy driver, motor stator unhealthy winding, and/or unhealthy magnetic components; the mechanical faults include overload, i.e., load torque is larger than the motor starting torque.

- ✓ The motor is over-heating.

  This problem is mainly caused by overloading or unhealthy winding. Another possible reason for over-heating is the presence of a motor cooling system

fault or motor phase circuit open fault. In order to avoid damaging the motor by over-heating, the temperature of motor and the crack of rotor blade should be monitored.

- ✓ The motor has abnormal acoustic noise.

  The problem usually comes from the bearing used to support the rotor. If the ball bearing is used, due to wear and tear, the gap between the bearing's inner and outer races becomes too large. This enlarged gap sharply increases the motor vibration and generates abnormal acoustic noise. If the fluid dynamic bearing (FDB) is used, acoustic noise may be induced by mechanical contact between the inner and outer races.

b) Motor faults classified by causes

The causes of motor fault can be classified by the fault in each portion of the motor. A flowchart is displayed in Figure 1.1.

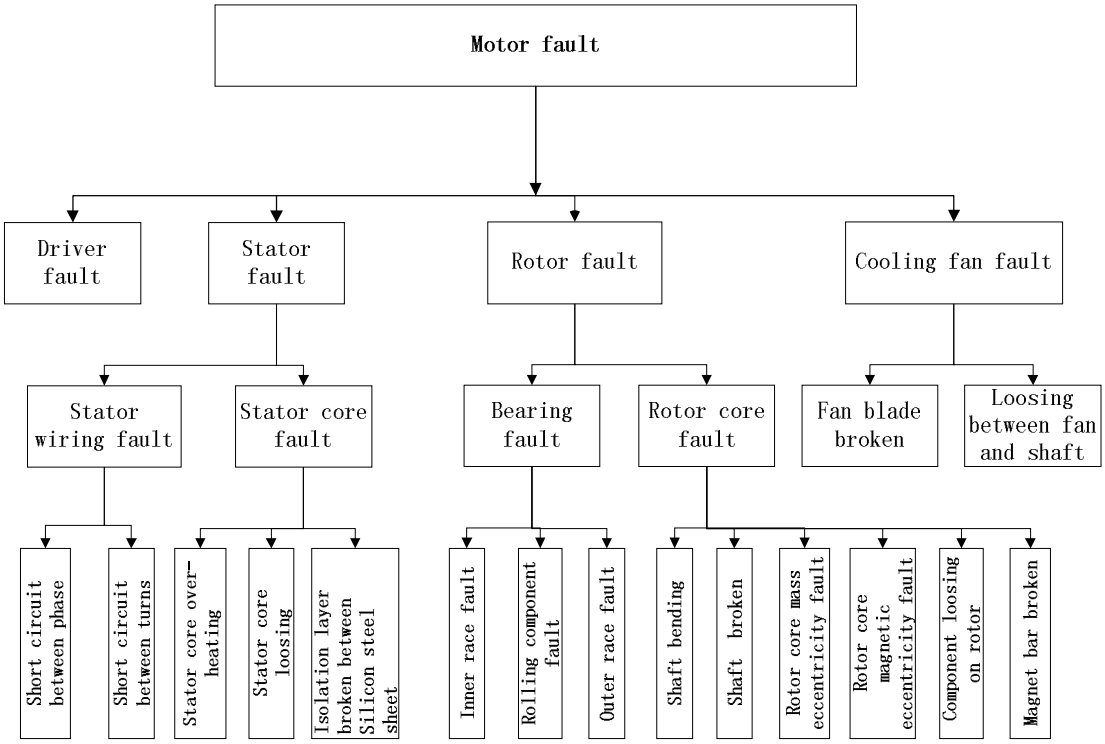

Figure 1.1: Motor fault types

1.1.2 Motor fault study methodologies

The main objective of motor fault analysis is to clarify the relationship between the motor fault reasons and the motor diagnostic features. The methodology used can be categorized into analytical, numerical and experimental methods.

- ✓ The analytical method uses mathematical models to predict the fault with the electric machine and the mechanical theories.
- ✓ The numerical method is adopted by using numerical technology to simulate the motor fault. The geometry of a faulty motor can be built using commercial Computer Aided Design (CAD) softwares, such as ProE®, AutoCad®, Unigraph® (UG), and Solidworks®. Subsequently, the geometry is imported to finite software, such as Ansys® or Ansoft® or other Computer Aided Engineering (CAE) software, which can be used to calculate motor electromagnetic (EM) induced vibration, such as Unbalanced Magnetic Pull (UMP), cogging torque, and back EMF based on the motor design parameters. The EM characteristics calculated will be imported to classical CAE software to simulate the fault motor vibration and other features, based on the EM and mechanical characteristics. The numerical method is popularly used by researchers due to its advantages as shown below:
  - ❖ It is easy to use and the user does not need to know the working principle behind the simulation model and numerical technology.
  - ❖ The numerical method is normally cheaper than the experimental method as the former does not need equipment for setting up an experimental system and construction of fault motor prototype.

- ✓ The experimental method is adopted by using an experimental design and setup to study the cause and relationship between motor fault root and performance. The advantage of this method is that the real case diagnostic feature can be obtained after using proper signal processing technologies, such as spectrum analysis for steady state analyses and Short-Time Fourier Transform (STFT) for transient state analyses. However, one of the disadvantages of experimental method is that it could be expensive and time consuming, and need the manpower in all the steps of the experiment.

In this thesis, all three methods are utilized in order to fully understand the motor cause-effect relationship, and to select correct diagnostic features to perform motor fault type classification. The analytical method is used to calculate natural frequencies of the PMSM in mechanical domain and different types of UMPs in electromagnetic (EM) domain. The analytical results can expose clearly the relationship between the vibration induced by different types of UMPs and motor fault types. These results can also be used as first-time motor design guidelines. The analytical results are validated by the simulation results obtained by numerical methods, e.g., finite element method. By using the numerical method to simulate known motor dimension and material properly, it can be observed that the simulation results are more accurate than the analytical results because the nonlinear effect is also considered during the calculation. Simulation results can finally be validated by the experimental ones.

1.1.3 Motor fault sensor selection and positioning

Experiment is necessary in the study of fault analysis and fault classification. Therefore, selecting the reasonable sensors to detect the fault signal is important. The

commonly-used sensors to monitor the motor vibration are accelerometer and Laser Doppler Vibrometer (LDV).

1.1.4 Motor fault signal processing technologies

Fault signal processing is necessary in the fault analysis as the signal obtained is normally contaminated by a lot of sources. The aim of the motor fault signal processing is to extract the useful information from the original time domain signal and filter out the signal noise. The ones used to do the motor healthy condition monitoring and fault diagnosis include mean calculation, variance calculation, skewness calculation, and intensity calculation. Frequency domain signal processing technologies are also used to do the fault type classification.

- Fourier transform

According to the Fourier transform, any periodic waveform can be decomposed into a series of sine and cosine waves. The general expression is expressed as:

$$g(t) = \sum_{n=0}^{\infty} A_n \cos\left(\frac{2\pi nt}{T}\right) + \sum_{n=0}^{\infty} B_n \sin\left(\frac{2\pi nt}{T}\right), \quad (1.1)$$

where T is the fundamental period.

Visualizing a signal in the frequency domain offers many benefits. Frequency domain representations allow individual frequency components contained within a signal to be viewed, including modulation sidebands, distortion effects and spurious frequency components.

- Discrete Fourier transform

The discrete Fourier transform (DFT) takes finite samples of a signal and transforms them into finite frequency samples of that signal.

The Fourier transform is applied to continuous-time signals. The DFT can be applied to signals that exist at finite time points.

The DFT produces a discrete frequency spectrum, i.e. amplitude levels at discrete frequencies, or "frequency bins". The DFT is defined as:

$$x(f) = \sum_{n=0}^{N} X(n) e^{-j\frac{2\pi fn}{f_s}}, \tag{1.2}$$

where N is the total number of samples taken from the original signal. Essentially, this equation uses the value, x, of the N samples to calculate the amplitude, X, of the signal at the k^{th} discrete frequency bin. The total frequency spectrum is constructed from all these values over the whole frequency range.

❖ Fast Fourier Transform

The fast Fourier transform (FFT) is a faster version of the DFT [4]. The FFT utilizes some smart algorithms to serve the same function as the DTF, but in much less time. In fact, the FFT is a development of the DFT, and removes duplicated terms in the mathematical algorithm to reduce the number of mathematical operations performed. Furthermore, the FFT is an efficient algorithm to compute the discrete DFT and its inverse. FFTs are of great importance to a wide variety of applications, including digital signal processing, the solving of partial differential equations, and algorithms for quickly multiplying large integers. Let $x_0, \ldots, x_{N-1}$ be complex numbers. The DFT is defined by the formula:

$$X_k = \sum_{n=0}^{N-1} X_n e^{-\frac{2\pi i}{N} nk}. \qquad K = 1,....N-1 \tag{1.3}$$

Evaluating these sums directly would take N^2 arithmetical operations. An FFT is an algorithm to compute the same result in only $N/log(N)$ operations. In general, such algorithms depend upon the factorization of N, but (contrary to popular misconception) there are $N/log(N)$ FFTs for all N, even prime N.

In this way, it is possible to use large numbers of samples without compromising the speed of the transformation. The FFT reduces computation by a factor of $(N/2)log2(N)$ [5].

- FFT base waterfall

The FFT base waterfall uses FFT methodology to plot the drawing either in a different time periods or at different speeds. In this thesis, the FFT base waterfall technology is used with different motor running speeds to obtain the fault data signals. These signals are used to diagnose the motor faults.

1.2 Outline of this thesis

Chapter 2, presents a review of different types of motor faults and diagnosis technologies. The rotor mechanical unbalance fault has been studied in numerous papers because it is a common fault due to machine tolerance. Other types of motor faults such as Unbalanced Magnetic Pulls (UMPs) have also been extensively studied. Besides the motor faults itself, studies on the motor with external load faults will also be reviewed in Chapter 2. The current signal shows the global motor performance effect and can be used to diagnose whether a motor is faulty or otherwise. However, it cannot indicate the fault position precisely. The vibration signal can show local effect,

and motor fault type and fault position can be indicated precisely. Numerous studies have been done on the motor fault analysis using vibration signals. Mathematical Model of Permanent Magnet Synchronous Motor (PMSM) is developed in Chapter 3. In Chapter 4, analytical equations for different excitation forces are interpreted, such as Mechanical Unbalance (MU), Static Unbalanced Magnetic Pull (SUMP), Dynamic Unbalanced Magnetic Pull (DUMP), Inclined Unbalanced Magnetic Pull (IUMP), and Axial Unbalanced Magnetic Pull (AUMP). In Chapter 5, the numerical models of different electromagnetic forces have been developed and the numerical results of different types of UMPs are analyzed. In Chapter 6, motor critical running frequency and the frequencies with forward and backward whirls are calculated by finite element method. The modal frequencies and modal shapes of the motor are also obtained by numerical analysis. These numerical results are compared with those analytical results in Chapter 3. In Chapter 6, the motor vibration responses under different types of motor eccentricity faults are also studied by using numerical transition analysis. These numerical results are verified by experimental measurement results in the following chapter. In Chapter 7, experimental platforms have been developed to verify the analytical and numerical fault models developed. Conclusions from this thesis are drawn and future works are discussed in Chapter 9. The procedure to calculate Inclined Unbalance Magnetic Pull is presented in Appendix A. Based on the analytical fault models developed, the fault of motor blade, which is one of important common parts used to cool the motor temperature, is studied in Appendix B. The cracks of the blade with different crack sizes are simulated, and the experimental design and measurement results are presented.

CHAPTER 2

LITERATURE REVIEW

2.1 Review of techniques for Mechanical Unbalance

Mechanical Unbalance (MU) in a rotating machine is a condition of unequal mass distribution at each section of the rotor [6]. When the unbalanced machine is rotating, the rotor mass centre does not coincide with the rotating axis and the eccentric force is generated on the rotor. Vibration and stress are induced in the rotor itself and in its supporting structure, which may gradually lead to excessive wear in the joints: bearings, bushings, shafts and spindles. Eventually, the whole system may break down. This is a very common malfunction in rotating machines. Vibrations due to one machine's mechanical unbalance may be transmitted through two paths. Firstly, it is through the floor to adjacent machinery and seriously impairs its accuracy or proper functioning. Secondly, it is through either the machine structure or the air to generate structure borne or air borne acoustic noise. Both decrease the machine's performance and the quality of the working environment.

Several researchers have studied rotor unbalance in rotating machines in recent years. Sudhakar and Sekhar [7] proposed equivalent loads minimization and vibration minimization method to apply for the identification of unbalance fault in a rotor system. Huang [8] studied the characteristics of torsion vibrations of an unbalanced

shaft using the numerical method, and the numerical results are agreeable with the experimental results. Concari et al. [9] proposed a method to discern mechanical torque unbalance in the induction motor. Their method uses the motor phase current sideband component to estimate the unbalance. Jalan and Mohanty [10] used a model-based fault diagnosis technology to diagnose the misalignment or unbalanced motor by building the methodical model and calculating residual vibration on the healthy motor. They measured the same type of vibration signal on the different types of faulty motors. Based on the difference between the motor vibration signals, they were able to perform fault identification to identify the faulty motor. Unlike other papers that covered mechanical unbalance (MU), Kim [11] performed a comprehensive study of MU, and developed an algorithm to estimate it. He made an interesting attempt to investigate machine running speed steady stages based on q-axis current simulation with a range of mathematical and simulation tools. A preliminary algorithm has been developed for extracting the stator frame phase current signal from the Pulse-width modulation (PWM) Voltage-source-inverter (VSI) terminal and converting it to q-axis current in the rotor frame, according to a rotating frame matrix conversion. A novel unbalance observer which is only based on q-axis current to calculate the system unbalance mass is proposed. Phase current in the stator frame signals varies with electrical frequency and mechanical rotating frequency, and there are two side-band fault signals in the frequency domain, with two types of frequency coupled together. This phenomenon increases the complexity of the design unbalance observer. Instead of two-side band fault signals in phase current in the stator frame, there is only one harmonic signal that needs to be monitored in the rotor frame. This harmonic signal amplitude is proportional to rotor unbalance term $m_u e$ (where m_u is unbalance

mass and e is distance between the centre of m_u and rotor centre) and the frequency refers to the rotor mechanical rotating frequency. Besides the proposed unbalance observer, the author also used one popular simple proportional and integral (PI) speed control strategy. The proposed unbalance estimate scheme in his paper also can be extended and applied to the studies on monitoring the unbalance problem in a no-steady-state operation condition of the Permanent Magnetic Synchronous Motor (PMSM). However, in his experimental research, the data set for verifying unbalance only contained two different weights, and a motor running two different speeds. This data set could have been more reliable if more recordings of the unbalance segment had been included. Furthermore, the motor mechanical running speeds, 60 RPM & 180 RPM, were too slow to present a relative speed motor working condition of 3000 RPM and above. An experimental setup with motor-rated speed would be more reliable. Besides performing unbalance force research, Shen [12] originally mentioned the unbalance momentum (UM), which is generated by disk deformation. The effect of UM reduces the accuracy of the theoretical resonance amplitudes prediction, and the UM is classified into different vibration unbalance modes [13]-[16]. Although researchers have studied MU and UM fault in rotor in [7]-[16] extensively, very few of them consider the electromagnetic force effect in analytical, numerical or experimental ways.

2.2 Review of techniques for motor Unbalanced Magnetic Pull

Other than MU, Unbalanced Magnetic Pull (UMP) is another big concern that demands a thorough study and understanding of motor design and diagnosis. In fact, UMP generated by rotor eccentricity faults has been an active research topic for more

than a hundred years [17]. In 1943, Robinson [18] analytically calculated Unbalanced Magnetic Pull (SUMP) due to static rotor eccentricity faults in induction and synchronous motors. However, in his research, the UMP equation is simply expressed as a product of the stator bore area and squared magnetic flux density. In switched reluctance motor study, not only some valuable new information on the static rotor eccentricity faults are presented, the dynamic rotor eccentricity faults are also presented in a coherent manner [19]. The authors depict that UMPs can be quickly predicted by their developed Magnetic Equivalent Circuit (MEC) approach when the relative rotor eccentricity is less than 25% of the normal air-gap. Kovacs [20] considered UMP in an eccentric rotor as a mechanical spring force with a negative spring constant when he studied motor vibration behavior. UMP was also considered as a spring force with negative spring constant by Belmans and his colleagues [21], when they did motor Rotor-Dynamic analyses. The authors reported that UMP decreases the critical running speed of the motor. Based on the motor shaft movement orbit from a mechanical point of view, Werner [22] uses shaft vibration signals to study induction motor SUMP due to the static eccentricity fault. On the other hand, Khoobroo and Fahimi [23] use a field reconstruction method to study SUMP in a Permanent Magnet Synchronous Motor (PMSM). Bi and his colleagues [24] analyzed and calculated Dynamic Unbalanced Magnetic Pull (DUMP) within one motor revolution. The lowest order of the extrinsic UMP harmonic is one-in-one motor revolution. Iamamura et al. [25] calculated SUMP, DUMP, and combined UMPs with these two components in a synchronous generator. They classified the largest amplitudes of SUMP and DUMP at different frequencies based on the FFT of the UMP. Besides the analytical methods used in UMP calculations, some numerical methods are also used by researchers to do the UMP analyses. The Finite Element

Method (FEM) is a popular technique to calculate UMP because it is easy to handle the complex geometry of the motor. Chari et al. [26] introduce the basic principles of two-dimensional FEM and its applications for the analysis of UMP in the motor. Although the concept of 3D FEM was presented by Chari in (year) [27], the 3D FEM method was seldom used until year 2000 due to low computer efficiency and high computing cost. Neves et al. [28] also show that a two-dimensional model is sufficient to study motor vibration behavior due to UMP in a switched reluctance motor. Even though there is no eccentricity distance between the rotor center and stator center, the intrinsic UMP, which is only related to EM structures, such as the matching between the magnetic pole pair and the slot number, still exists. However, it is only formed in even harmonics and can be eliminated by an even slot number [29]. Besides the EM structure induced UMP, Bi and his colleagues [30] also presented the UMP induced by the motor drive current, and mentioned that asymmetric windings are more sensitive to the drive current than symmetric ones. Although researchers have studied different types of UMPs fault in [18]-[30] extensively, the differences between SUMP, DUMP, Inclined Unbalanced Magnetic Pull (IUMP) and Axial Unbalanced Magnetic Pull (AUMP) has not been effectively analyzed. To successfully classify these four types of UMPs, the analytical models of the PMSM should be fully developed.

2.3 Review of techniques for motor faults based on current & vibration signals

PMSM faults can be the result of abnormality in the driver, stator, bearing, rotor and/or cooling system. The driver and stator faults belong in the electrical category of the PMSM. By directly monitoring stator current or voltage signals, the electrical faults can be detected and classified [31]-[33]. Bearing faults are well-defined and

studied in numerical papers via the analyses of vibration signals [34]-[38]. Rotor faults in motors, including rotor unbalance fault, misalignment fault, dynamic eccentricity and static eccentricity fault, need to be further studied.

Many papers have analyzed these problems. Jalan and Mohanty [39] use a model-based fault diagnosis technology to diagnose the misalignment and Mechanical Unbalance (MU) of the motor. They built a methodical model and calculated the residual vibration of the healthy motor. They then measured the same type of vibration signal on different types of faulty motors. Based on difference between the motor vibration signals, they performed the fault identification to identify the faulty motor. Even though vibration and thermal diagnostic analyses have been used for decades, most of the recent research is still restricted to the electrical properties diagnosis of the motor, with emphasis on the stator voltage or phase current monitoring. Rajagopalan et al. [40] demonstrated that the motor current signature analysis can be applied to the diagnosis of the brushless DC (BLDC) motor rotor condition, particularly in applications which converge to a steady state operation. However, they also mentioned that pulsating loads have the capability to mask rotor fault signatures by using sample FFT spectrum. When a motor is operating under varied load, the phase current becomes non-stationary signals. Time-frequency signal processing technologies, such as Short-time Fourier Transform (STFT) and Wavelet, have been widely adopted in motor fault diagnosis. Gu et al. [41] studied induction motor current signals using modified bispectrum for diagnosis compressor faults, such as valve leakage, inter-cooler leakage and belt looseness, when the motor undertakes a varying load under different faulty conditions. Unlike other papers that study BLDC faults by monitoring current signals, Rajagopalan et al. [42] performed a comprehensive study of BLDC rotor faults under varied speeds and/or constantly

changing load operating conditions, based on a Spectrogram of filtered BLDC current and Windowed Fourier Ridge (WFR). The automatic rotor fault detection algorithm is designed with a synthetic adaptive tracking filter. The high frequency noise can be filtered out by the Low Pass Pre-filter. The fundamental frequency and all harmonics above the second order harmonics are removed by the sixth and eighth switch capacitor filters, respectively. However, some useful faulty information could be accidently removed. The center frequency of the adaptive filter can be varied with motor speed to ensure that the fundamental frequency is removed and the fault frequencies are distinct. In electrical signals analysis, the authors systematically study the characteristics of the Spectrogram and windowed Fourier Ridges by using an analytical model, and validate the effectiveness of the MATLAB® simulation model by injecting a hypothetical fault signal with two side-band fault frequencies. The advantage of their proposed method is that no additional sensor is needed, but it cannot distinguish different types of UMPs.

2.4 Review of techniques for blade crack monitoring

The rotor blade is a rotationally periodic structure (RPS). Shen et al. analyzed the eigenvalues and the corresponding eigenvectors of the RPS [43]. Hameeda and Honga [44] presented an intelligent digital signal proceeding methodology for diagnosing faults in rotating machinery using the wavelet theory, based on a nonlinear adaptive algorithm. Huang and Kuang [45] investigated the effect of a near root local blade crack on the stability of a grouped blade disk. They also modeled a shrouded blade disk with crack, and derived equations of blade motion. Chiu and Huang [46] analytically studied the influence of coupling vibrations on shaft-torsion, disk-

transverse and bland-bending of a rotor system with a mistuned blade. They did mode analysis and illustrated the changes of the rotor's natural frequencies due to mistuned blades. Huang [47] examined the effects of the number of blades and the distribution of cracks on mode localization in a group blade-disk system, and claimed that the number of cracked blades significantly affects the localization modes in a mistuned blade-disk. He also found that increasing the number of cracked blades enhances localization. Fang et al. [48] studied the vibration response of a single crack on an aero-engine bladed-disk, simplifying the model into several cantilevered beams coupled with springs which connect the top tips of each beam. They applied the U-transformation approach to develop analytical solutions to the mode and harmonic vibrations, and concluded that even small crack damage could cause vibration mode localization and forced response localization. Roy and Guli [49] analyzed the effect of damage growth on the modal frequencies by using a finite element model of a helicopter rotor blade made of composite materials. They claimed that damage can be detected by monitoring changes in swap mode, bending mode, and torsion mode frequencies. Kuang and Huang [50] investigated the effects of position, depth of crack and rotating speed in periodic shrouded blades which were used to simulate the blade of a turbo-rotor disk. They derived the equation of motion by employing the Galerkin method, and presented numerical results. Chang and Chen [51] presented a technique for single edge crack damage detection, and employed the wavelet transform to analyze spatially distributed signals. They argued that the crack position could be identified by the distributions of the wavelet coefficients. Kumer et al. [52] studied the effects of low cycle fatigue (LCF) damage on the rotating frequency of a turbine blade. They concluded that LCF can cause sufficient material stiffness loss as the damage growth progresses, and that rotating frequency changes can be used as an

indicator to track damage growth. Therefore, the final stage of damage in the structure before failure can be detected by their method. Parker [53] derived the relationship between acoustic resonance and blade vibration in axial flow compressors. He illustrated the relation between the blade excitation and acoustic resonance frequencies. Based on his formula, the acoustic frequencies can be obtained if the excitation frequencies and rotor speed are known. Srinivas et al. [54] studied the variation of natural frequencies as a function of stiffness reduction factor, and also performed damage prediction of rotating blades using displacement residuals. Although researchers have studied blade crack fault extensively, the electromagnetic force effect should be considered further.

2.5 Inspiration from the literature review

The literature review shows that the PMSM is a complicated electromagnetic mechanical system. The mechanical researcher's focus is mainly on exploring the mechanical reasons, whereas the electrical researcher's focus EM and electrical reasons. In order to fully understand motor vibration behavior and improve the accuracy of fault diagnosis, all the fields should be fully studied together and involve deep knowledge of UMP and vibration analysis. The demand for a high-power density motor with small overall dimensions has resulted in the size of the air-gap between the rotor and stator becoming smaller than before. Any imprecise dimension introduces the varied uneven air-gap in axial direction and may cause serious IUMP. In order to detect the magnet field by a hall sensor, the rotor is made longer than the stator. In this situation, the rotor center is offset from the stator center in the axial direction, and consequently, AUMP is induced. The induced IUMP and AUMP will

certainly become a considerable concern. These two types of UMP can only be studied by three-dimensional numerical methods. In view of the many multi-frequency components in UMP, transient analysis should be favored over harmonic analysis. The major drawback of performing UMP calculation in three-dimensional FEM and vibration study in transient analysis is computing time consumption. It is desirable to have analytical approaches which are able to predict motor vibration and fault more quickly. In the previous experimental research [42], shims, the specimens designed for dynamic eccentricity, are simply inserted between the rotor and the inner ring of the ball bearing. The fitting dimension and pre-load may have excessive tolerance. As a result, the dynamic eccentricity may be varied with time. Moreover, when the shims are only inserted on one side of the rotor shaft, this may cause not only dynamic eccentricity fault, but also misalignment fault. This is because the air-gap is also changed along the motor shaft rotation axis. Consequently, the experimental results may be incorrect due to this poor faulty design. A new innovative method should be considered to create the accurate dynamic eccentricity fault, static eccentricity fault and other types of UMPs faults in experimental design.

2.6 Conclusions

In this chapter, numerous papers are reviewed. These papers show the studying results in MU and UMPs analyses, and present motor fault analyses based on vibration and current signals, motor blade fault. UMP is an important electromagnetic (EM) index in the fault analysis, especially if the rotor eccentricity is obvious. In motor vibration study, mechanical unbalance force and different types of UMPs are considered as the major motor vibration sources in the mathematical model of the

PMSM in Chapter 3. Therefore, in-depth knowledge of both fields, MU and UMP, are required in fault diagnosis of the PMSM.

CHAPTER 3

MATHEMATICAL MODEL OF PMSM

3.1 Introduction

When a Permanent Magnet Synchronous Motor (PMSM) is under faulty state, some malfunction of the motor components may generate additional excitation forces on the motor and/or change the original structural properties of the motor in a healthy state. These additional forces or structural changes obviously affect the vibration behaviors of the motor, resulting in an undesirable increase in vibration level and natural frequency shifts. To understand the reasons behind the undesired vibration and frequency shift in the PMSM, the mathematical model with a capability to effectively predict the natural frequencies of the motor is to be developed. This model can be further utilized to build an electrical rotating machine fault diagnosis platform.

3.2 Mathematical model of rotor

3.2.1 Lumped mass of rotor

In the physical model of a motor, the rotor is a continuous mass distribution system which has an infinite degree of freedom. For analytical studies, the rotor can be simplified into a lumped mass model with a multiple-degree system. The lumped

mass node can be selected on the center of the yoke, both ends of the rotor shaft and the position where the fan or other accessories are mounted on the shaft. It is clear that the rotor yoke with a magnet has a main mass M_c, main polar momentums of inertia $J_p^{(c)}$, and main radial momentums of inertia $J_d^{(c)}$ (as shown in Figure 3.1). Rotor shaft mass is evenly distributed with density μ_{rs} while the length and radius of rotor are l_{rs} and r_{rs} respectively. Therefore, the equivalent lumped mass M, lumped polar momentums of inertia J_p, and lumped radial momentums of inertia J_d can be calculated by:

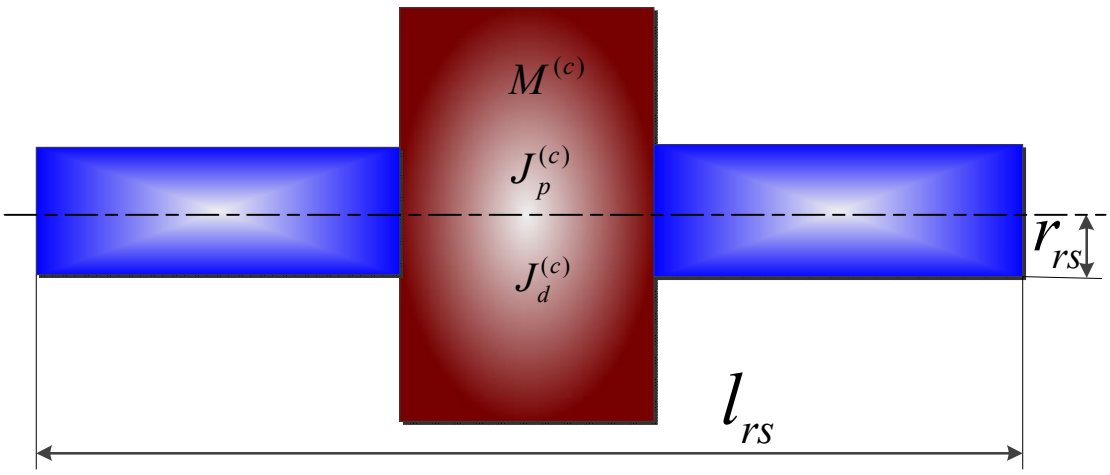

Figure 3.1: Rotor lumped mass

$$\begin{cases} M = M^{(c)} + \mu_{rs} l_{rs} \pi r_{rs}^2 \\ J_p = J_p^{(c)} + \frac{1}{2} \mu_{rs} l_{rs} \pi r_{rs}^4 \\ J_d = J_d^{(c)} + \frac{1}{12} \mu_{rs} l_{rs}^3 \pi r_{rs}^2 \end{cases} \tag{3.1}$$

3.2.2 Critical running speed of the rotor on rigid supports

The motor rotor is assumed to be supported by two rigid bearings. The rotor shaft cross section moment of inertia is I, and the shaft material modulus is E. The structure of the rotor with rigid supports is shown in Figure 3.2.

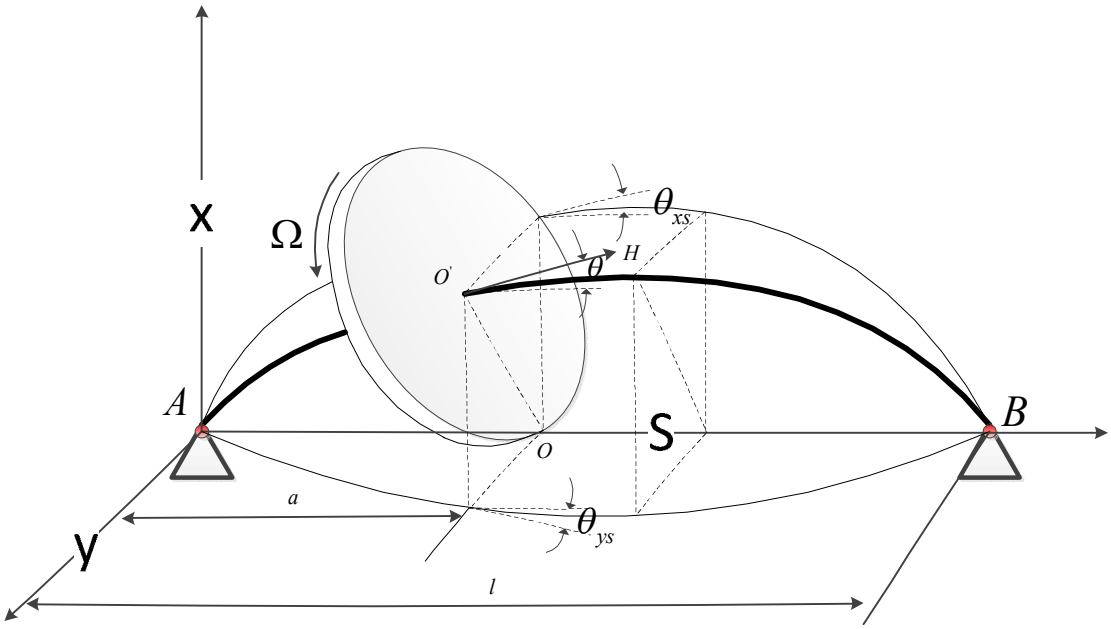

Figure 3.2: Flexible rotor shaft with fixed supports

When the equivalent force p is applied to the rotor yoke, the rotor yoke rotation centre will shift from O to O' due to the bending deflection of the shaft. This equivalent force may be the Mechanical Unbalance (MU) force and/or the Unbalanced Magnet Pull (UMP). The flexibility and angular displacement of the center in the plane (x, s) can be expressed as:

$$\begin{cases} r = \dfrac{pa^2(l-a)(2l-a)}{6lEI} \\ \varphi = \dfrac{pa(l-a)(2l-a)}{3lEI} \end{cases}, \tag{3.2}$$

where l is the distance between two support bearings and a is the distance between the left support bearing and the lumped mass center of the rotor.

The bending moment may be generated at the rotor yoke rotating centre O due to motor rotor misalignment. When the bending moment is applied to O', the flexibility and angular displacement of the center in the plane (x, s) are:

$$\begin{aligned} r &= \frac{Ma(l-a)(2l-a)}{3lEI} \\ \varphi &= \frac{M(3a^2-3la+l^2)}{3lEI} \end{aligned} \quad , \tag{3.3}$$

when the unit force or unit bending moment is applied to O, the unit coefficient pliability is:

$$\begin{aligned} \alpha_{rr} &= \frac{a^2(l-a)(2l-a)}{6lEI} \\ \alpha_{r\varphi} = \alpha_{\varphi r} &= \frac{a(l-a)(2l-a)}{3lEI} \\ \alpha_{\varphi\varphi} &= \frac{(3a^2-3la+l^2)}{3lEI} \end{aligned} \quad . \tag{3.4}$$

Stiffness matrix is the inverse matrix of flexibility matrix:

$$\begin{bmatrix} k_{rr} & k_{r\varphi} \\ k_{\varphi r} & k_{\varphi\varphi} \end{bmatrix} = \begin{bmatrix} \alpha_{rr} & \alpha_{r\varphi} \\ \alpha_{\varphi r} & \alpha_{\varphi\varphi} \end{bmatrix}^{-1} \quad . \tag{3.5}$$

The four critical angular velocities can be obtained and expressed as:

$$\begin{bmatrix} \omega_{rr} & \omega_{r\varphi} \\ \omega_{\varphi r} & \omega_{\varphi\varphi} \end{bmatrix} = \begin{bmatrix} \sqrt{\frac{K_{rr}}{M}} & \sqrt{\frac{K_{r\varphi}}{M}} \\ \sqrt{\frac{K_{\varphi r}}{J_d}} & \sqrt{\frac{K_{\varphi\varphi}}{J_d}} \end{bmatrix} \quad , \tag{3.6}$$

with reference to [6], the four critical angular velocities can be obtained from the following equation:

$$\begin{aligned}&\omega_n^4-(J_p/J_d)\Omega\omega_n^3-(\omega_{rr}^2+\omega_{\varphi\varphi}^2)\omega_n^2\\&+(J_p/J_d)\Omega\omega_{rr}^2\omega_n+\omega_{rr}^2\omega_{\varphi\varphi}^2-\omega_{r\varphi}^2\omega_{\varphi r}^2\\&=0\end{aligned}. \tag{3.7}$$

By solving equation (3.7), the first four vibration mode critical angular velocities can be obtained.

3.2.3 Critical running speed of the rotor on flexible supports

In the real case, the rotor of the motor is supported by the ball bearings or Fluid Dynamic Bearing (FDB). Therefore, the bearings need to be considered as flexible supports. The physical model of the rotor with flexible supports is shown in Figure 3.3. For the general case, it can be assumed that the bearing stiffness at the support A is different from that at support B. The deflection at point B is assumed to exceed that at A. In Figure 3.4, the deflections in the x direction at supports A and B are also assumed to be x_A and x_B, respectively. The deflection at point O in the x direction can be linearly calculated by:

$$\begin{cases}x_1=(1-\dfrac{a}{l})x_A+\dfrac{a}{l}x_B\\-\theta_{xA}=\dfrac{x_B-x_A}{l}\end{cases}. \tag{3.8}$$

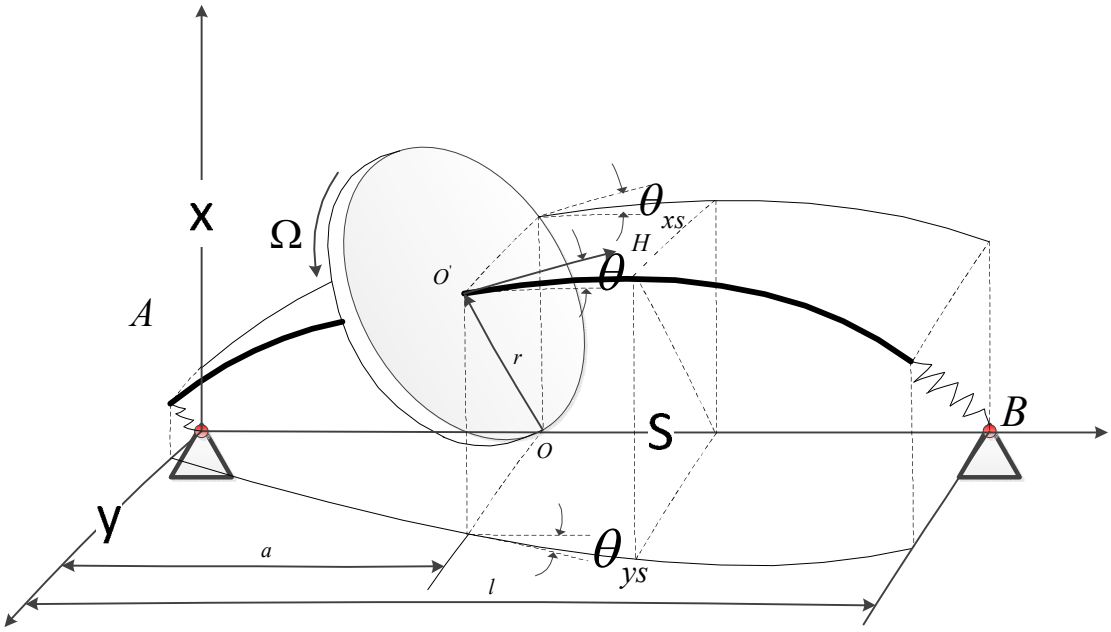

Figure 3.3: Flexible rotor shaft with flexible supports

In Figure 3.5, the deflections in the ***y*** direction at supports A and B are y_A and y_B, respectively. The deflection at point O in the y direction can be linearly calculated by:

$$\begin{cases} y_1 = (1-\frac{a}{l})y_A + \frac{a}{l}y_B \\ -\theta_{yA} = \frac{y_B - y_A}{l} \end{cases}, \tag{3.9}$$

The stiffness of the bearings at supports A and B is k_A and k_B. When a force P or bending moment M is applied at O, another assumption is also made that the x direction component of force P and moment M is $Pcos\beta$ and $Mcos\beta$, respectively; accordingly, the y direction component of force P and moment M should be $Psin\beta$ and $Msin\beta$, respectively.

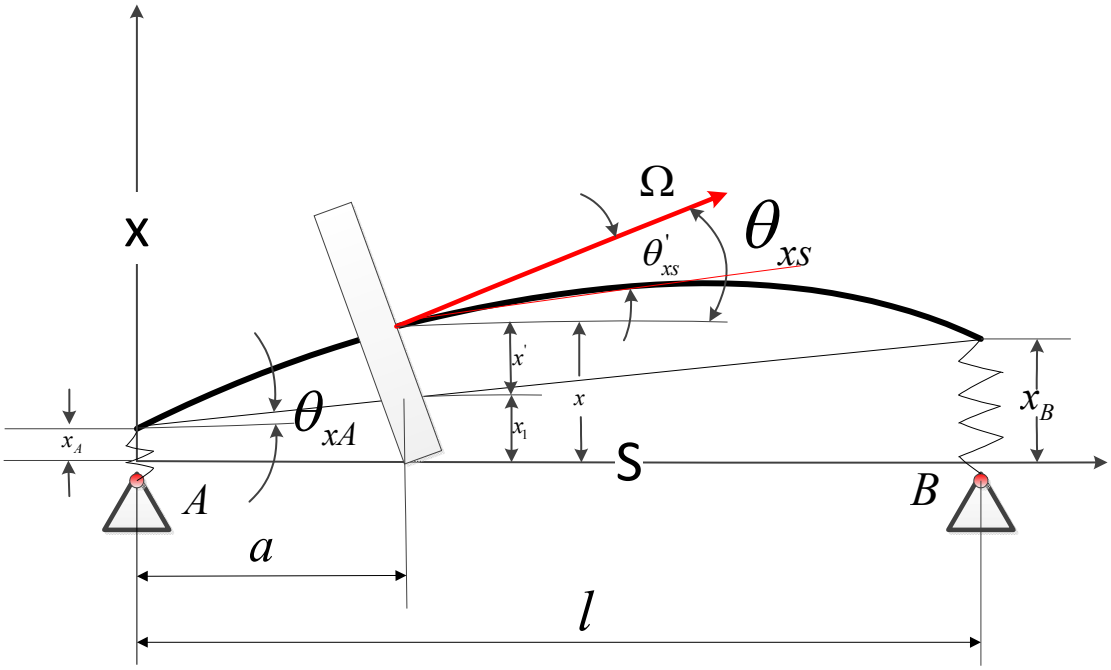

Figure 3.4: Flexible rotor shaft with flexible supports in x direction

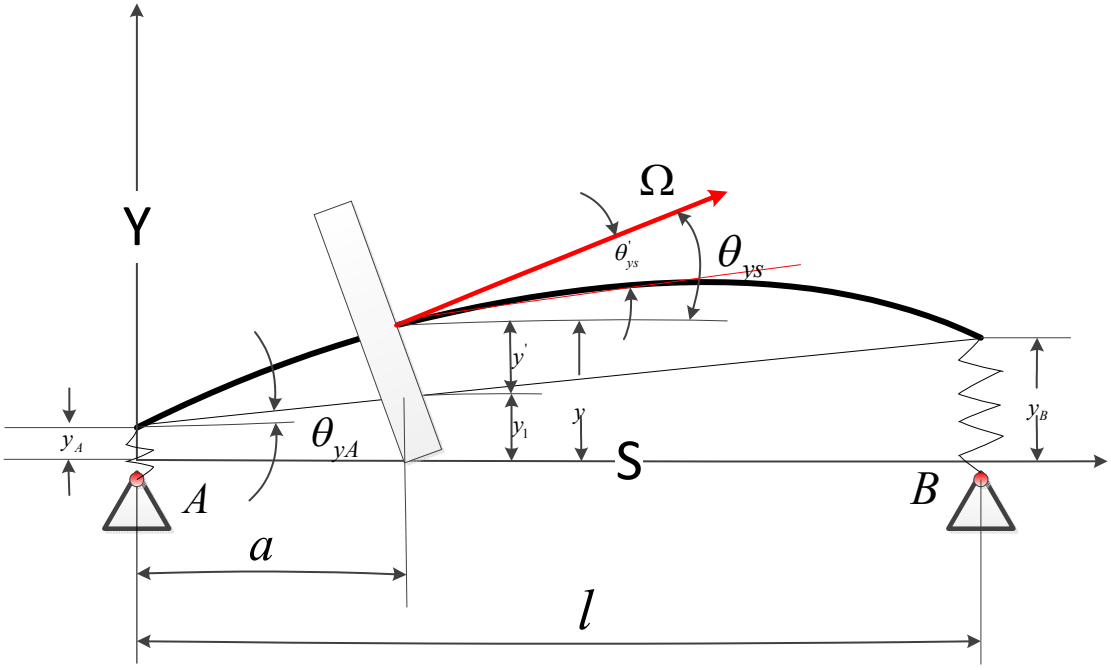

Figure 3.5: Flexible rotor shaft with flexible supports in y direction

The reaction force at supports A, B due to force P can be calculated by:

$$\begin{cases} R_{Ax\_P} = P(1-\dfrac{a}{l})\cos\beta \\ R_{Ay\_P} = P(1-\dfrac{a}{l})\sin\beta \\ R_{Bx\_P} = P(\dfrac{a}{l})\cos\beta \\ R_{By\_P} = P(\dfrac{a}{l})\sin\beta \end{cases} . \tag{3.10}$$

The reaction force at supports A, B due to bending moment M can be calculated by:

$$\begin{cases} R_{Ax\_M} = -\dfrac{M\cos\beta}{l} \\ R_{Ay\_M} = -\dfrac{M\sin\beta}{l} \\ R_{Bx\_M} = \dfrac{M\cos\beta}{l} \\ R_{Ax\_M} = \dfrac{M\sin\beta}{l} \end{cases} . \tag{3.11}$$

It can be assumed that the reaction force of the bearing at supports A and B is a linear function of their deflection when force P is applied. So the deflection at A, B is:

$$\begin{cases} x_A = \dfrac{R_{Ax\_p}}{k_A}, x_B = \dfrac{R_{Bx\_p}}{k_B} \\ y_A = \dfrac{R_{Ay\_p}}{k_A}, y_B = \dfrac{R_{By\_p}}{k_B} \end{cases} , \tag{3.12}$$

when bending moment *M* is applied, the deflection at *A, B* is:

$$\begin{cases} x_A = \dfrac{R_{Ax\_M}}{k_A}, x_B = \dfrac{R_{Bx\_M}}{k_B} \\ y_A = \dfrac{R_{Ay\_M}}{k_A}, y_B = \dfrac{R_{By\_M}}{k_B} \end{cases} . \tag{3.13}$$

Equations (3.10) and (3.11) are substituted into equations (3.12) and (3.13), following which equations (3.12) and (3.13) are substituted into equations (3.8) and (3.9). The deflection and section corner induced by force P can then be calculated:

$$\begin{cases} x_{1\_p} = P\left[\frac{1}{k_A}(1-\frac{a}{l})^2 + \frac{1}{k_B}(\frac{a}{l})^2\right]\cos\beta \\ \theta_{x\_p} = -\frac{P}{l}\left[\frac{1}{k_B}\frac{a}{l} - \frac{1}{k_A}(1-\frac{a}{l})\right]\cos\beta \\ y_{1\_p} = P\left[\frac{1}{k_A}(1-\frac{a}{l})^2 + \frac{1}{k_B}(\frac{a}{l})^2\right]\sin\beta \\ \theta_{y\_p} = -\frac{P}{l}\left[\frac{1}{k_B}\frac{a}{l} - \frac{1}{k_A}(1-\frac{a}{l})\right]\sin\beta \end{cases}, \tag{3.14}$$

the deflection and section corner induced by bending moment M can be calculated by:

$$\begin{cases} x_{1\_M} = \frac{M}{l}\left[-\frac{1}{k_A}(1-\frac{a}{l}) + \frac{1}{k_B}\frac{a}{l}\right]\cos\beta \\ \theta_{x\_M} = \frac{M}{l^2}\left[\frac{1}{k_A} + \frac{1}{k_B}\right]\cos\beta \\ y_{1\_M} = \frac{M}{l}\left[-\frac{1}{k_A}(1-\frac{a}{l}) + \frac{1}{k_B}\frac{a}{l}\right]\sin\beta \\ \theta_{y\_M} = \frac{M}{l^2}\left[\frac{1}{k_A} + \frac{1}{k_B}\right]\sin\beta \end{cases}. \tag{3.15}$$

In Figure 3.4 and Figure 3.5, the relationship below can be built:

$$\begin{cases} x = x_1 + x' \\ y = y_1 + y' \end{cases}, \tag{3.16}$$

where, x' and y' in Figures 3.4 and 3.5 are the disk displacement in x and y direction due to the shaft deformation. The total deflection in the x and y directions due to force P can be obtained by substituting equations (3.2) and (3.14) into equation (3.16):

$$\begin{cases} x = P\left[\frac{1}{k_A}(1-\frac{a}{l})^2 + \frac{1}{k_B}(\frac{a}{l})^2\right]\cos\beta + \frac{pa^2(l-a)(2l-a)}{6lEI}\cos\beta \\ y = P\left[\frac{1}{k_A}(1-\frac{a}{l})^2 + \frac{1}{k_B}(\frac{a}{l})^2\right]\sin\beta + \frac{pa^2(l-a)(2l-a)}{6lEI}\sin\beta \end{cases} , \tag{3.17}$$

The rotor structure is assumed as isotropy, so the coefficient pliability:

$$\alpha_{rr} = \left[\frac{1}{k_A}(1-\frac{a}{l})^2 + \frac{1}{k_B}(\frac{a}{l})^2\right] + \frac{a^2(l-a)(2l-a)}{6lEI} . \tag{3.18}$$

In Figures 3.4 and 3.5, the relationship below can be built:

$$\begin{cases} \theta_{xs} = \theta_{xA} + \theta_{xs}' \\ \theta_{ys} = \theta_{yA} + \theta_{ys}' \end{cases} , \tag{3.19}$$

the total section corner in the x and y direction due to force p can be obtained by substituting Equations (3.2) and (3.14) into Equation (3.19):

$$\begin{cases} \theta_x = -\frac{P}{l}\left[\frac{1}{k_B}\frac{a}{l} - \frac{1}{k_A}(1-\frac{a}{l})\right]\cos\beta + \frac{pa(l-a)(2l-a)}{3lEI}\cos\beta \\ \theta_y = -\frac{P}{l}\left[\frac{1}{k_B}\frac{a}{l} - \frac{1}{k_A}(1-\frac{a}{l})\right]\sin\beta + \frac{pa(l-a)(2l-a)}{3lEI}\sin\beta \end{cases} , \tag{3.20}$$

the coefficient pliability of section corner:

$$\alpha_{r\varphi} = -\frac{1}{l}\left[\frac{1}{k_B}\frac{a}{l} - \frac{1}{k_A}(1-\frac{a}{l})\right] + \frac{a(l-a)(2l-a)}{3lEI} . \tag{3.21}$$

The total section corner in the x and y direction due to bending moment M can be obtained by substituting equations (3.3) and (3.15) into equation (3.19):

$$\begin{cases} \theta_x = \dfrac{M}{l^2}\left[\dfrac{1}{k_A}+\dfrac{1}{k_B}\right]\cos\beta + \dfrac{M(3a^2-3la+l^2)}{3lEI}\cos\beta \\ \theta_y = \dfrac{M}{l^2}\left[\dfrac{1}{k_A}+\dfrac{1}{k_B}\right]\sin\beta + \dfrac{M(3a^2-3la+l^2)}{3lEI}\sin\beta \end{cases}, \tag{3.22}$$

the coefficient pliability of the section corner:

$$\alpha_{\varphi\varphi} = \frac{1}{l^2}\left[\frac{1}{k_A}+\frac{1}{k_B}\right] + \frac{(3a^2-3la+l^2)}{3lEI}, \tag{3.23}$$

As $\alpha_{r\varphi} = \alpha_{\varphi r}$, the stiffness matrix is the reverse matrix of the coefficient pliability matrix. When equations (3.18), (3.21) and (3.23) are substituted into equation (3.5), the stiffness can be obtained as shown below:

$$\begin{bmatrix} k_{rr} & k_{r\varphi} \\ k_{\varphi r} & k_{\varphi\varphi} \end{bmatrix} = \begin{bmatrix} \alpha_{rr} & \alpha_{r\varphi} \\ \alpha_{\varphi r} & \alpha_{\varphi\varphi} \end{bmatrix}^{-1} \tag{3.24}$$

$$= \begin{bmatrix} \left[\dfrac{1}{k_A}(1-\dfrac{a}{l})^2+\dfrac{1}{k_B}(\dfrac{a}{l})^2\right]+\dfrac{a^2(l-a)(2l-a)}{6lEI} & -\dfrac{1}{l}\left[\dfrac{1}{k_B}\dfrac{a}{l}-\dfrac{1}{k_B}(1-\dfrac{a}{l})\right]+\dfrac{a(l-a)(2l-a)}{3lEI} \\ -\dfrac{1}{l}\left[\dfrac{1}{k_B}\dfrac{a}{l}-\dfrac{1}{k_B}(1-\dfrac{a}{l})\right]+\dfrac{a(l-a)(2l-a)}{3lEI} & \dfrac{1}{l^2}\left[\dfrac{1}{k_B}+\dfrac{1}{k_B}\right]+\dfrac{(3a^2-3la+l^2)}{3lEI} \end{bmatrix}^{-1},$$

let

$$\begin{aligned} \Delta = & \left\{\left[\frac{1}{k_A}(1-\frac{a}{l})^2+\frac{1}{k_B}(\frac{a}{l})^2\right]+\frac{a^2(l-a)(2l-a)}{6lEI}\right\}\times\left\{\frac{1}{l^2}\left[\frac{1}{k_B}+\frac{1}{k_B}\right]+\frac{(3a^2-3la+l^2)}{3lEI}\right\} \\ & -\left\{\frac{a(l-a)(2l-a)}{3lEI}-\frac{1}{l}\left[\frac{1}{k_B}\frac{a}{l}-\frac{1}{k_B}(1-\frac{a}{l})\right]\right\}^2 \end{aligned} \tag{3.25}$$

then,

$$\begin{cases} k_{rr} = \dfrac{\alpha_{\varphi\varphi}}{\Delta} = \dfrac{1}{\Delta}\left\{\dfrac{1}{l^2}\left[\dfrac{1}{k_A}+\dfrac{1}{k_B}\right]+\dfrac{(3a^2-3la+l^2)}{3lEI}\right\} \\ k_{r\varphi} = -\dfrac{\alpha_{\varphi r}}{\Delta} = \dfrac{1}{\Delta}\left\{\dfrac{1}{l}\left[\dfrac{1}{k_B}\dfrac{a}{l}-\dfrac{1}{k_A}(1-\dfrac{a}{l})\right]-\dfrac{a(l-a)(2l-a)}{3lEI}\right\} \\ k_{\varphi r} = -\dfrac{\alpha_{\varphi r}}{\Delta} = \dfrac{1}{\Delta}\left\{\dfrac{1}{l}\left[\dfrac{1}{k_B}\dfrac{a}{l}-\dfrac{1}{k_A}(1-\dfrac{a}{l})\right]-\dfrac{a(l-a)(2l-a)}{3lEI}\right\} \\ k_{\varphi\varphi} = \dfrac{\alpha_{rr}}{\Delta} = \dfrac{1}{\Delta}\left\{\left[\dfrac{1}{k_A}(1-\dfrac{a}{l})^2+\dfrac{1}{k_B}(\dfrac{a}{l})^2\right]+\dfrac{a^2(l-a)(2l-a)}{6lEI}\right\} \end{cases} . \tag{3.26}$$

By substituting Equation (3.26) into equation (3.6), ω_{rr}, $\omega_{r\varphi}$, $\omega_{\varphi r}$, and $\omega_{\varphi\varphi}$ can be obtained respectively. By substituting ω_{rr}, $\omega_{r\varphi}$, $\omega_{\varphi r}$, and $\omega_{\varphi\varphi}$ into equation (3.7) and solving the equation, the critical angular velocities of the first four vibration modes can be obtained.

3.3 Mathematical model of bearing

The motor rotor could be supported by Fluid Static Bearings (FSBs), Fluid Dynamic Bearings (FDBs), ball bearings, magnet bearings, aero-dynamic Bearings (ADB) and/or other types of bearings.

Although the dynamic characterization of the FSBs is superior in terms of isolating vibrations, this type of bearing is seldom used due to the oil pumps are needed to form a thin lubricant layer between inner and outer races. In contrast, another type of Fluid Bearing, FDBs, in which the thin lubricant layer can be generated by the bearings themselves when the rotor is rotating, is commonly used in high-speed light-load motor applications nowadays. By using FDBs, the vibration and acoustic noise level can be significantly attenuated. So, ball bearings used in hard disk drive (HDD) motors have been entirely replaced by FDBs because the non-repeatable runout

(NRRO) and noise generated by ball bearings can be significantly reduced by using FDBs [55].

Shen et al. [56]-[59] obtained experimental and theoretical estimations of the bearing stiffness and damping coefficient of the FDBs. The simple forms of the stiffness matrix and damping matrix of the FDBs are shown below, respectively:

$$\begin{cases} [C] = \begin{bmatrix} c_{xx} & c_{xy} \\ c_{yx} & c_{yy} \end{bmatrix} \\ [K] = \begin{bmatrix} k_{xx} & k_{xy} \\ k_{yx} & k_{yy} \end{bmatrix} \end{cases} . \tag{3.27}$$

Although FDBs have the aforementioned advantages, ball bearings are still the most commonly used in real life due to their lower cost and larger load range capabilities compared to other types of bearings. With ball bearings, the outer and inner races can be considered as rigid bodies, and an assumption can be made that, when an external force is applied in the x or y direction, it will not induce deflection in the y or x direction. Ball bearings can thus be considered as an isotropic component when the dynamic performance is analyzed in a motor with ball bearings. The stiffness and damping matrix of the ball bearings can therefore be simplified as:

$$\begin{cases} [C] = \begin{bmatrix} c_{xx} & 0 \\ 0 & c_{xx} \end{bmatrix} \\ [K] = \begin{bmatrix} k_{xx} & 0 \\ 0 & k_{xx} \end{bmatrix} \end{cases} . \tag{3.28}$$

3.4 Mathematical model of stator

The motor stator includes the stator winding assembly, the outer races of rolling bearings, hall sensors, and the motor base. The natural frequency patterns of the stator coil may change if its structure and boundary condition are changed. Diagnosis of stator coil-related faults is thus possible by detecting shifted natural frequency of the stator coil.

3.4.1 Stator coil

3.4.1.1 Teeth of stator coil

Each tooth of the stator coil can be modeled as a cantilever beam, as shown in Figure 3.6. The dominated vibration of a cantilever beam is the bending mode vibration. The natural frequencies of a cantilever beam can also be calculated [60].

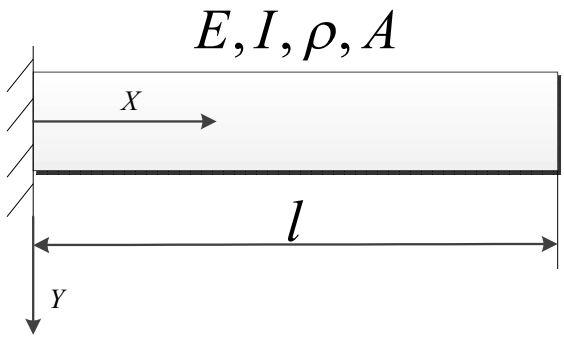

Figure 3.6: A cantilever in bending vibration

$$\omega_i = \lambda_i^2 \sqrt{\frac{EI}{\rho A}}, \qquad i = 1,2,3.....n \tag{3.29}$$

where λ_i can be obtained by solving:

$$\cos(\lambda l)\cosh(\lambda l) = -1 \quad , \tag{3.30}$$

where l is the length of the beam.

The solution of Equation (3.30) has an infinite number; the first three solutions are:

$\lambda_1 l = 1.875104$; $\lambda_2 l = 4.694091$; $\lambda_3 l = 7.854757$.

3.4.1.2 Main body of stator core

The stator coil of the motor can be modeled as a ring type element. The mode shape can be seen in Figure 3.7.

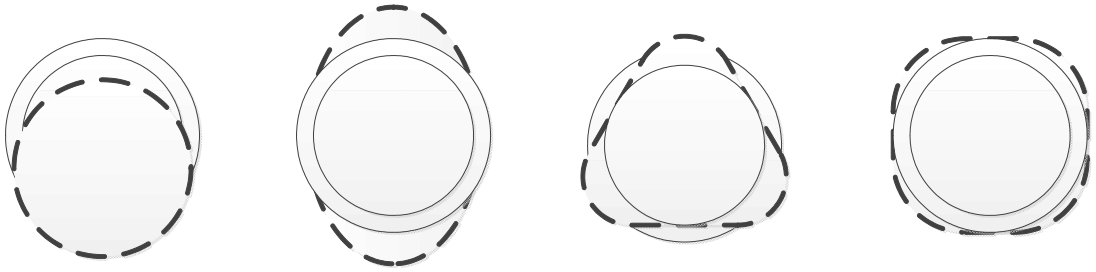

Figure 3.7: First four vibration mode shapes of ring type element

If the ratio between the length of stator and its diameter, l/D_c is less than or equals to unity, the stator can be considered as a hollow cylinder, and the natural frequencies can be calculated by [61] [62]:

$$f_n = \frac{2}{\pi D_c} \frac{n(n^2-1)}{\sqrt{n^2+1}} \sqrt{\frac{E_c I_c}{\rho_c L_c h_c}}, \tag{3.31}$$

where I_c is the moment of inertia of the stator coil, E_c is the modulus of elasticity, and h_c is the length of the stator core.

If the ratio between the length of the stator and its diameter, l/D_c is larger than unity, the stator can be considered as a cylindrical shell, and the natural frequencies can be calculated by:

$$f_i = \frac{\Omega_i}{\pi D_c}\sqrt{\frac{E_c}{\rho_c(1-\mu_c{}^2)}} \qquad i = 1,2,3.....n \quad , \tag{3.32}$$

where μ_c is the Poisson coefficient of the stator coil , and Ω_i can be calculated:

$$\Omega_i = \begin{cases} 1 & i = 0 \\ \frac{1}{2}\sqrt{(1+i^2+k^2i^4)+\sqrt{(1+i^2+k^2i^4)^2-4k^2i^6}} & i > 0 \end{cases} \quad , \tag{3.33}$$

where k is a no-dimension coefficient and has:

$$k = \frac{h_c^2}{D_c{}^2} \quad . \tag{3.34}$$

If the stator teeth, stator core, and motor case, in which the motor stator is tightly inserted, are considered as one component in the natural frequency of stator calculation, equation (3.32) should be modified and expressed as:

$$f_i = \frac{1}{2\pi}\sqrt{\frac{K_i^{\,c} + K_i^{\,case}}{M_c + M_{teeth} + M_{case}}} \quad , \tag{3.35}$$

where

$$K_i^{\,c} = \frac{4\Omega_i^2}{D_c}\frac{\pi L_c h_c E_c}{1-\mu_c{}^2} \quad , \tag{3.36}$$

$$K_i^{\,case} = \frac{4\Omega_i^2}{D_{case}}\frac{\pi L_{case} h_{case} E_{case}}{1-\mu_{case}{}^2} \quad , \tag{3.37}$$

and

$$M_c = \pi \rho_c D_c L_c h_c \quad , \tag{3.38}$$

$$M_{case} = \pi \rho_{case} D_{case} L_{case} h_{case} \quad , \tag{3.39}$$

$$M_{teeth} = N_t L_t W_t L_c \quad . \tag{3.40}$$

Where N_t is the number of teeth in the stator coil, L_t is the tooth length in equation (3.40), and W_t is the width of the teeth.

3.5 Mathematical model of motor foundation

To reduce the vibration of the motor and isolate the vibration of the motor from other devices, a number of isolation pads are usually installed under the motor mounting plate as shown in Figure 3.8.

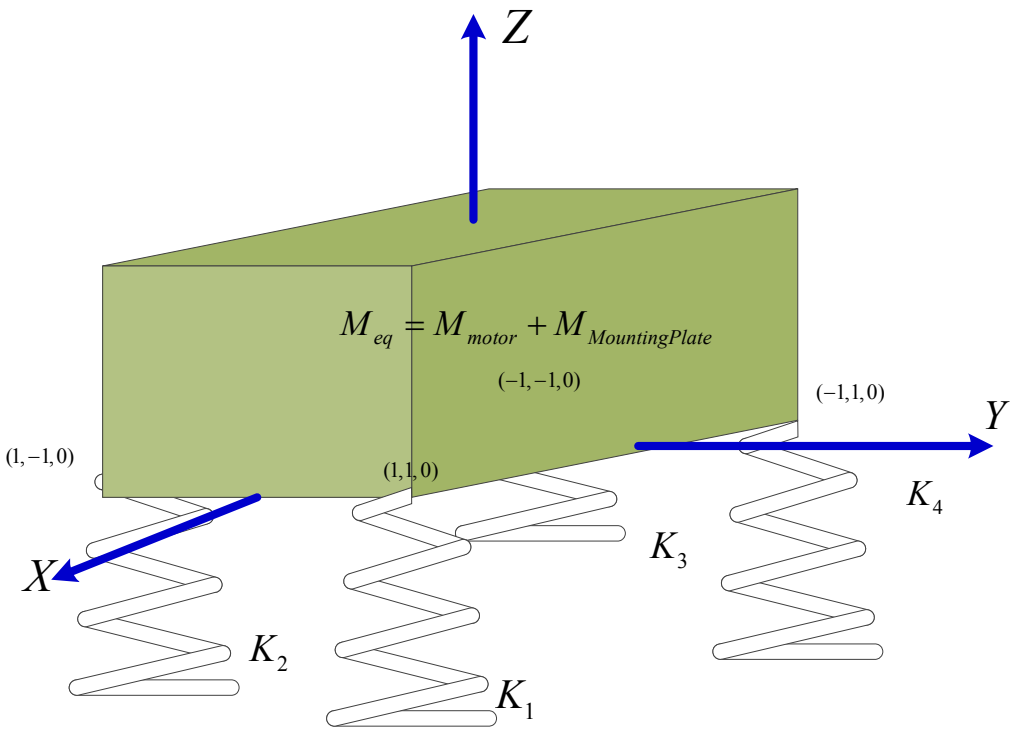

Figure 3.8: Motor with mounting plate isolated by isolation pad

In this study, four isolation pads with the same stiffness and damping coefficient in all Degrees of Freedom (DOF) are assumed to connect the motor mounting plate to the ground, with the stiffness of the isolation pad in x, y, and z as K_x, K_y and K_z respectively. Another assumption is that the principal moments of the inertia of the mounting plate are I_{xx}, I_{yy} and I_{zz}, respectively. If there is no coupling effect between x, y and z and rotating angles α, β and γ due to symmetrical mounting, the foundation natural frequencies are [60]:

$$\begin{cases} \omega_x = \sqrt{\dfrac{\sum_{i=1}^{4} K_x^i}{M_{eq}}} \\ \omega_y = \sqrt{\dfrac{\sum_{i=1}^{4} K_y^i}{M_{eq}}} \\ \omega_z = \sqrt{\dfrac{\sum_{i=1}^{4} K_z^i}{M_{eq}}} \end{cases}, \tag{3.41}$$

and

$$\begin{cases} \omega_\alpha = \sqrt{\dfrac{\sum_{i=1}^{4} y_i^{\,2} K_z^i}{I_{xx}}} \\ \omega_\beta = \sqrt{\dfrac{\sum_{i=1}^{4} x_i^{\,2} K_z^i}{I_{yy}}} \\ \omega_\gamma = \sqrt{\dfrac{\sum_{i=1}^{4} (y_i^2 K_x^i + x_i^2 K_y^i)}{I_{zz}}} \end{cases}. \tag{3.42}$$

3.6 Conclusions

In this chapter, a mechanical mathematical model of the Permanent Magnet Synchronous Motor (PMSM) is built; the analytical equations of the critical running speed of the motor with rigid rotor support and those with flexible rotor support are derived respectively. Based on the equations, the natural frequencies of the first four modes in these two types of mounting conditions can be obtained after evaluating the motor parameters. Since the dynamic performance of the PMSM is mainly dependent on the rotor support components (bearings), two commonly-used types of bearings (FDBs and ball bearings) are analyzed. The stiffness and damping matrixes of the FDBs are different from those of ball bearings because FDBs have the coupling effect in the ***x*** and ***y*** directions. Moreover, there is a half-speed whirling frequency in FDBs. The natural frequencies of the stator teeth can be calculated by modeling the tooth as a cantilever beam. The stator core is considered as either a hollow cylinder or a cylindrical shell, depending on the relationship between the stator length and stator diameter. Consequently, the natural frequencies calculated with the combined structure exceed those based on only the stator alone. The mathematical model of the motor foundation considers the movements in the x, y and z directions, and rotating movements around the x, y and z axes. The mechanical structure mathematical models, including the rotor, bearings, stator, and the mounting foundation of the motor, are built in this chapter.

CHAPTER 4

ANALYTICAL MODELS OF EXCITATION FORCES OF PMSM

In the previous chapter, the analytical models in mechanical domain were developed to predict the natural frequencies of the Permanent Magnet Synchronous Motor (PMSM). The objective of this chapter is to develop analytical models of the excitation forces in both mechanical and electrical domains to analyze the performance of PMSM in depth.

4.1 Mechanical Unbalance

Mechanical Unbalance (MU) is a common excitation source of motor vibration. This force may cause the motor to age prematurely, thus damaging the motor components if it is not properly addressed. The dynamic response of MU due to mass eccentricity is illustrated in Figure 4.1.

The rotor's total mass is M. The rotor's eccentricity mass (m) rotates with angular velocity ω, and the distance between M and m is r, then, based on the mass spring damping theory, the force vibration equation can be built as:

$$(M-m)\ddot{x}_{(t)} + m\frac{d^2}{dt^2}[x_{(t)} + r\sin(\omega t)] + c\dot{x}_{(t)} + kx_{(t)} = 0 \quad . \tag{4.1}$$

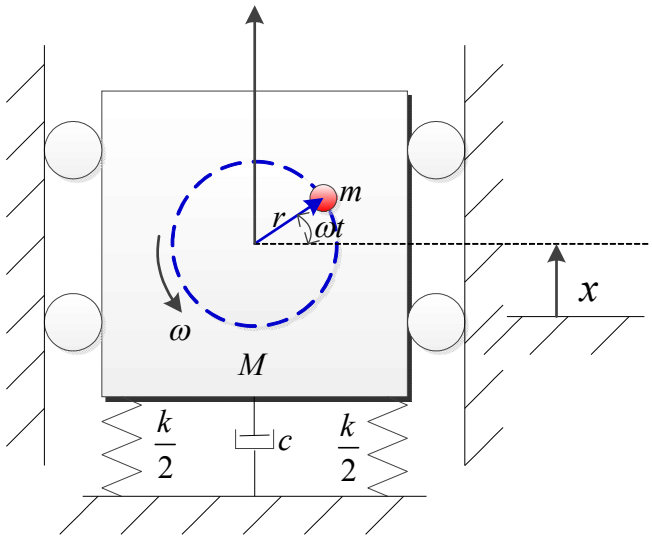

Figure 4.1: Mechanical Unbalance excitation force due to rotor mass eccentricity

Equation (4.1) can then be rearranged as:

$$M\ddot{x}_{(t)} + c\dot{x}_{(t)} + kx_{(t)} = mr\omega^2 \sin(\omega t) \quad . \tag{4.2}$$

Equation (4.2) shows the standard harmonic response of the object M. It can be observed that this force is proportional to the square of the motor's rotating speed ω.

4.2 Unbalanced Magnetic Pulls

4.2.1 Static Unbalanced Magnetic Pull

When the running motor's rotor center is offset from its stator center but does not rotate around the stator center, the motor is defined as a Static Eccentricity (SE) faulty motor. Consequently, Static Unbalanced Magnetic Pull (SUMP) will be generated. The SE fault could be induced by an ellipse of the stator core, misplacement of the rotor onto the stator, the location parts with loose machining tolerances, or the rotor being shifted down due to the wearing out of the bearing. The geometry of the section parameter of PMSM can be set, as shown in Figure 4.2.

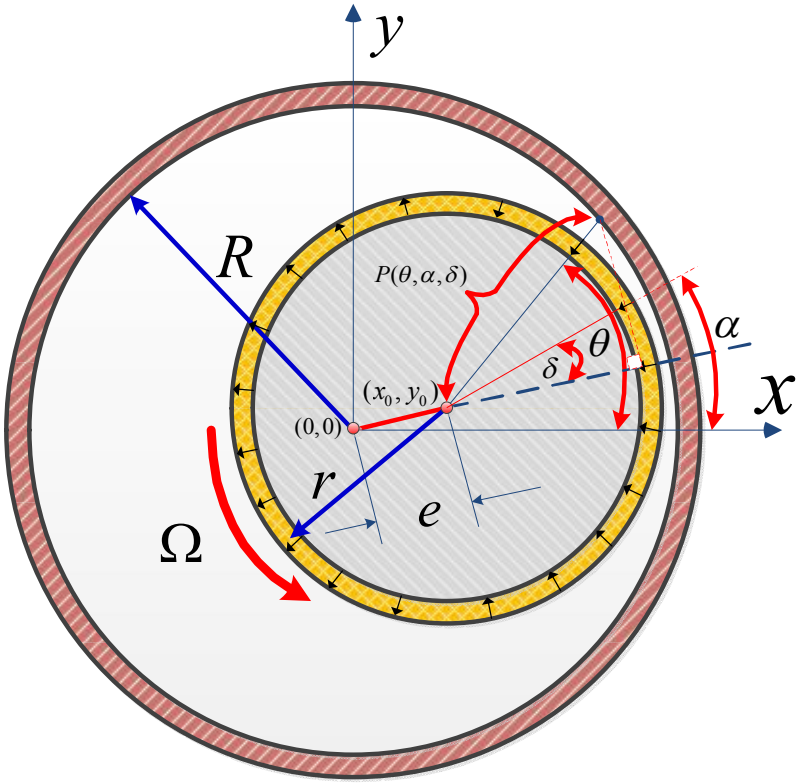

Figure 4.2: Mathematical model for calculating SUMP air-gap

The stator geometry equation can be expressed as:

$$[P(\theta,\alpha,\delta)\cos(\theta-\alpha+\delta)+e]^2+[P(\theta,\alpha,\delta)\sin(\theta-\alpha+\delta)]^2=R^2, \quad (4.3)$$

where x_0 and y_0 are the rotor center coordinates, e the distance between the rotor center and stator center, r the outer diameter of the rotor, R the inner diameter of the stator, α the rotor position in the stator coordinate, and δ the phase difference between the eccentric position and rotor position. $P(\theta,\alpha,\delta)$ can thus be deduced as:

$$P(\theta,\alpha,\delta)=-e\cos(\theta-\alpha+\delta)\pm\sqrt{R^2+e^2[\sin(\theta-\alpha+\delta)]^2} \quad . \quad (4.4)$$

As e is much smaller than R, the square root part of equation (4.4) can be expressed as:

$$P(\theta,\alpha,\delta)=R-e\cos(\theta-\alpha+\delta) \quad . \quad (4.5)$$

The eccentricity air-gap in one section can be expressed as:

$$\begin{aligned}\delta_{(\theta,\alpha,\delta)} &= P(\theta,\alpha,\delta) - r \\ &= \delta_0[1-\varepsilon\cos(\theta-\alpha+\delta)],\end{aligned} \tag{4.6}$$

where δ_0 is the average air-gap, ε relative eccentricity, and the unit permeance of the motor air-gap can be expressed as:

$$\begin{aligned}\Lambda_e(\theta,\alpha,\delta) &= \frac{\mu_0}{k_\mu \delta_{(\theta,\alpha,\delta)}} \\ &= \Lambda(\theta)/[1-\varepsilon\cos(\theta-\alpha+\delta)] \\ &\approx \Lambda(\theta)[1+\varepsilon\cos(\theta-\alpha+\delta)] \quad ,\end{aligned} \tag{4.7}$$

and

$$\Lambda(\theta) = \Lambda_0[1+\sum_{n=0}\lambda_{An}\cdot\cos(nZ\theta)] \quad , \tag{4.8}$$

where μ_0 is the permeability of vacuum, Z the number of stator slot, λ_n the coefficient of the nth order unit permeance of the air-gap, and Λ_0 the average permeance of the air-gap, which is related to ε. Λ_0 is also linked with the thickness and permeability of the magnet, and the stator slot structure.

In the motor operation, the magnetic-motive-force (MMF) generated by the PM ring can be described by:

$$F_R(\theta,\alpha) = \sum_{n=0} F_{R2n-1}\sin[(2n-1)p(\theta+\alpha)] \quad , \tag{4.9}$$

where θ is the position of the field, p the pole-pair of the PM ring, and α the rotor phase difference w.r.t. the stator reference point. It is clear that α is a function of time and rotor speed.

Using the magnetic-circuit method, the effective magnetic flux density in the air-gap can be expressed as:

$$B_A(\theta,\alpha,\delta) = \Lambda_e(\theta,\alpha,\delta)\cdot F_R(\theta,\alpha) \quad . \tag{4.10}$$

The local radial force area density at position θ can thus be calculated by:

$$p_A(\theta,\alpha,\delta)=\frac{1}{2\mu_0}B_A^2(\theta,\alpha,\delta) \quad . \tag{4.11}$$

where μ_0 is the permeability of the vacuum.

Therefore, the UMP, $P_A(\alpha,\delta)$, can be calculated by the following:

$$\begin{aligned} P_A(\alpha,\delta) &= \int_0^{2\pi} p_A(\theta,\alpha,\delta)R_A d\theta \\ &= \frac{R_A}{2\mu_0}\int_0^{2\pi} B_A^2(\theta,\alpha,\delta)d\theta \\ &= \frac{R_A}{2\mu_0}\int_0^{2\pi} \Lambda_e^2(\theta,\alpha,\delta)F_R^2(\theta,\alpha,\delta)d\theta \quad , \end{aligned} \tag{4.12}$$

where R_A is the average radius of the air-gap.

From equations (4.7) and (4.9), it can be known that

$$\begin{aligned} \Lambda_e^2(\theta,\alpha,\delta) &= \sum_{m=0} l_{Am}\cdot\cos(mZ\theta)\times[1+\varepsilon\cos(\theta-\alpha+\delta)]^2 \\ &\approx \sum_{m=0} l_{Am}\cdot\cos(mZ\theta)\times[1+2\varepsilon\cos(\theta-\alpha+\delta)] \quad , \end{aligned} \tag{4.13}$$

and

$$F_A^2(\theta,\alpha)=\sum_{n=0} f_{A2n}\cdot\cos[(2np(\theta-\alpha)] \quad . \tag{4.14}$$

The definitions of l_{AM} and f_{An} can be found in [29].

Using the results shown in equations (4.13) and (4.14), the UMP can be deduced as:

$$\begin{aligned} P_A(\alpha,\delta) = \frac{R_A}{2\mu_0}\times\int_0^{2\pi}[\sum_{m=0} l_{Am}\cdot\cos(mZ\theta)]\cdot[1+2\varepsilon\cos(\theta-\alpha+\delta)] \\ \cdot\sum_{n=0} f_{A2n}\cdot\cos[2np(\theta-\alpha)]d\theta \quad , \end{aligned} \tag{4.15}$$

and

$$P_{AI}(\alpha)=\frac{R_A}{2\mu_0}\times\int_0^{2\pi}[\sum_{m=0} l_{Am}\cdot\cos(mZ\theta)]\cdot\sum_{n=0} f_{A2n}\cdot\cos[2np(\theta-\alpha)]d\theta \quad , \tag{4.16}$$

where $P_{AI(\alpha)}$ is just the component caused by the EM structure reported in [29] as intrinsic UMP.

For the UMP due to static eccentricity, $P_{AE(\alpha,\delta)}$ can be expressed as:

$$P_{AE}(\alpha)=\frac{\varepsilon R_A}{2\mu_0}\times\int_0^{2\pi}\sum_{m=0}l_{Am}\cdot\{\cos[(mZ+1)\theta-\alpha+\delta]+\cos[(mZ-1)\theta-\alpha+\delta]\}\cdot\sum_{n=0}f_{A2n}\cdot\cos[2np(\theta-\alpha)]d\theta \quad , \tag{4.17}$$

Therefore, the static UMP in ***x*** direction can be expressed as:

$$P_{AE\_X}(\alpha)=\frac{\varepsilon R_A}{2\mu_0}\times\int_0^{2\pi}\sum_{m=0}l_{Am}\cdot\{\cos[(mZ+2)\theta-\alpha+\delta]+\cos[(mZ-2)\theta-\alpha+\delta]\}\times\sum_{n=0}f_{A2n}\cdot\cos[2np(\theta-\alpha)]d\theta \quad , \tag{4.18}$$

From the orthogonality of the triangular function, it can be known that the integrations of all the items in equation (4.18) are zero after being integrated from 0 to 2π, except the items which meet the following condition:

$$\begin{cases}2np=mZ\pm2\\2np=mZ\end{cases} \quad . \tag{4.19}$$

Equation (4.18) can be simplified as:

$$\begin{aligned}P_{AE\_X}(\alpha,\delta)=\frac{\varepsilon R_A\pi}{2\mu_0}\times\{&\sum_m f_{A2n}l_{Am}\cdot\cos[2np\alpha-(\alpha-\delta)]|_{2np=mZ+2}\\&-\sum_m f_{A2n}l_{Am}\cdot\cos[2np\alpha+(\alpha-\delta)]|_{2np=mZ-2}\\&+\sum_m f_{A2n}l_{Am}\cdot\cos[2np\alpha-(\alpha-\delta)]|_{2np=mZ}\\&-\sum_m f_{A2n}l_{Am}\cdot\cos[2np\alpha+(\alpha-\delta)]|_{2np=mZ}\}\end{aligned} \quad . \tag{4.20}$$

Using the same procedure, the UMP in ***y*** direction can be obtained and expressed as:

$$\begin{aligned}P_{AE\_Y}(\alpha)=\frac{\varepsilon R_A\pi}{2\mu_0}\times\{&\sum_m f_{A2n}l_{Am}\cdot\sin[2np\alpha-(\alpha-\delta)]|_{2np=mZ+2}\\&-\sum_m f_{A2n}l_{Am}\cdot\sin[2np\alpha+(\alpha-\delta)]|_{2np=mZ-2}\\&+\sum_m f_{A2n}l_{Am}\cdot\sin[2np\alpha-(\alpha-\delta)]|_{2np=mZ}\\&-\sum_m f_{A2n}l_{Am}\cdot\sin[2np\alpha+(\alpha-\delta)]|_{2np=mZ}\}\end{aligned} \quad . \tag{4.21}$$

The assumption is that the rotor core's effective length is L_0, the motor global SUMP in x and y can thus be expressed as:

$$\begin{cases} P_{GE\_X}(\alpha) = P_{AE\_X}(\alpha) \times L_0 \\ P_{GE\_Y}(\alpha) = P_{GE\_Y}(\alpha) \times L_0 \end{cases}. \quad (4.22)$$

Deduction 4.2.1

From the analysis in this section, the following deductions can be obtained.

1) SUMP has a constant component in eccentricity direction only.
2) In one motor revolution, the lowest order of the SUMP harmonic is two times its pole-pair number.
3) The order of the SUMP harmonic is independent of the eccentricity.

4.2.2 Dynamic Unbalanced Magnetic Pull

When a running motor has its rotor center offset from its stator center, and the rotor center also rotates around the stator center, the motor is called a dynamic eccentricity (DE) faulty motor. As a result, Dynamic Unbalanced Magnetic Pull (DUMP) of the DE motor will be generated by the relative movement between the rotor and stator. The DE fault could be induced by an ellipse of the rotor yoke, bending of the rotor shaft, misalignment of the rotor yoke and rotor shaft, and misplacement of the segment magnet. Similar to SUMP, one section of the PMSM with DE fault can be taken, and the geometry of the section parameter can be set, as in Figure 4.3. The stator geometry equation can be expressed as:

$$\{P(\theta,\alpha,\beta)\cos[\theta-(\alpha+\beta)]+e\}^2+\{P(\theta,\alpha,\beta)\sin[\theta-(\alpha+\beta)]\}^2=R^2, \quad (4.23)$$

where e is the offset of the rotor geometry center from the stator geometry center, r the outer diameter of the rotor, and R the inner diameter of the stator. $P(\theta, \alpha, \beta)$ can then be expressed as:

$$P(\theta,\alpha,\beta) = -e\cos[\theta-(\alpha+\beta)] \pm \sqrt{R^2+e^2\{\sin[\theta-(\alpha+\beta)]\}^2} \quad . \tag{4.24}$$

From Figure 4.3, it can be observed that $P(\theta, \alpha, \delta)$ is larger than zero, and $esin(\theta-\alpha+\delta)/R$ much less than unity. Equation (4.24) can then be expressed as:

$$P(\theta,\alpha,\beta) = R - e\cos[\theta-(\alpha+\beta)] \quad . \tag{4.25}$$

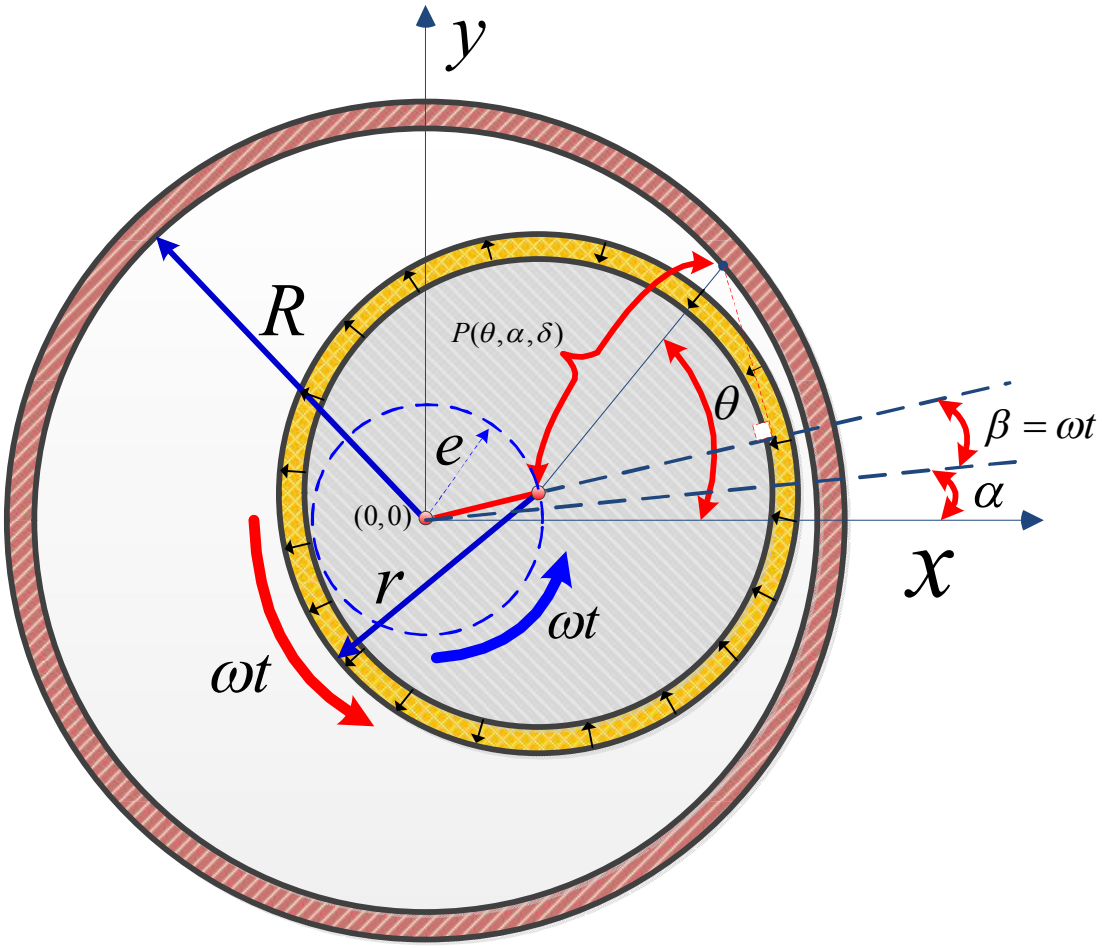

Figure 4.3: Mathematical model for calculating DUMP air-gap

The dynamic eccentricity air-gap in one section can be expressed as:

$$\begin{aligned}\delta_{(\theta,\alpha,\beta)} &= P(\theta,\alpha,\beta) - r \\ &= \delta_0\{1-\varepsilon\cos[\theta-(\alpha+\beta)]\} \\ &= \delta_0\{1-\varepsilon\cos[\theta-(\omega t+\alpha)]\} \quad .\end{aligned} \tag{4.26}$$

Using a similar deductive inference procedure, the DUMP in x and y directions can be obtained by simply changing α to ωt+α in equations (4.20) and (4.21), and these are expressed by:

$$\begin{aligned} P_{AE\_X}(\alpha,\beta) = \frac{\varepsilon R_A \pi}{2\mu_0} \times \{ & \sum_m f_{A2n} l_{Am} \cdot \cos[(2np-1)(\omega t+\alpha)]|_{2np=mZ+2} \\ & -\sum_m f_{A2n} l_{Am} \cdot \cos[(2np+1)(\omega t+\alpha)]|_{2np=mZ-2} \\ & +\sum_m f_{A2n} l_{Am} \cdot \cos[(2np-1)(\omega t+\alpha)]|_{2np=mZ} \\ & -\sum_m f_{A2n} l_{Am} \cdot \cos[(2np+1)(\omega t+\alpha)]|_{2np=mZ}\} \end{aligned} , \quad (4.27)$$

and

$$\begin{aligned} P_{AE\_Y}(\alpha,\beta) = \frac{\varepsilon R_A \pi}{2\mu_0} \times \{ & \sum_m f_{A2n} l_{Am} \cdot \sin[(2np-1)(\omega t+\alpha)]|_{2np=mZ+2} \\ & -\sum_m f_{A2n} l_{Am} \cdot \sin[(2np+1)(\omega t+\alpha)]|_{2np=mZ-2} \\ & +\sum_m f_{A2n} l_{Am} \cdot \sin[(2np-1)(\omega t+\alpha)]|_{2np=mZ} \\ & -\sum_m f_{A2n} l_{Am} \cdot \sin[(2np+1)(\omega t+\alpha)]|_{2np=mZ}\} \end{aligned} . \quad (4.28)$$

It can be observed in equations (4.27) and (4.28) that the amplitudes and harmonic frequencies of the DUMP in the motor will link with the pole pair and stator slot number. However, there is always a fundamental frequency component when n = 0. We assume the length of motor rotor yoke is L_0. The global fundamental DUMP in motor can then be expressed as:

$$P_{GE\_X}(\alpha,\omega,t) = \frac{\varepsilon R_A L_0 \pi}{2\mu_0} f_{A0} l_{A0} \cos(\omega t+\alpha) \quad , \quad (4.29)$$

and

$$P_{GE\_Y}(\alpha,\omega,t)=\frac{\varepsilon R_A L_0 \pi}{2\mu_0} f_{A0} l_{A0} \sin(\omega t+\alpha) \quad , \tag{4.30}$$

Deduction 4.2.2

From the analysis in this section, the following deductions can be obtained.

1) DUMP does not have any constant component in all directions.
2) In one motor revolution, the lowest order of the DUMP harmonic is the same frequency as the motor speed.
3) In one motor revolution, the second lowest order of the DUMP harmonic is two times its pole-pair number either minus or plus one depending on the combination of the motor pole-pair number and slot number .
4) The order of the DUMP harmonic is independent on the eccentricity.
5) The amplitude of DUMP increases with increasing dynamic eccentricity distance.

4.2.3. Inclined Unbalanced Magnetic Pull

Motors with self-aligning bearings can eliminate the rotor bending force; this type of bearing is shown in Figure 4.4. However, as the mechanical structure is easily misaligned, the magnetic field generated by the permanent magnet on the rotor acts with the stator core to generate more UMPs in the motor operation.

Although the machining tolerances of the rotor and stator have been improved, the motor assembly tolerance gaps still exist and may generate a rotor-misalignment type of eccentricity which is defined as Inclined Eccentricity (IE). This type of eccentricity will generate the Inclined Unbalanced Magnetic Pull (IUMP), which may create major vibrations because of the smaller air-gap and lower machining tolerances. There are four types of misalignment, which are shown in Figures 4.5 to 4.8.

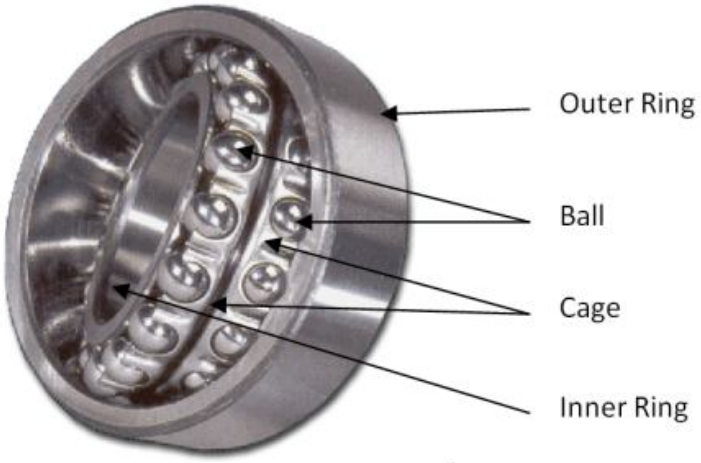

Figure 4.4: Self-aligning ball bearing [63]

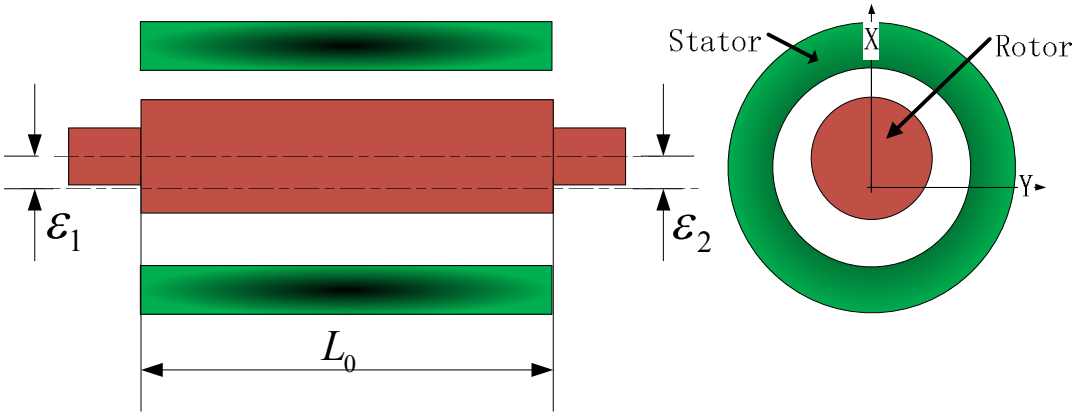

Figure 4.5: Motor with two ends of rotor upward from stator center with the same distance

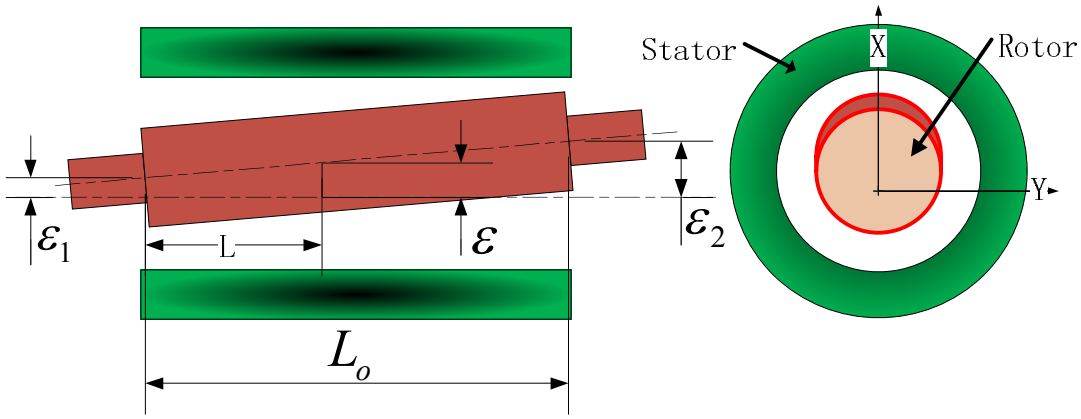

Figure 4.6: Motor with two ends of rotor upward from stator center with different distances

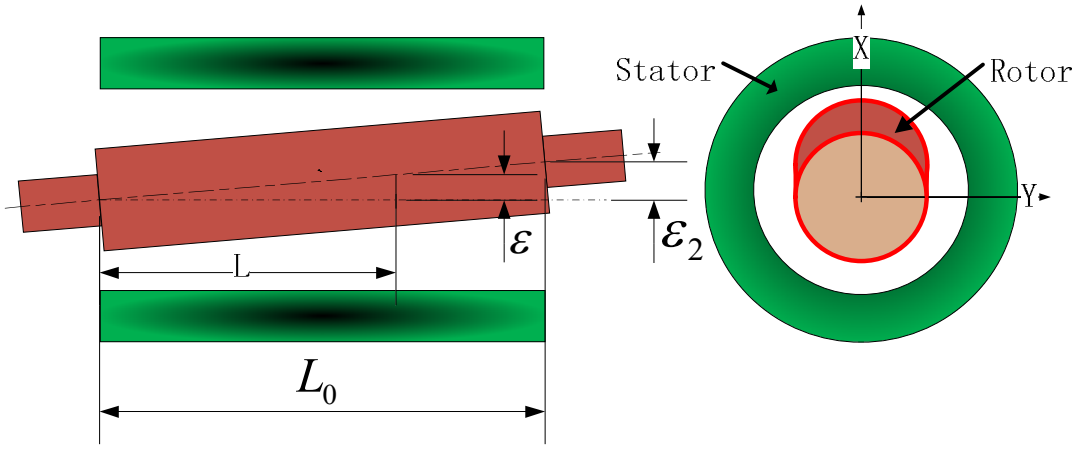

Figure 4.7: Motor with one end of rotor upward from stator center

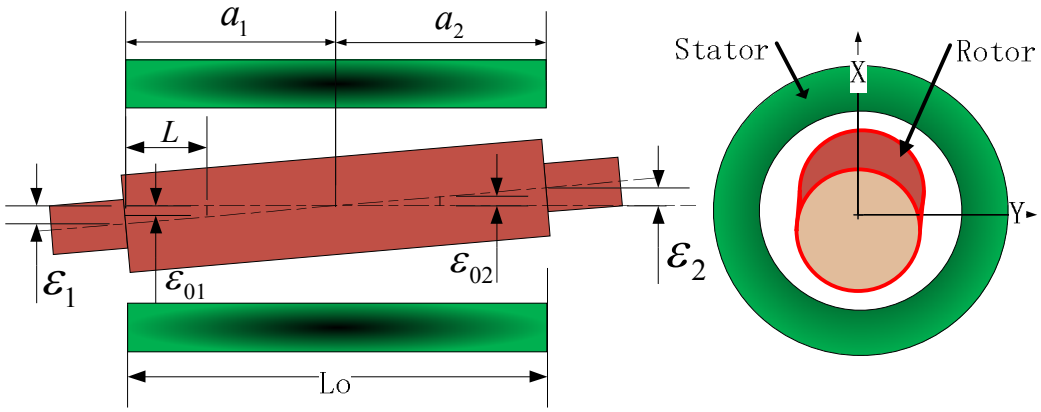

Figure 4.8: Motor with one end of rotor upward from stator center and another end of rotor downward from stator center

In this chapter, we will concentrate on analyzing the effects of the IUMP caused by uneven rotor misalignment in the axial direction. The influence of the drive current on the air-gap field, reported in [30], will be ignored in this thesis.

It can be seen that the type-1 misalignment in Figure 4.5 is the same as static eccentricity, which has already been studied in a previous section of this chapter. For type-2, the eccentricity of any section shown in Figure 4.6 can be expressed as:

$$\varepsilon = \varepsilon_1 + \frac{L}{L_0}(\varepsilon_2 - \varepsilon_1) \quad , \tag{4.31}$$

where L is the distance from the reference point to the point where the section UMP force is calculated, and L_O is the effective length of the stator core of the motor. Therefore, the global IUMP in x and y can be obtained by simply subtracting equation (4.31) to equations (4.20) and (4.21). To simplify the expression in the following analysis, we define CoP_{GE_X} and $\underline{CoP_{GE\_Y}}$ in equations (4.20) and (4.21) and express them as:

$$\begin{aligned} C_O P_{GE\_X} = \{ & \sum_m f_{A2n} l_{Am} \cdot \cos[2np\alpha - (\alpha - \delta)]|_{2np=mZ+2} \\ & - \sum_m f_{A2n} l_{Am} \cdot \cos[2np\alpha + (\alpha - \delta)]|_{2np=mZ-2} \\ & + \sum_m f_{A2n} l_{Am} \cdot \cos[2np\alpha - (\alpha - \delta)]|_{2np=mZ} \\ & - \sum_m f_{A2n} l_{Am} \cdot \cos[2np\alpha + (\alpha - \delta)]|_{2np=mZ} \} \end{aligned} , \tag{4.32}$$

and

$$\begin{aligned} C_O P_{GE\_Y} = \{ & \sum_m f_{A2n} l_{Am} \cdot \sin[2np\alpha - (\alpha - \delta)]|_{2np=mZ+2} \\ & - \sum_m f_{A2n} l_{Am} \cdot \sin[2np\alpha + (\alpha - \delta)]|_{2np=mZ-2} \\ & + \sum_m f_{A2n} l_{Am} \cdot \sin[2np\alpha - (\alpha - \delta)]|_{2np=mZ} \\ & - \sum_m f_{A2n} l_{Am} \cdot \sin[2np\alpha + (\alpha - \delta)]|_{2np=mZ} \} \end{aligned} . \tag{4.33}$$

Therefore, in Figure 4.6, the global IUMP in the ***x*** and ***y*** direction can be expressed as:

$$P_{GE\_X}(\alpha, \delta) = \frac{(\varepsilon_1 + \varepsilon_2) L_0 R_A \pi}{4\mu_0} \times CoP_{GE\_X} , \tag{4.34}$$

and

$$P_{GE\_Y}(\alpha,\delta)=\frac{(\varepsilon_1+\varepsilon_2)L_0R_A\pi}{4\mu_0}\times CoP_{GE\_Y} \quad . \tag{4.35}$$

The type-3 misalignment is in, Figure 4.7, let ε_1 equal zero, and the global IUMP in x, y can be obtained, which is expressed by:

$$P_{GE\_X}(\alpha,\delta)=\frac{\varepsilon_2L_0R_A\pi}{4\mu_0}\times CoP_{GE\_X} \quad , \tag{4.36}$$

and

$$P_{GE\_X}(\alpha,\delta)=\frac{\varepsilon_2L_0R_A\pi}{4\mu_0}\times CoP_{GE\_Y} \quad . \tag{4.37}$$

For type-4, calculation of the global radial IUMP of a motor with an unevenly misaligned rotor on different sides, as shown in Figure 4.8, is more complicated. The eccentricity of the section between 0~a_1 and a_1~L_0 can be respectively expressed as:

$$\begin{cases}\varepsilon_{01}=\dfrac{a_1-L}{a_1}\varepsilon_1\\ \varepsilon_{02}=\dfrac{L-a_1}{a_2}\varepsilon_2\end{cases}, \tag{4.38}$$

and

$$a_1=\frac{\varepsilon_1}{\varepsilon_1+\varepsilon_2}L_0, \tag{4.39}$$

where ε_2 is assumed to be larger than ε_1, and therefore, when we define the IUMP in the range $a_1 \sim L_0$ as positive, the IUMP in the range $0 \sim a_1$ should be negative. In Figure 4.8, the type-4 global IUMP in x and y directions can be calculated and expressed as:

$$
\begin{aligned}
P_{GE\_X}(\alpha,\delta) &= [-\frac{R_A\pi}{2\mu_0}\int_0^{a_1}\frac{a_1-L}{a_1}\varepsilon_1 dL + \frac{R_A\pi}{2\mu_0}\int_{a_1}^{L_0}\frac{L-a_1}{a_2}\varepsilon_2 dL] \\
&\times CoP_{GE\_X} \\
&= \frac{2L_0^2-2a_1L_0+a_1^2-a_1a_2}{2a_2}\times\frac{R_A\pi}{2\mu_0}\times CoP_{GE\_X} \\
&= \frac{2\varepsilon_1^2+\varepsilon_1\varepsilon_2+2\varepsilon_2^2}{2\varepsilon_2}\times\frac{R_A\pi}{2\mu_0}\times CoP_{GE\_X}
\end{aligned}
\quad , \tag{4.40}
$$

and

$$
\begin{aligned}
P_{GE\_Y}(\alpha,\delta) &= [-\frac{R_A\pi}{2\mu_0}\int_0^{a_1}\frac{a_1-L}{a_1}\varepsilon_1 dL + \frac{R_A\pi}{2\mu_0}\int_{a_1}^{L_0}\frac{L-a_1}{a_2}\varepsilon_2 dL] \\
&\times CoP_{GE\_Y} \\
&= \frac{2L_0^2-2a_1L_0+a_1^2-a_1a_2}{2a_2}\times\frac{R_A\pi}{2\mu_0}\times CoP_{GE\_Y} \\
&= \frac{2\varepsilon_1^2+\varepsilon_1\varepsilon_2+2\varepsilon_2^2}{2\varepsilon_2}\times\frac{R_A\pi}{2\mu_0}\times CoP_{GE\_Y}
\end{aligned}
\quad . \tag{4.41}
$$

Deduction 4.2.3

From the analysis in this section, the following deductions can be obtained.

1) IUMP has a constant component in the eccentricity direction only.
2) In one motor revolution, the lowest order of the IUMP harmonic is two times its pole-pair number.
3) The order of the IUMP harmonic is independent on the eccentricity.
4) The amplitude of IUMP increases with dynamic eccentricity distance.

4.2.4. Axial Unbalanced Magnetic Pull

For realizing some special characteristics, many PMSMs have the rotor aligned asymmetrically in the axial direction (Z-asymmetrical rotor). For example, many PMSMs use a Hall sensor to detect the rotor position.

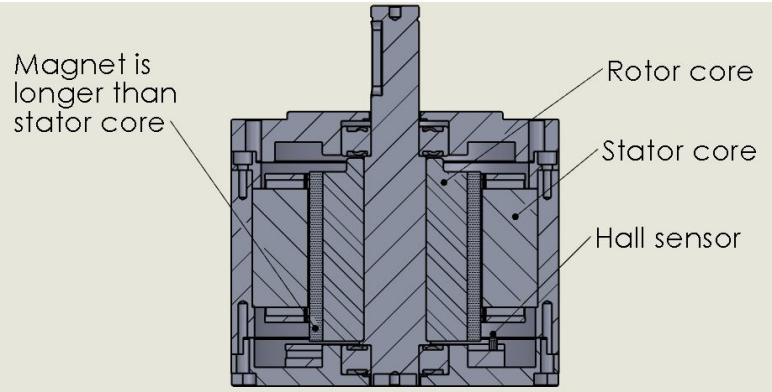

Figure 4.9: PMSM motor with the rotor aligned asymmetrically in axial direction

For the PMSM driven with Hall sensor, to make the rotor's magnetic field to be clearly detectable, the rotor is aligned asymmetrically in the axial direction, bringing the sensors close to the magnet. This is shown in Figure 4.9.

As the mechanical structure is axially asymmetrical, the magnetic field generated by the permanent magnet on the rotor acts with the stator core and generates an additional UMP in the motor operation. We can define this type of UMP as Axial Unbalanced Magnetic Pull (AUMP).

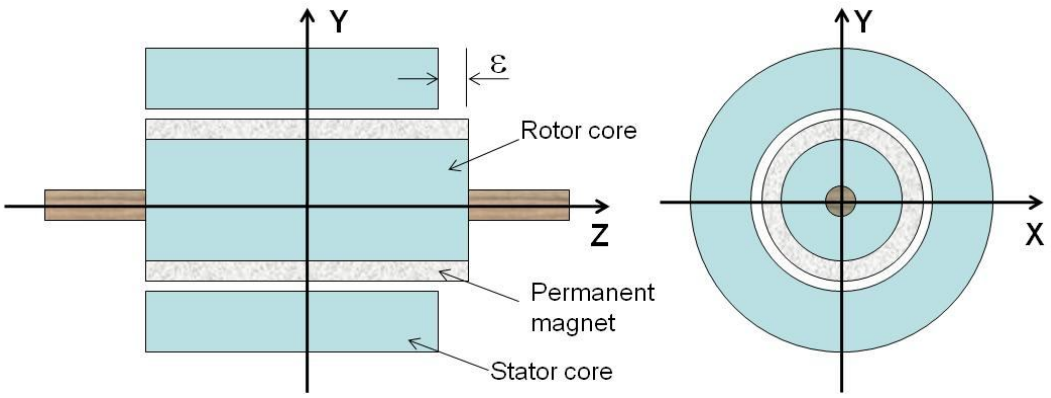

Figure 4.10: A simplified model for describing the PMSM with Z-asymmetrical rotor (outer stator shorter than inner rotor)

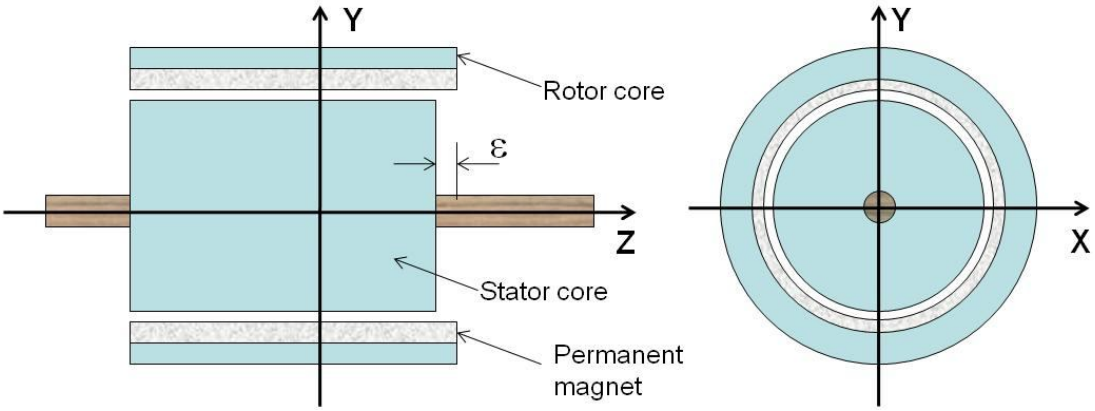

Figure 4.11: A simplified model for describing the PMSM with Z-asymmetrical rotor (inner stator shorter than outer rotor)

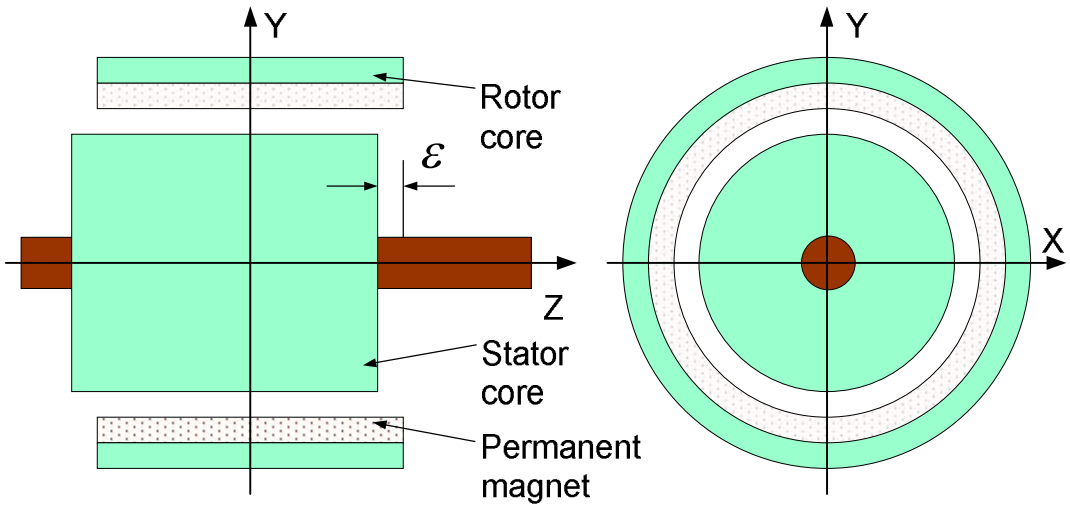

Figure 4.12: A simplified model for describing the PMSM with Z-asymmetrical rotor (outer rotor and stator with equal length)

Figures 4.10 and 4.11 depict the simplified electromagnetic (EM) models of PMSM with Z-asymmetrical inner and outer rotors, respectively. From the viewpoint of magnetic circuit analysis, there is no difference between the models for analyzing the PMSM with the inner and outer rotors. Figure 4.12 shows the EM model of the PMSM with Z-asymmetrical on the same length of outer rotor and inner stator

configuration. This structure is used in the case where the AUMP is necessary, and saving magnetic material is important.

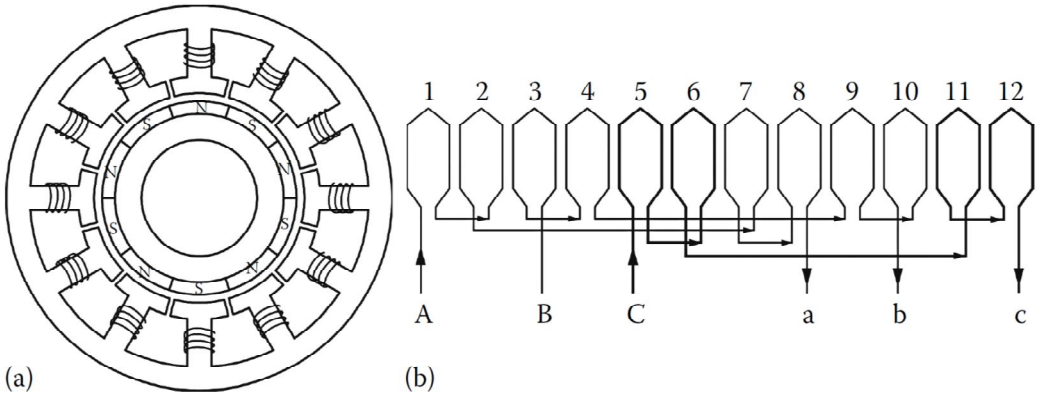

Figure 4.13: A concentrated coil-wound spindle motor with 12 slots and 5 magnetic pole-pairs
(a): machine schematic; (b) winding diagram [64]

The magnetic field on the axial edge of the motor is not only related to the permanent magnets on the rotor, but also to the stator core structure, especially the slots on the core. If there is no slot on the stator, the geometrical relationship between the rotor and the stator is fixed, i.e., from the viewpoint of the rotor, the magnetic relationship between the rotor and stator is not affected by the rotor position. In this case, as the field generated by the armature winding currents in the axial edge is normally much weaker than the field generated by the magnet, the magnetic pull produced by the permanent magnet is constant. It also means, for the slot-less PMSM motor, that if the AUMP in one rotor position can be known, the AUMP in the other position can also be known.

However, the existence of the stator slots makes the geometrical relationship between the rotor and stator complicated. The influence of the edgy magnetic field varies with the rotor rotation. This makes the AUMP vary with the rotor rotation.

The machine schematic and winding diagrams of the PMSM are shown in Figure 4.13, and the three-dimensional structure is illustrated in Figure 4.14.

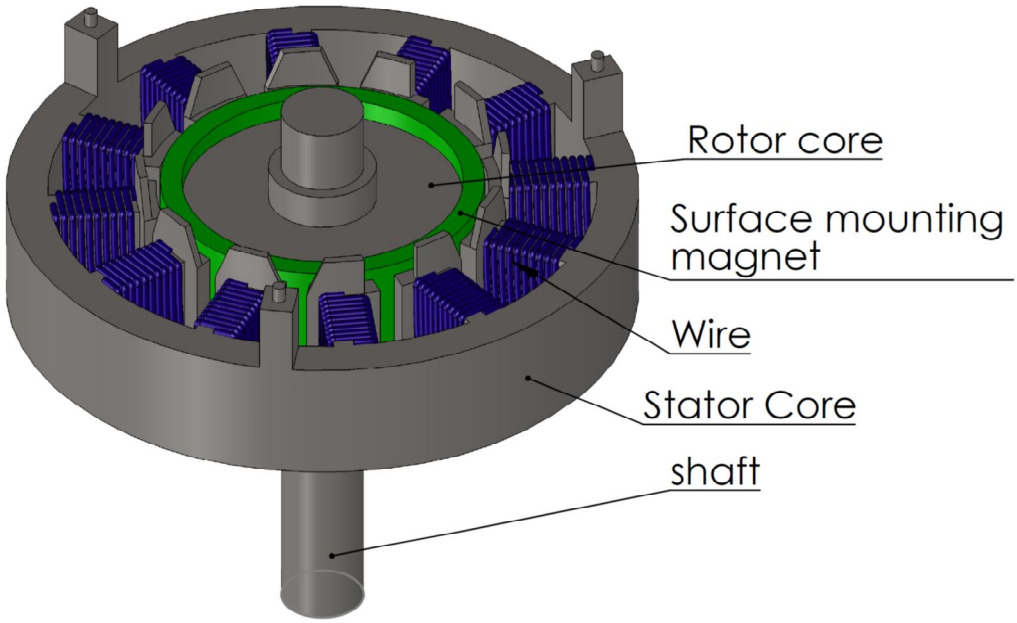

Figure 4.14: Three-dimensional structure of a spindle motor with 12 slots and 5 magnetic pole-pairs

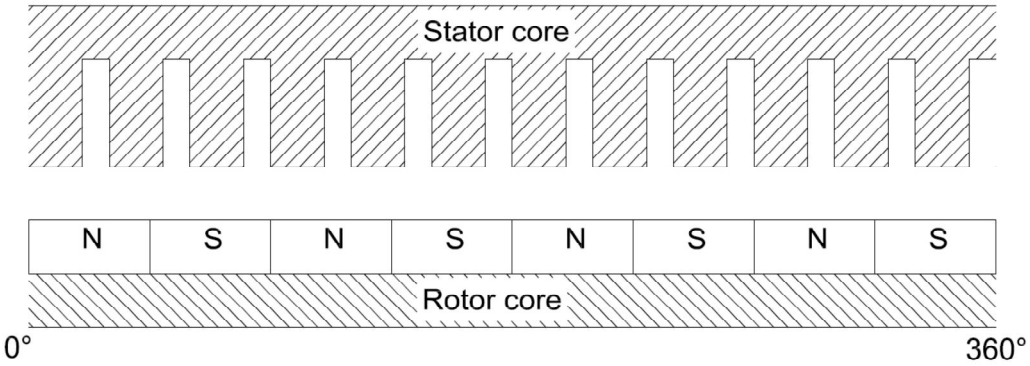

Figure 4.15: A simplified model describing the variation of the air-gap of axial edgy of the spindle motor

Using the magnetic circuit method, the effective air-gap of the motor axial edge can be expressed with the simplified model shown in Figure 4.15. From the viewpoint of the rotor, the length of the local air-gap changes when the rotor is in

different positions. From Figure 4.15, the effective permeance of the axial edgy air-gap can be expressed as:

$$\Lambda_A(\theta) = \Lambda_{A0}[1 + \sum_{n=0} \lambda_{An} \cdot \cos(nZ\theta)], \tag{4.42}$$

where Λ_{A0} is the effective average permeance of the air-gap, which is related with ε_A. For the difference between the lengths of the rotor and stator; see Figures 4.10 and 4.11. Λ_{A0} is also linked with the thickness and permeability of the magnet, and the stator slot structure. Z is the number of stator slots and λ_{An} is the coefficient of the nth order unit permeance of the air-gap.

In the motor operation, the magnetic-motive-force (mmf) generated by the PM ring can be expressed as:

$$F_A(\theta, \alpha) = \sum_{n=0} K_{A,2n-1} \sin[(2n-1)p(\theta + \alpha)], \tag{4.43}$$

where θ is the position of the field, p the pole-pair of the PM ring, and α the rotor phase difference from the stator reference point.

Using the magnetic-circuit method, the effective magnetic flux density in the air-gap can be expressed as:

$$B_A(\theta, \alpha) = \Lambda_A(\theta) \cdot F_A(\theta, \alpha). \tag{4.44}$$

The local radial force area density at position θ can thus be calculated by:

$$p_A(\theta, \alpha) = \frac{\nu_0}{2} B_A^2(\theta, \alpha) \quad . \tag{4.45}$$

where μ_0 is the permeability of the vacuum.

Therefore, the AUMP, $P_A(\alpha)$, can be calculated using the following equation:

$$\begin{aligned} P_A(\alpha) &= \varepsilon_A \int_0^{2\pi} p_A(\theta,\alpha) R_A d\theta = \frac{\varepsilon_A R_A}{2\mu_0} \int_0^{2\pi} B_A^2(\theta,\alpha) d\theta \\ &= \frac{\varepsilon_A R_A}{2\mu_0} \int_0^{2\pi} \Lambda_A^2(\theta) F_A^2(\theta,\alpha) d\theta \end{aligned} \quad , \tag{4.46}$$

where ε_A is the effective length difference between the stator core and permanent magnet in Figures 4.10 and 4.11. R_A is the average radius of the air-gap.

From equations (4.42) and (4.43), it can be known that,

$$\Lambda_A^2(\theta) = \sum_{m=0} l_{Am} \cdot \cos(mZ\theta)] \quad , \tag{4.47}$$

and

$$F_A^2(\theta,\alpha) = \sum_{n=0} f_{An} \cdot \cos[(2np(\theta-\alpha)] \quad . \tag{4.48}$$

The definitions of l_{Am} and f_{An} can be found in [29].

Using the results shown in equations (4.47) and (4.48) , the UMP can be expressed as:

$$P_A(\alpha) = \frac{\varepsilon_A R_A}{2\mu_0} \times \int_0^{2\pi} [\sum_{m=0} l_{Am} \cdot \cos(mZ\theta)] \sum_{n=0} f_{A2n} \cdot \cos[2np(\theta-\alpha)] d\theta \quad . \tag{4.49}$$

From the orthogonality of the triangular function, it can be known that the integrations of all the items in equation (4.49) are zero, except for the items which can meet the following condition: $mZ = 2np$. Therefore, the following result can be obtained:

$$\begin{aligned} & P_A(\alpha) \\ &= \frac{\varepsilon_A R_A \pi}{2\mu_0} \sum_{m=0} l_{Am} [\sum_{n=0} f_{A2n} \cos(2np\alpha)] \Big|_{mZ=2np} \\ &= P_{A0} + \frac{\varepsilon_A R_A \pi}{2\mu_0} \sum_q [l_{Aq} f_{Aq} \cos(q\alpha)] \end{aligned} \tag{4.50}$$

where P_{A0} is the zero order of the AUMP and q is the common multiple of mZ and $2np$. Therefore, it is possible that P_A changes in motor operation.

Deduction 4.2.4

From the analysis in this section, the following deductions can be obtained.

1) AUMP has a constant component in the axial direction only. This constant component is normally the maximum component in AUMP. Its value can be predetermined by the lengths of the rotor magnet and stator core, and the specification of magnetic material.
2) In one motor revolution, the lowest order of the AUMP harmonic is the Least common Multiple (LCM) of its pole number and slot number.

4.3 Conclusions

In this chapter, the vibration excitation forces are analyzed with analytical models in mechanical and electromagnetic domain.

The analysis results show that, the Mechanical Unbalance (MU) force is proportional to the eccentricity mass on the rotor and the distance between the centre of the eccentricity mass and the rotor rotating center, moreover, the force is also proportional to the square of the rotating speed of the rotor. The fundamental frequency of the MU force is $1\times$ order of the rotor's mechanical rotating speed. The motor's Unbalanced Magnetic Pulls (UMPs) could be generated by various rotor eccentricity faults. UMPs can be classified as Static Unbalanced Magnetic Pull (SUMP), Dynamic Unbalanced Magnetic Pull (DUMP), Inclined Unbalanced Magnetic Pull (IUMP), and Axial Unbalanced Magnetic Pull (AUMP), according to the various types of eccentricity faults. SUMP has constant offset components in the offset direction of the rotor center. This constant force is in direct proportion to the rotor eccentricity distance, the average radius of the air-gap and the motor stator length. However, there is no constant force in the orthogonal direction of the eccentricity. The fundamental frequency of SUMP is $P\times$ order, where P stands for the motor pole number. On the other hand, the DUMP does not have the constant force component as it varies with the rotor's mechanical rotating position. The fundamental frequency of the DUMP is $1\times$ order and the second lowest frequency is

either ($P+1$) × order or ($P-1$) × order depending on the motor pole number and slot number combination. The amplitude of the DUMP is also proportional to the motor eccentricity distance, average radius of the air-gap and motor stator length. The DUMP in y direction has a 90 degree phase shift from that in x direction. The IUMP is a more general version of the SUMP. As shown in Figure 4.5, the SUMP is the first type of IUMP. The IUMP on the rotor is not only dependent on the eccentricity distance in the two side support systems, but also on the offset direction. Evaluating the effectiveness of this type of UMP is very complicated, and detailed calculations will be shown in Chapter 5. However, the fundamental frequency of IUMP is the same as SUMP. Unlike aforementioned SUMP, DUMP, and IUMP generated by the radius direction eccentricity of the rotor, the AUMP is the excitation force generated by the axial direction eccentricity. The AUMP not only has a constant component P_{A0}, but it also has components that vary with the rotor's mechanical rotating frequency. The second part of the AUMP is proportional to the axial eccentricity and the average radial of the air-gap, but is not dependent on the stator's effective length. The fundamental frequency of AUMP is the Least common Multiple (LCM) × order.

CHAPTER 5

NUMERICAL COMPUTATION OF UNBALANCED MAGNETIC PULL AND MECHANICAL UNBALANCED FORCE IN MOTOR

In the previous chapter, it was mentioned that Mechanical Unbalance (MU) and Unbalanced Magnetic Pulls (UMPs) are the sources causing the vibration and acoustic noise of the permanent magnet synchronous motor (PMSM). The analytical models have been developed to predict MU and four types of UMPs. Due to the complicated geometries, only stator, air-gap, and rotor have to be modeled through finite element method (FEM). The purpose of this chapter is to verify the faulty frequencies predicted in the previous chapter with numerical analysis.

5.1 Fundamental theory of electromagnetic force calculation

Maxwell's equations represent an elegant way to describe the fundamentals of electricity and magnetism. They include Gauss's law of electricity, Gauss's law for magnetism, Faraday's law of induction, and Ampere's law of electrical circuits. Maxwell's equations have an integral form and differential form,

$$\begin{cases} \nabla \cdot E = 4\pi k\rho \\ \nabla \cdot B = 0 \\ \nabla \times E = -\dfrac{\partial B}{\partial t} \\ \nabla \times B = \dfrac{4\pi k}{c^2} J + \dfrac{1}{c^2}\dfrac{\partial E}{\partial t} \end{cases}, \tag{5.1}$$

where k=1/(4πε$_0$) is Coulomb's constant and c^2=1/($\mu_0\varepsilon_0$).

5.2 Introduction of Finite Element Method on Magnetic Field studies

The finite element method (FEM), originally introduced by Turner et al. (1956), is a powerful computational technique that is able to generate approximate solutions to a variety of "real-world" engineering problems with complex domains subjected to general boundary conditions [65]. It has been used in electrical machine analysis since the 1970's [66][67]. The solution of the finite element problem is obtained by finding an approximate solution to the studied field quantity that lives in the same space as the basis functions. The basis functions are functions that have the value one in their node, and zero in all other nodes. The nodes are obtained from a mesh, often with triangular elements.

5.3 Electromagnetic force calculation by 2D finite element method

Motor Static and Dynamic UMPs can be calculated using 2D finite element method (FEM). Using 2D FEM, the following assumptions are made:

1) The motor rotor and stator core in the axial direction is uniform.
2) The fillet and chamfer of the stator core and rotor core will be ignored.
3) The end effect of the magnetic field will be ignored.
4) The magnetic field of the motor stator core's outer surface is zero.
5) The eddy current effect in the stator core will be ignored.

The magnetic vector potential can be calculated by:

$$\nabla\times[\frac{1}{\mu_r\mu_0}\nabla\times A_z(x,y)]=-J_z(x,y), \tag{5.2}$$

where $J_Z(x, y)$ is the section current density.

The magnetic density and magnetic flux density can then be calculated respectively:

$$B = \nabla \times A \quad , \tag{5.3}$$

$$H = B/(\mu_r \mu_0) \quad . \tag{5.4}$$

Finally, the Static and Dynamic UMPs of the rotor can be calculated by the virtual displacement method:

$$F_{ump} = \frac{\partial}{\partial s}[\int_V (\int_0^H BdH)dV] \quad . \tag{5.5}$$

where s is the displacement in the force direction, and V is the volume of the rotor.

5.3.1. Static Unbalanced Magnetic Pull

When the center of the motor's rotor is offset from its stator center but the center does not rotate around the stator center, the motor is defined as a Static Eccentricity (SE) faulty motor.

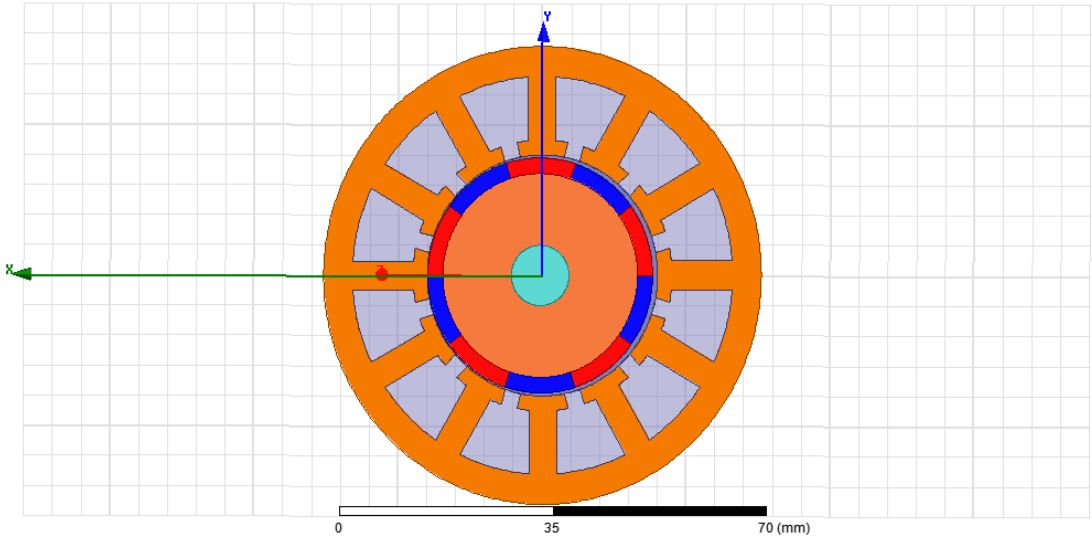

Figure 5.1: Geometry of 12S5PP SUMP motor

In the SE faulty motor, the Static Unbalanced Magnetic Pull (SUMP) is generated when the motor is running. The motor used in the study is a surface mounted Permanent Magnet Synchronous Motor (PMSM) with 12 slots and 5 pole-pairs (12S5PP), and its speed is 3000 RPM. Figure 5.1 shows the motor structure to be analyzed. It can be observed that the rotor's initial position is collinear in the x axis.

The element size of the air-gap is designed to be 0.05mm because the minimum air-gap is only 0.1 mm. The FEM model is shown in Figure 5.2.

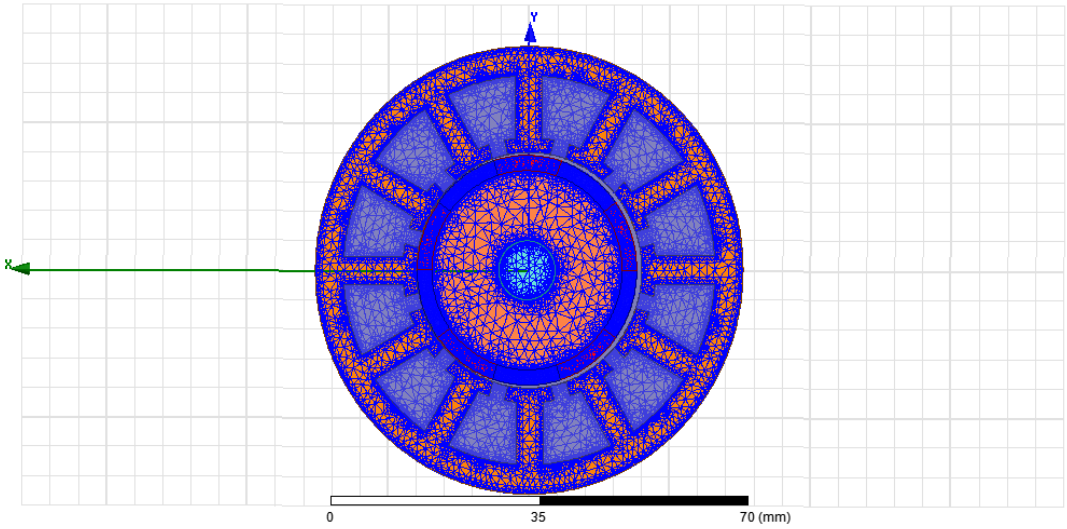

Figure 5.2: FEM model of 12S5PP SUMP motor

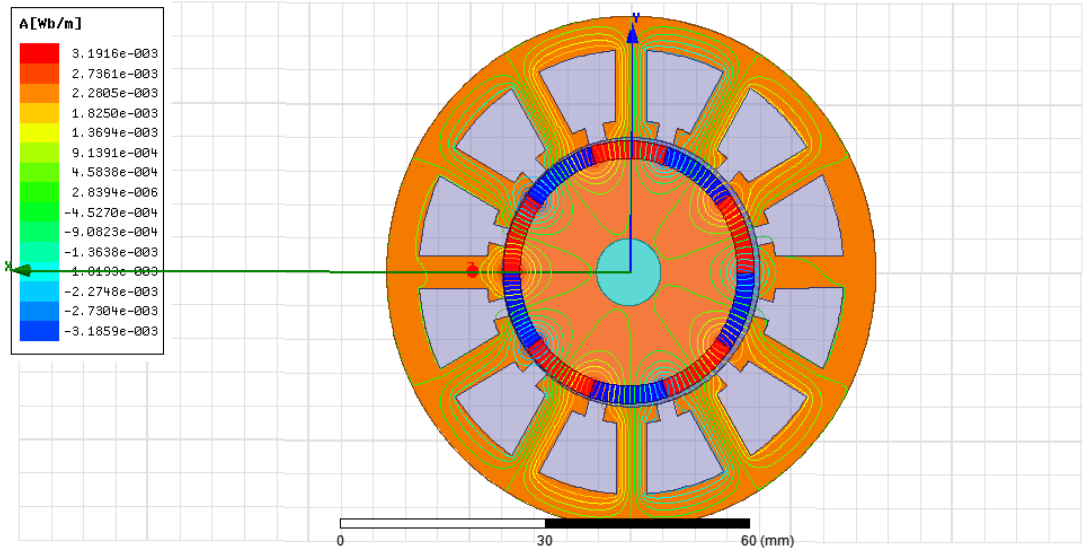

Figure 5.3: Flux lines of 12S5PP SUMP motor

The simulation results of the flux lines and magnetic flux density of the SUMP motor are shown in Figures 5.3 and 5.4.

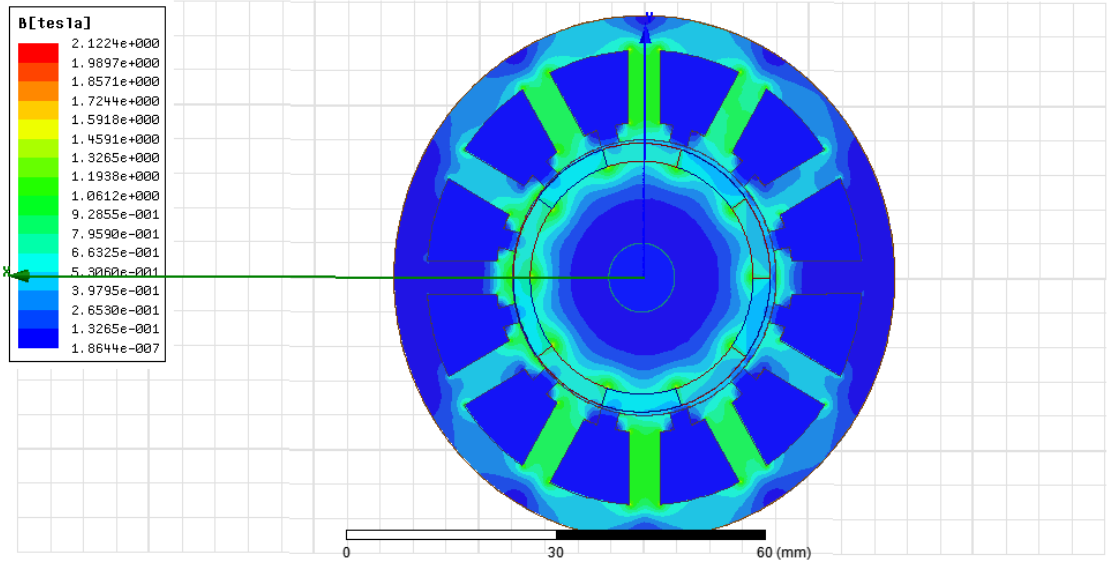

Figure 5.4: Magnetic Flux Density of 12S5PP SUMP motor

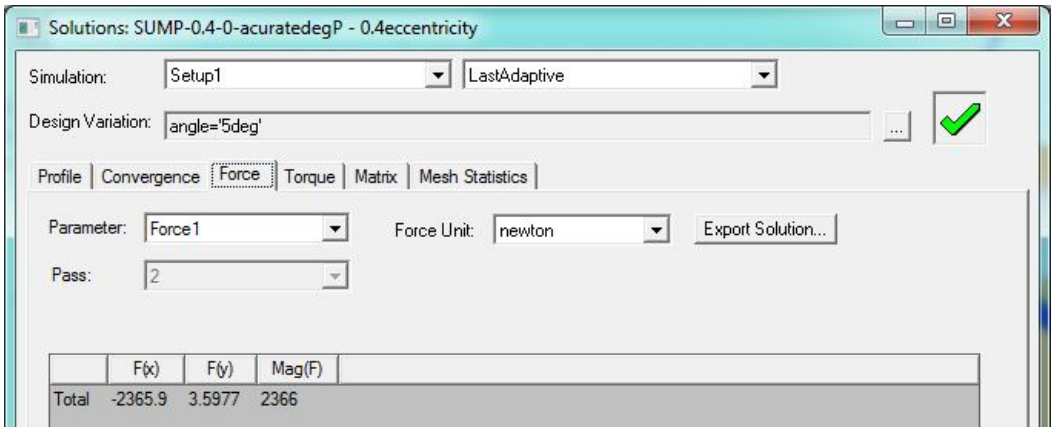

Figure 5.5: SUMP with default length setting in ANSOFT® in x and y direction on stator

The default length of the motor used in analysis is 1000 mm when the Maxwell2D static magnetic field solver is used, but the stator core length of the motor used in this study is only 13mm. If the assumption is that the SUMP force in the axial direction is evenly distributed, the SUMP can be obtained by:

$$F_{sump\_x} = \frac{F(x)\times 13}{1000}(Newton), \quad F_{sump\_y} = \frac{F(y)\times 13}{1000}(Newton) \quad , \tag{5.6}$$

where $F(x)$ and $F(y)$ are SUMP calculated by Maxwell2D solver as shown in Figure 5.5.

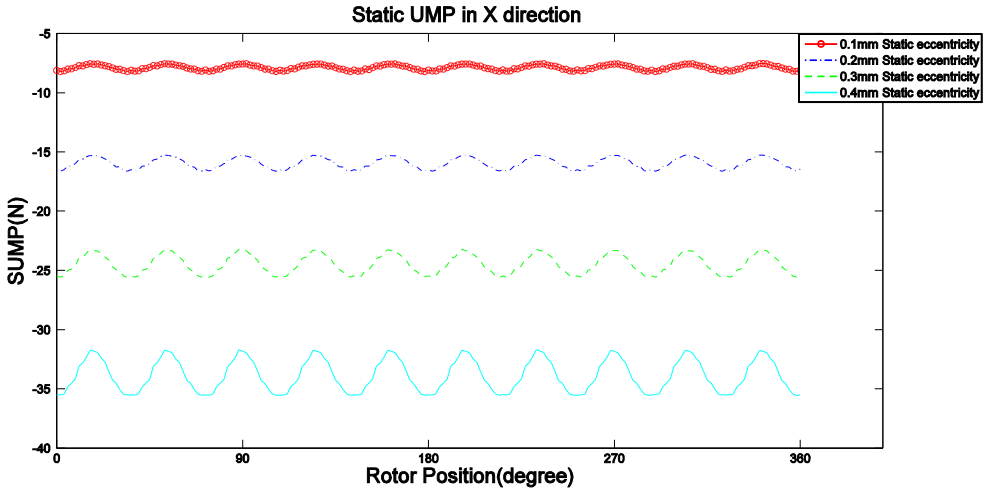

Figure 5.6: SUMP of 12S5PP motor in x direction with different static eccentricity

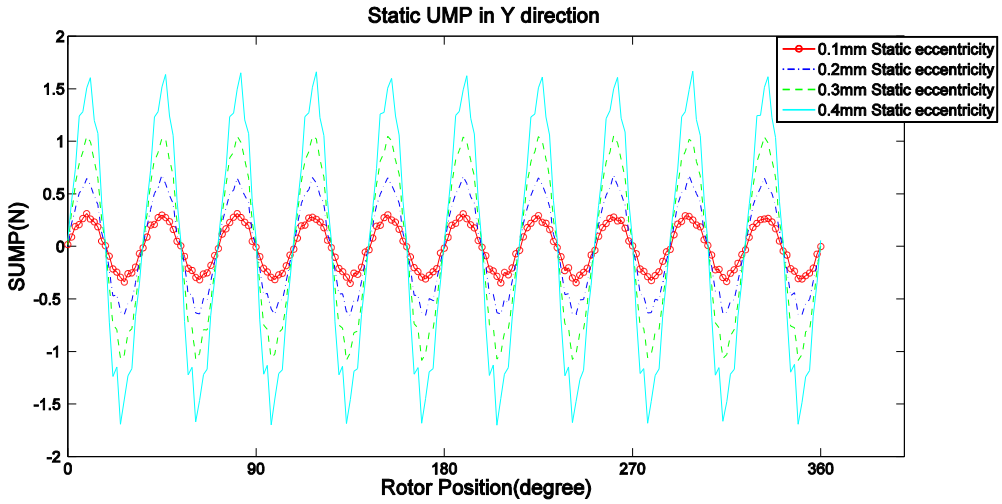

Figure 5.7: SUMP of 12S5PP motor in y direction with different static eccentricity

The rotor positions from 0 to 360 degrees with 2000 steps are calculated, and the SUMP is obtained in one full cycle. Then, the SUMP on the stator of the motor in the x and y directions are obtained and shown in Figures 5.6 and 5.7. It can be observed

that the SUMP in the x and y directions are repeated 10 times during one mechanical cycle. To better understand the faulty frequency of SUMP, Fourier transform (FT) is employed to convert time domain signal to frequency domain signal as shown in Figures 5.8 and 5.9.

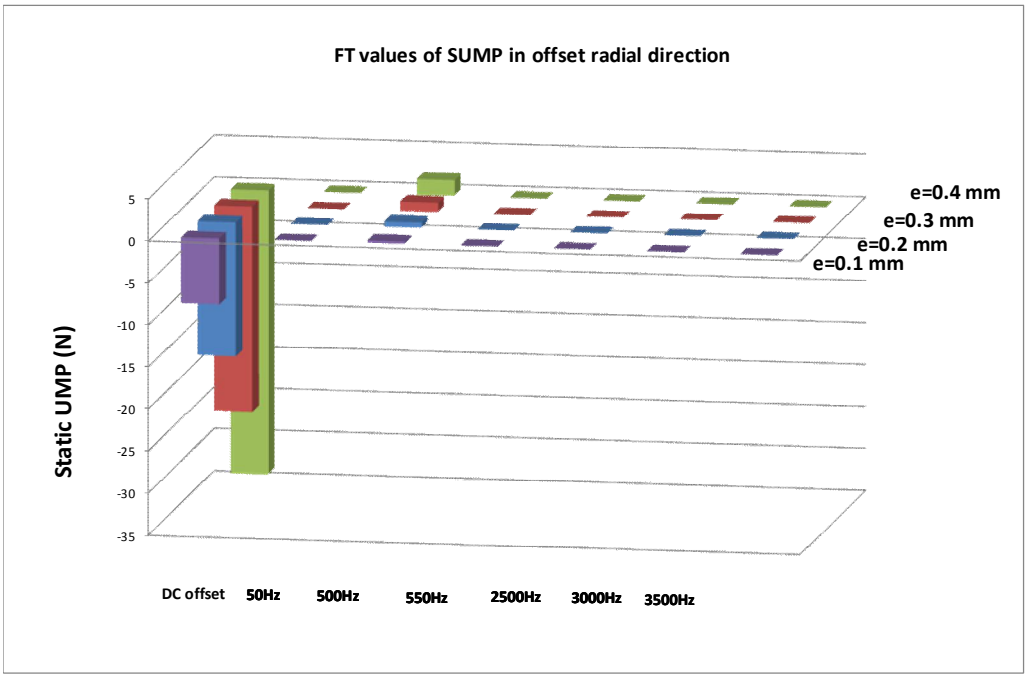

Figure 5.8: All main components of SUMP in offset direction

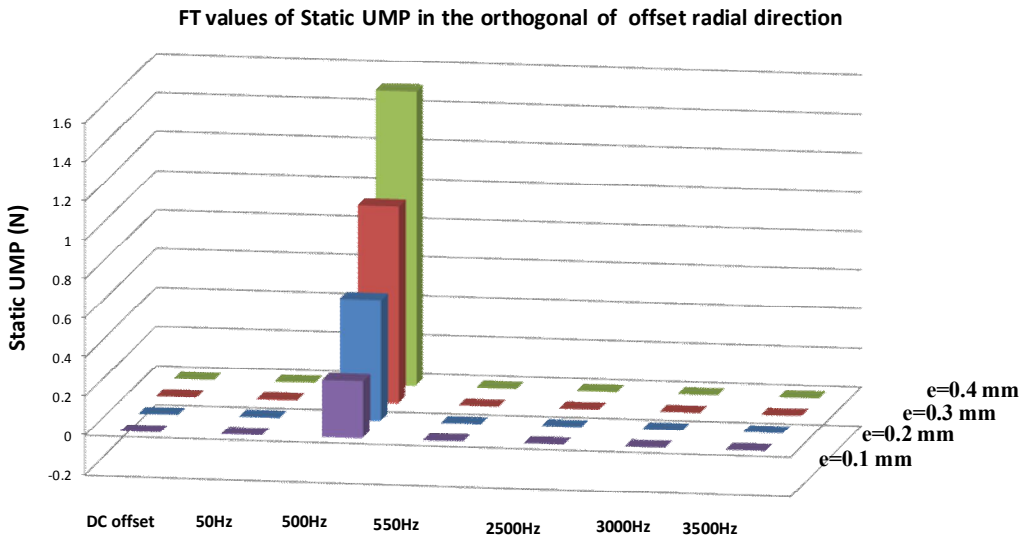

Figure 5.9: All main components of SUMP in the orthogonal of the offset direction

Figure 5.8 shows all main components of the SUMP in the offset direction. It can be observed that the DC and 500 Hz components are the dominant ones in the SUMP, these two components will be considered as the only excitation forces in future vibration analyses. Figure 5.9 shows all main components of the SUMP in the orthogonal of the offset direction. It can be observed that the 500 Hz components are dominant in the SUMP and they are considered as the only excitation forces in future vibration analyses.

The detailed values of the components of the SUMP in the offset direction are listed in Table 5.1. It can be observed that the DC and 500 Hz components are dominant in the SUMP, and in proportion to the eccentricity distance in the offset direction. The values of other orders components are as small as negligible (Figure 5.8).

Table 5.1: FT main components of SUMP in offset direction with different grades of SE faults calculated with FEM

Frequency(Hz)	e=0.1mm	e=0.2mm	e=0.3mm	e=0.4mm
0	**-7.877536675**	**-15.95476109**	**-24.48902901**	**-33.86621662**
50	0.001545449	0.005399179	0.002530073	0.004468707
500	**0.295566014**	**0.654664929**	**1.136767088**	**1.893571642**
550	0.004264765	0.004700421	0.001218807	0.005270306
2500	0.001111411	0.002433344	0.004397277	0.005625359
3000	0.000789972	0.001596159	0.002445844	0.0033731
3500	0.000763498	0.001556423	0.00240158	0.00335682

Table 5.2: FT main components of SUMP in orthogonal of offset direction with different grades of SE faults calculated with FEM

Frequency(Hz)	e=0.1mm	e=0.2mm	e=0.3mm	e=0.4mm
0	-0.00010388	0.000205293	0.000233276	-0.00014827
50	0.002432002	0.002081906	0.002582144	0.002176182
500	**0.295470447**	**0.619977895**	**1.011739246**	**1.51051141**
550	0.000952787	0.000639325	8.1579E-05	0.001916389
2500	0.000238854	0.000467963	0.00081579	0.002141106
3000	2.61261E-05	6.34861E-05	0.000118703	0.000195558
3500	2.70594E-05	5.99691E-05	9.7262E-05	0.000142147

The detailed values of the components of the SUMP in the orthogonal of the offset direction are listed in Table 5.2. It can be observed that the DC component of the SUMP is very small and near to zero. The value of the fundamental components (500 Hz) is proportional to the eccentricity distance in the orthogonal of the offset direction. Moreover, the amplitude of the value is the same as that in the offset direction.

When the PMSM has 5 pole-pairs and 12 slots, the equations (4.20) and (4.21) in Chapter 4 satisfied "$2np=mZ-2$" condition. These two equations can be simplified as,

$$P_{AE\_X}(\alpha,\delta) = -\frac{\varepsilon R_A \pi}{2\mu_0} \times \sum_m f_{A2n} l_{Am} \cdot \cos[2np\alpha + (\alpha - \delta)] \quad , \tag{5.7}$$

and

$$P_{AE\_X}(\alpha,\delta) = -\frac{\varepsilon R_A \pi}{2\mu_0} \times \sum_m f_{A2n} l_{Am} \cdot \sin[2np\alpha + (\alpha - \delta)] \quad . \tag{5.8}$$

When the eccentricity direction is in the x direction in equations (5.7) and (5.8), $\alpha - \delta$ is zero. If the speed of is 3000 RPM, α is 50 Hz. Therefore, the dominant component in SUMP is 500 Hz. Consequently, the simulation results validate that the analytical SUMP models shown in equations (4.20) and (4.21) are correct.

Table 5.3: Comparison between analytical solutions and simulation results (*x* direction)

Frequencies	DC	50 Hz	500 Hz	550 Hz	2500 Hz	3000 Hz	3500 Hz
Analytical results	**Yes**	NO	**Yes**	NO	Yes	NO	Yes
Simulation results	**Yes**	Yes (negligible)	**Yes**	Yes (negligible)	Yes	Yes (negligible)	Yes

Table 5.4: Comparison between analytical solutions and simulation results (y direction)

Frequencies	DC	50 Hz	500 Hz	550 Hz	2500 Hz	3000 Hz	3500 Hz
Analytical results	No	NO	**Yes**	NO	Yes	NO	Yes
Simulation results	Yes (negligible)	Yes (negligible)	**Yes**	Yes (negligible)	Yes	Yes (negligible)	Yes

In Chapter 4, the analytical model of the SUMP was presented. This model can also be used to analyze the motor shown in Figure 5.1. Tables 5.3 and 5.4 compare the SUMP obtained from the analytical model to its numerical results. From the tables, these two types of results are relatively matched though negligible results are seen in the simulation. These minor anomalies would be due to the computational error. The comparison show the effective of the analytical mode developed in Chapter 4.

5.3.2. Dynamic Unbalanced Magnetic Pull

When the center of the motor's rotor is offset from its stator center and the center also rotates around the stator center, the Dynamic Unbalanced Magnetic Pull (DUMP) is generated. The dynamic eccentricity could be caused by an ellipse of the rotor yoke, a bent rotor axis, and/or an uneven magnetic arrangement. In this analysis, the model of a no-eccentricity motor is built in an ANSOFT® model environment first, following which the rotor shaft, motor yoke, and all magnets are moved from the centre of the stator to the offset position. The full cycle DUMP with 2000 steps are calculated. Figure 5.10 shows the DUMP in the x direction with different dynamic eccentricities; the DUMP increases as the Dynamic Eccentricity (DE) increases. However, the relationship between the DUMP and the DE is not linear. The DUMP carries two frequency signals, a $1\times$ fundamental frequency and a $11\times$ pole-pair relative frequency. Moreover, the $11\times$ pole-pair relative frequency DUMP is also increased when the level of DE is increased. Figure 5.11 shows the DUMP in the $\boldsymbol{y}$ direction

with different dynamic eccentricities. The same conclusions can be drawn in Figures 5.10 and 5.11. The only difference is that there is a 90-degree phase shift from DUMP signals in Figure 5.10.

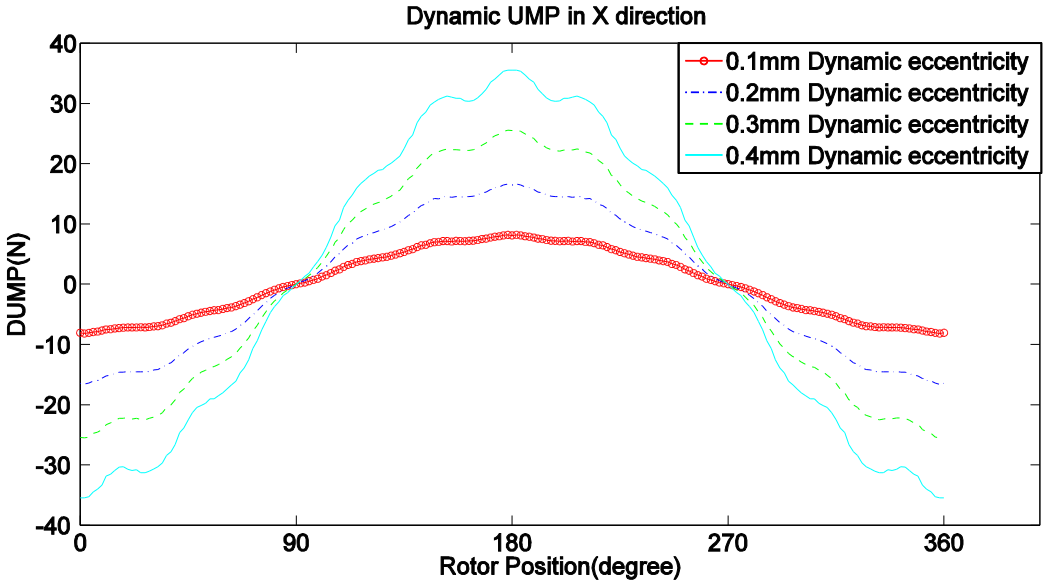

Figure 5.10: DUMP of 12S5PP motor in x direction with different dynamic eccentricities

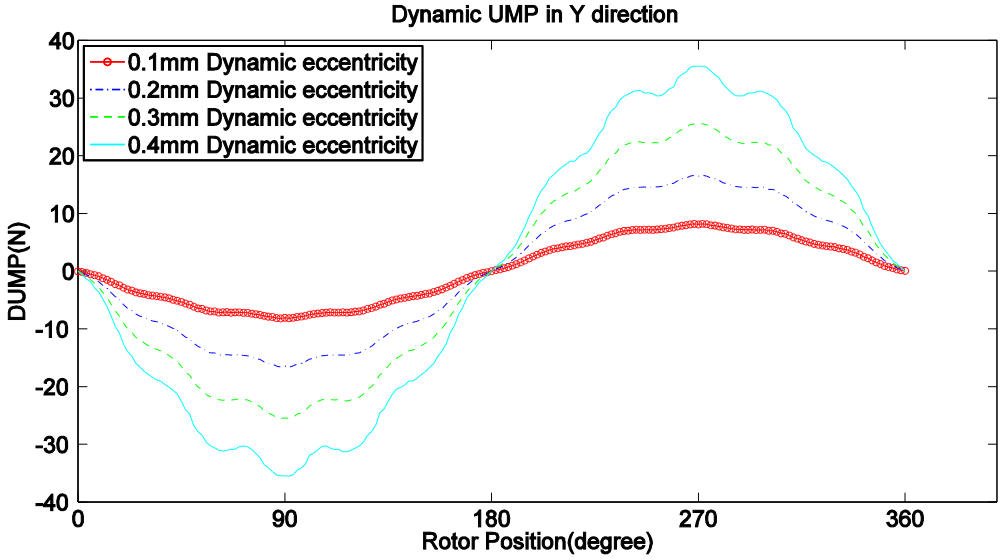

Figure 5.11: DUMP of 12S5PP motor in y direction with different dynamic eccentricities

To better understand the faulty frequency of DUMP, Fourier transform (FT) is employed to convert time domain signal to frequency domain signal as shown in Figure 5.12 and Figure 5.13.

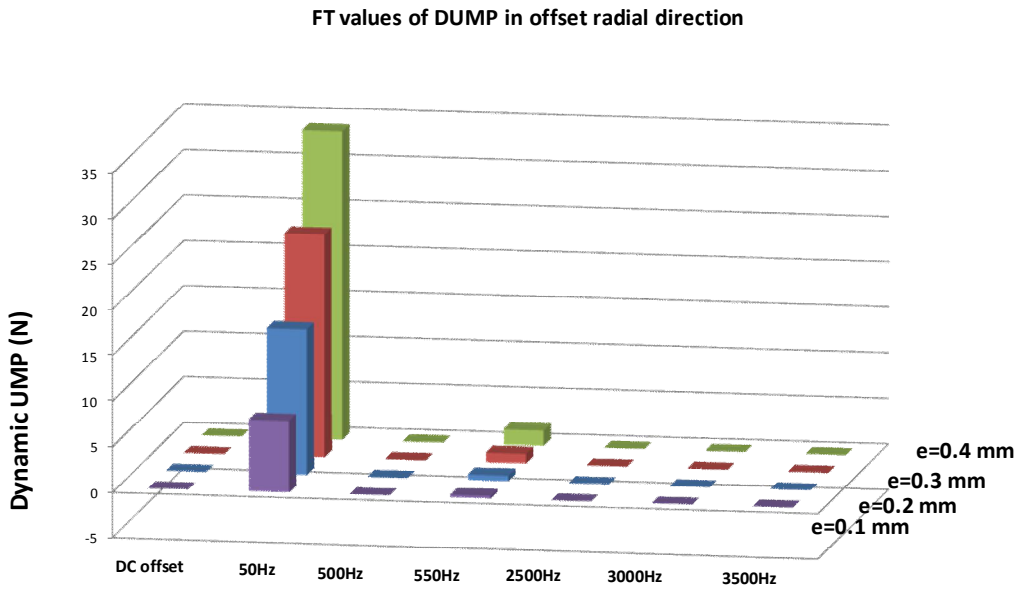

Figure 5.12: All main components of DUMP in the offset direction

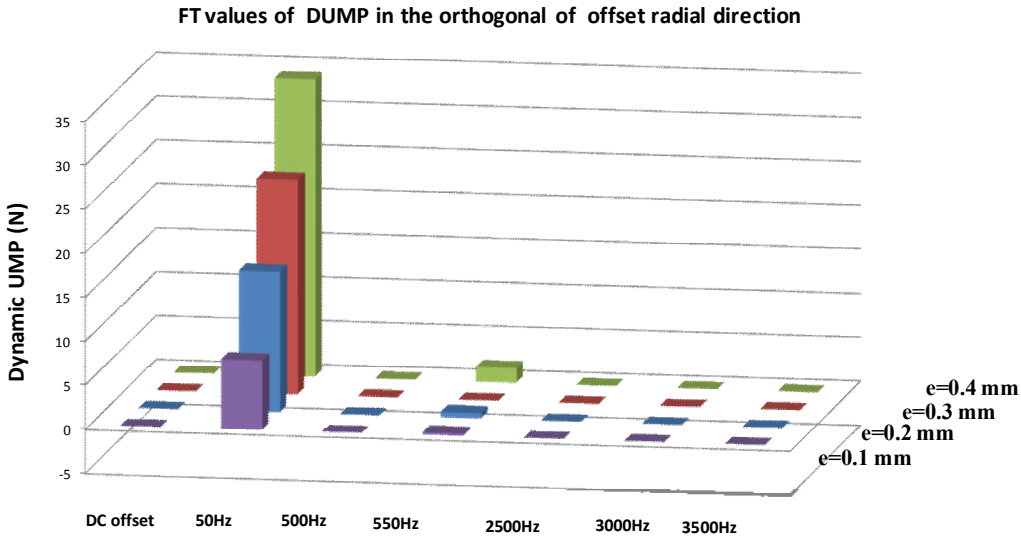

Figure 5.13: All main components of DUMP in the orthogonal of the offset direction

From Figure 5.12, it can be observed that the 50 Hz component is dominant in the DUMP. The second biggest contributor is the 550 Hz component, which has the pole number of the rotating revolutions in addition to one rotating revolution. Figure

5.13 shows all the main components of the DUMP in the orthogonal of the offset radial direction. It can be observed that the 50 Hz component is dominant in the DUMP, while the next biggest contributor is the 550 HZ component, which has the pole number of rotating revolutions in addition to one rotating revolution. It validates that the analytical DUMP model shown in equations (4.27) and (4.28) is correct. The procedure is shown as follows.

When the PMSM has 5 pole-pairs and 12 slots, the equations (4.27) and (4.28) in Chapter 4 satisfied "$2np=mZ-2$" condition. These two equations can be simplified as,

$$P_{AE\_X}(\alpha,\beta)=-\frac{\varepsilon R_A\pi}{2\mu_0}\times\sum_m f_{A2n}l_{Am}\cdot\cos[(2np+1)(\omega t+\alpha)] \quad , \tag{5.9}$$

and

$$P_{AE\_Y}(\alpha,\beta)=-\frac{\varepsilon R_A\pi}{2\mu_0}\times\sum_m f_{A2n}l_{Am}\cdot\sin[(2np+1)(\omega t+\alpha)] \quad . \tag{5.10}$$

When the speed of motor is 3000 RPM, the synchronous frequency is 500 Hz, from equations (5.9) and (5.10), it can been seen that the first two dominant components in DUMP are 50 Hz and 550 Hz.

The detailed values of the components of the DUMP in the offset direction are listed in Table 5.5. It can be observed that the 50Hz and 550 Hz components are dominant in the DUMP, and they are in proportion to the eccentricity distance in the offset direction. The values of other orders components are as small as negligible. Table 5.6 shows two main components of the DUMP in the orthogonal of offset direction, and it can be observed that the 50Hz and 550 Hz components are dominant in the DUMP, and they are in proportion to the eccentricity distance in the orthogonal

of offset direction. The values of other orders components are as small as negligible. The same result is also shown in Figure 5.12.

Table 5.5: FT main components of DUMP in offset direction with different grades of DE faults calculated with FEM

Frequency(Hz)	e=0.1mm	e=0.2mm	e=0.3mm	e=0.4mm
0	-0.008241551	-0.003503433	0.004196684	0.004996841
50	**7.865853985**	**15.94641568**	**24.4952554**	**33.86298869**
500	0.010563516	0.014420999	0.024067923	0.037254054
550	**0.297196429**	**0.634777401**	**1.071662399**	**1.70173481**
2500	0.001333763	0.001459486	0.002212539	0.004500623
3000	0.000718951	0.001456814	0.002246999	0.003124418
3500	0.000720668	0.001462247	0.002248747	0.003125665

Table 5.6: FT main components of DUMP in the orthogonal of offset direction with different grades of DE faults calculated with FEM

Frequency(Hz)	e=0.1mm	e=0.2mm	e=0.3mm	e=0.4mm
0	-4.408E-06	-0.000459605	-4.8047E-05	-7.7952E-05
50	**7.87670974**	**15.9613192**	**24.501069**	**33.865954**
500	0.00454842	0.019718091	0.028895784	0.042622988
550	**0.29559768**	**0.62869964**	**0.0015843**	**1.6993632**
2500	0.000237819	0.000506769	0.01584299	0.001738368
3000	0.000373966	0.000763904	0.001179234	0.001639747
3500	0.000373938	0.000758456	0.001173279	0.001630771

Tables 5.7 and 5.8 compare the theoretical prediction of DUMP from the analytical model in previous chapter with the numerical results from FEA simulation in this chapter in x and y direction. These two types of results are relatively matched though negligible results are seen in the simulation. These minor anomalies would be due to the computational error.

Table 5.7: Comparison between analytical solutions and simulation results (x direction)

Frequencies	DC	50 Hz	500 Hz	550 Hz	2500 Hz	3000 Hz	3500 Hz
Analytical results	NO	**Yes**	NO	**Yes**	NO	NO	NO
Simulation results	Yes (negligible)	**Yes**	Yes (negligible)	**Yes**	Yes (negligible)	Yes (negligible)	Yes (negligible)

Table 5.8: Comparison between analytical solutions and simulation results (y direction)

Frequencies	DC	50 Hz	500 Hz	550 Hz	2500 Hz	3000 Hz	3500 Hz
Analytical results	NO	**Yes**	NO	**Yes**	NO	NO	NO
Simulation results	Yes (negligible)	**Yes**	Yes (negligible)	**Yes**	Yes (negligible)	Yes (negligible)	Yes (negligible)

5.4 Electromagnetic force calculation by 3D finite element method

The Motor Inclined Unbalanced Magnetic Pull (IUMP) and Axial Unbalance Magnetic Pull (AUMP) are asymmetric in the axial direction. Therefore, only the three-dimensional FEM can be used to calculate IUMP and AUMP.

Using three-dimensional FEM, the following assumptions are made:

1) The motor rotor and stator core in the axial direction is uneven.
2) The fillet and chamfer of the stator core and rotor core are ignored.
3) The end effect of the magnetic field is ignored.
4) The motor is surrounded by a region whose magnetic field is zero.
5) The eddy current effect in the stator core is ignored.

The magnetic vector potential can be calculated by:

$$J(x,y,z) = \nabla \times H(x,y,z) \quad , \tag{5.11}$$

$$\nabla \cdot B(x,y,z) = 0 \quad , \tag{5.12}$$

where $J(x, y, z)$ is the current density and $B(x, y, z)$ is the magnetic density.

For a permanent magnet, the magnetic density can be described as:

$$B = \mu_0 \cdot \mu_r \cdot H + \mu_0 \cdot M_p \quad , \tag{5.13}$$

where μ_0 is the vacuum permeability, μ_r the relative permeability of the permanent magnet, and M_p the magnetic polarization intensity of the permanent magnet material.

If the rotor core and/or stator core are/is made by anisotropy, the tensor form of the relative permeability can be described as:

$$\mu_r = \begin{bmatrix} \mu_{rx} & & \\ & \mu_{ry} & \\ & & \mu_{rz} \end{bmatrix} . \tag{5.14}$$

The magnetic flux density can be described as:

$$H = H_p + \nabla \cdot \varphi + H_c . \tag{5.15}$$

where φ is scalar magnetic potential, H_p the magnet density of each tetrahedral element, and M_c the magnet density on the permanent magnet.

5.4.1. Inclined Unbalanced Magnetic Pull

When both sides of the rotor center are offset from the stator center with different levels and/or different directions without the rotor center rotating around the stator center, the motor is called an Inclined Eccentricity (IE) faulty motor. In the IE motor, the Inclined Unbalanced Magnetic Pull (IUMP) will be generated. The Inclined Eccentricity (IE) could be caused by a misplacement of the rotor onto the stator, the location parts with lower machining tolerances, or the rotor being shifted down due to the wearing out of the bearings. The eccentricity ratio and/or the direction of eccentricity are/is different in each section of the axis direction, and therefore the IUMP should be different in each section and the position of the IUMP center may vary. In order to calculate the IUMP correctly, the stator is divided into multi-segments in the axial direction. In the radial direction, each section is divided into multi-sections.

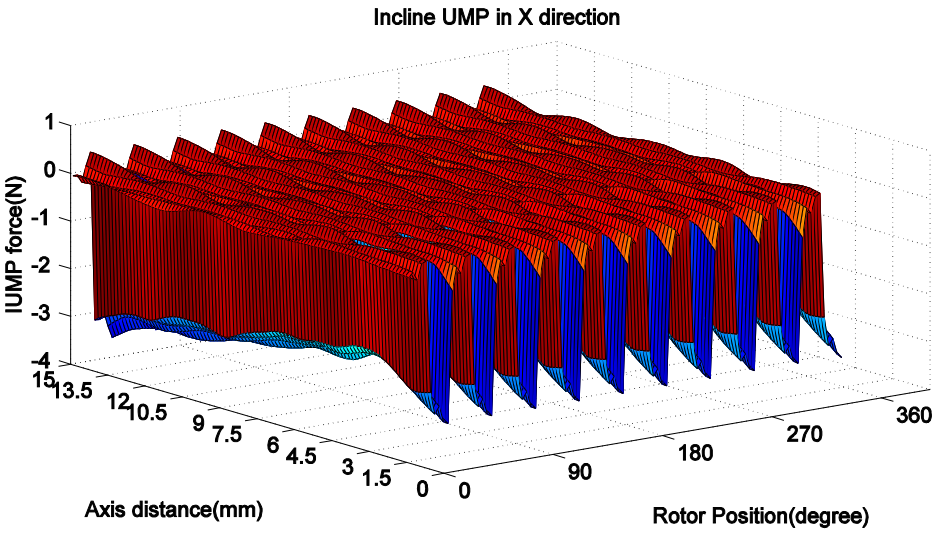

Figure 5.14: 3D view of IUMP force in x direction in each section

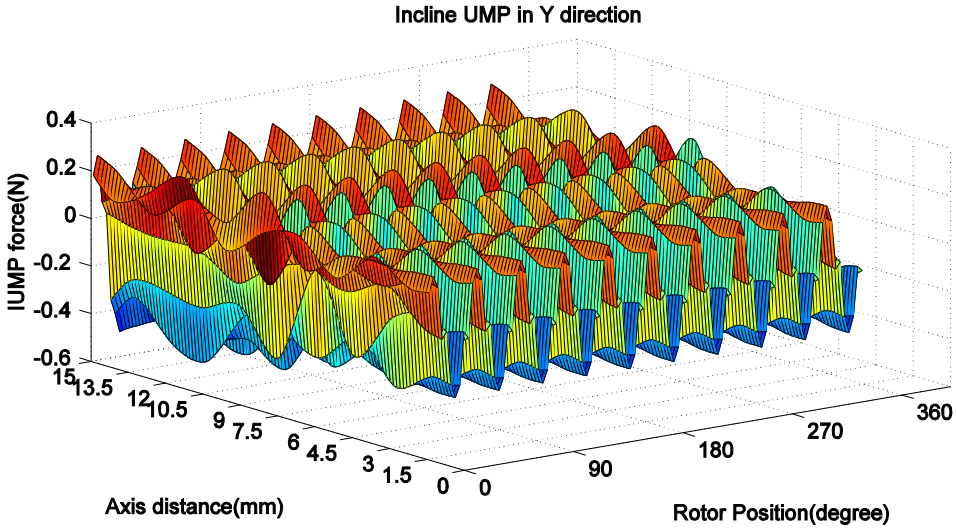

Figure 5.15: 3D view of IUMP force in y direction in each section

Figure 5.14 shows that the IUMP not only repeats 10 times in one full rotor cycle, but also has DC offset in the eccentricity direction. The reason is that the IE is also a type of static rotor eccentricity and the studied motor structure has 10 poles and 12 slots structure. In Figure 5.15, although there is no IE in the y direction, the IUMP in the y direction still exists, and its frequency is also 10 times of the rotor's rotating frequency. However, the amplitudes of the IUMP in the y direction are much smaller

than the IUMP in the x direction, which are shown in Figure 5.14. Figure 5.15 also shows that the IUMP in the y direction does not have any DC offset.

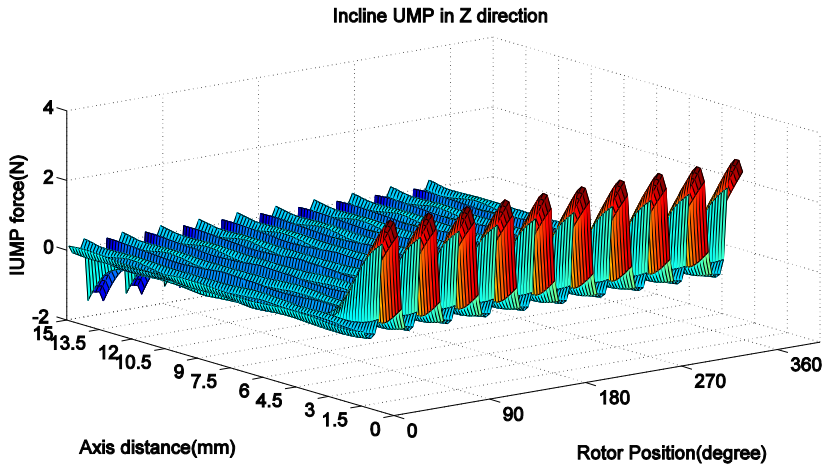

Figure 5.16: 3D view of IUMP force in z direction in each section

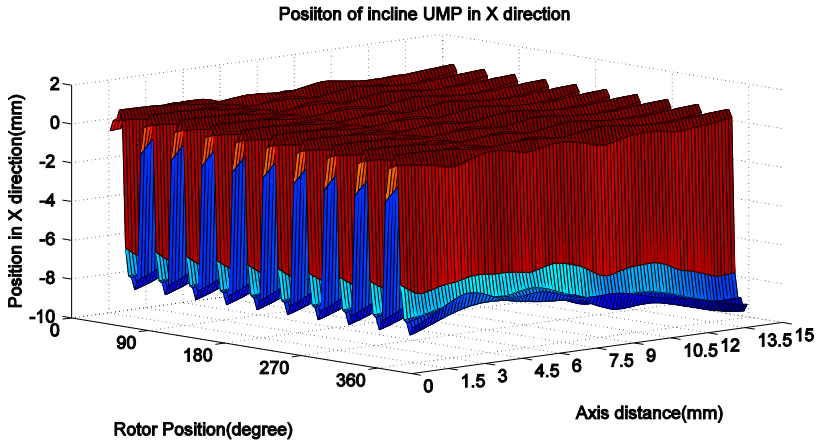

Figure 5.17: Varied position of IUMP in x direction

In Figure 5.16, the frequency of the IUMP is 10 times of the rotor's rotating speed. The reason is that the studied motor structure has 10 poles and 12 slots structure. The diagram also shows that the IUMP force at the both ends of the stator in the z direction is larger than that of the middle section of the stator. This is the angular

effect of the misalignment of the axis end point. The phenomenon can be utilized to effectively distinguish motor misalignment faults from static eccentricity faults.

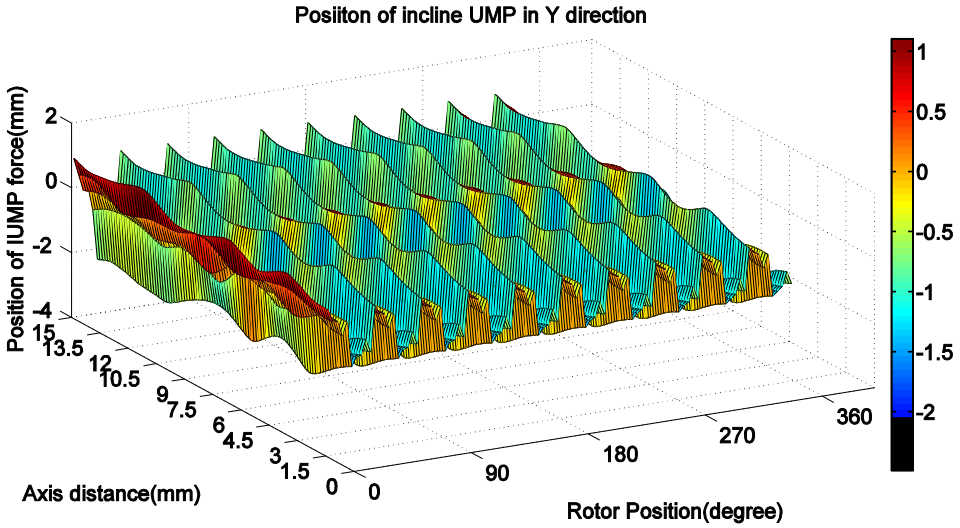

Figure 5.18: Varied position of IUMP in y direction

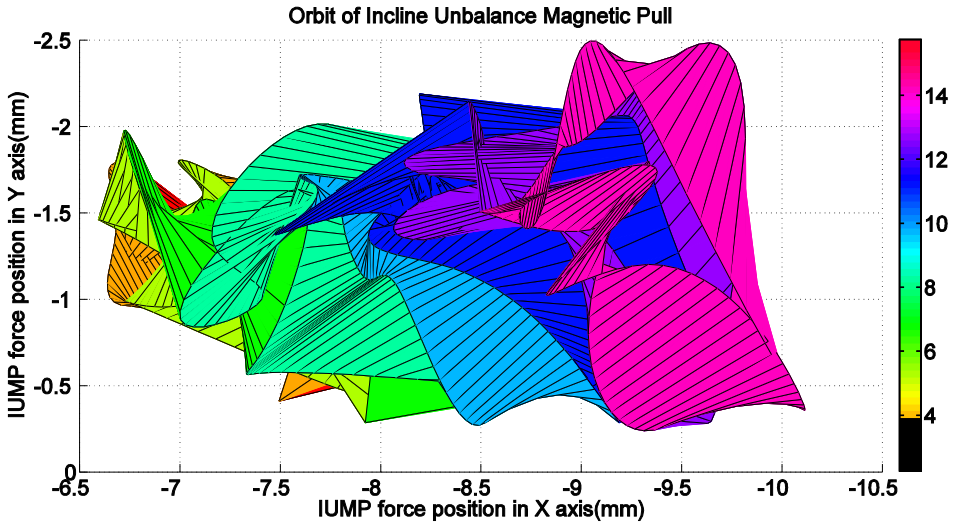

Figure 5.19: The variation of UMP center of 12S5PP motor obtained with FEM in Cartesian coordinates

In Figures 5.17 and 5.18, it can be seen that the IUMP force acting position, as well as the direction and amplitude of the IUMP force, change by time in different portions of the motor stator section due to different eccentricity grades in different

section of the motor along axis. This phenomenon will cause additional motor vibration and acoustic noise that reduce the motor's life cycle.

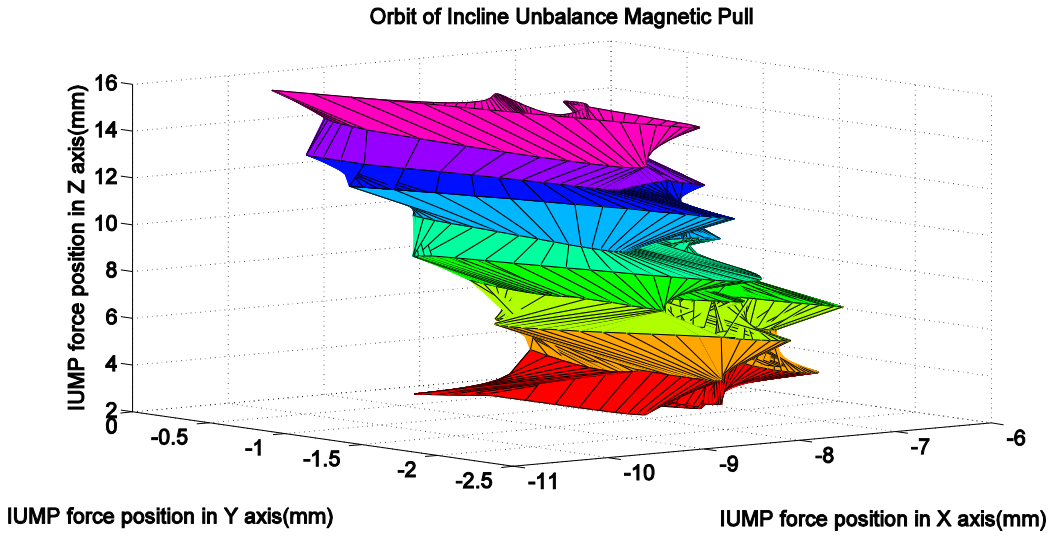

Figure 5.20: The variation of UMP center of 12S5PP motor obtained with FEM in three-dimensional coordinates

Figures 5.19 and 5.20 show the positional orbit of the IUMP in 2D and 3D format in Cartesian coordinates (refer to Appendix A). The orbit center in each section is different due to a 0.3mm misalignment of the rotor in the x direction. It can be seen that the IUMP position has a large variation although the rotor only has a 0.3mm offset. This can increase the motor vibration and acoustic level if we do not consider it in the design and manufacturing stages. The motor's repeatable runout (RRO) and non-repeatable run out (NRRO) should be increased, causing the dynamic performance of the motor to be downgraded. To better understanding the faulty frequency of IUMP, Fourier transform (FT) is employed to convert time domain signal to frequency domain signal as shown in Figures 5.21, 5.22 and 5.23.

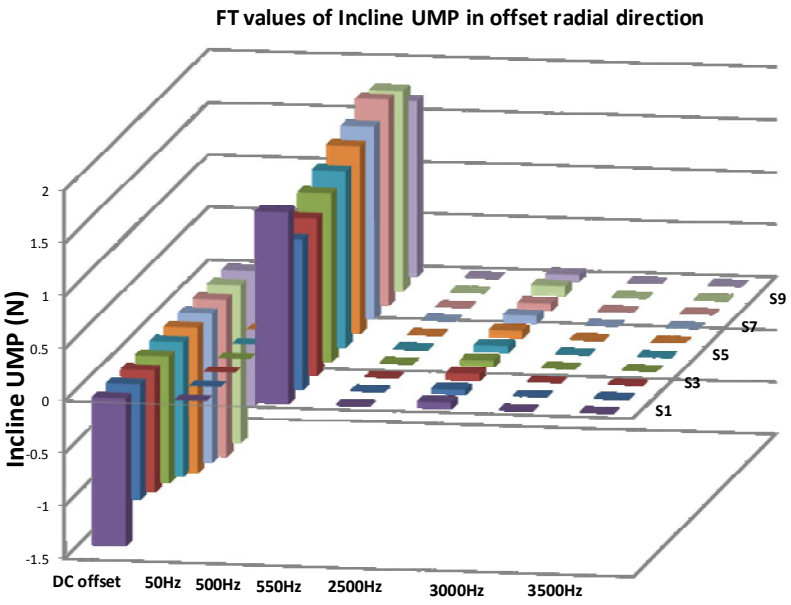

Figure 5.21: All main components of IUMP in the offset direction in 12S5PP motor with 0.3mm IE fault

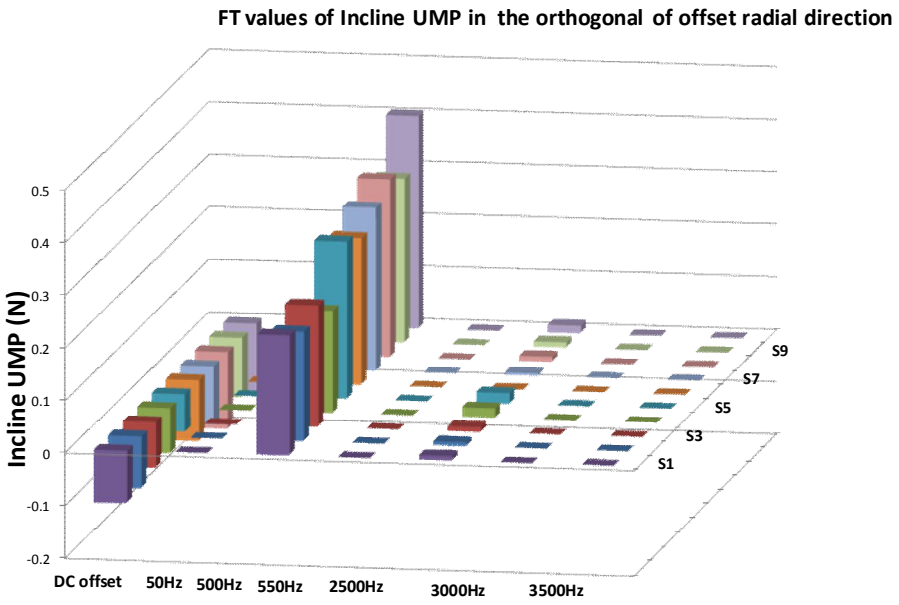

Figure 5.22: All main components of IUMP in the orthogonal of the offset direction in 12S5PP motor with 0.3mm IE fault

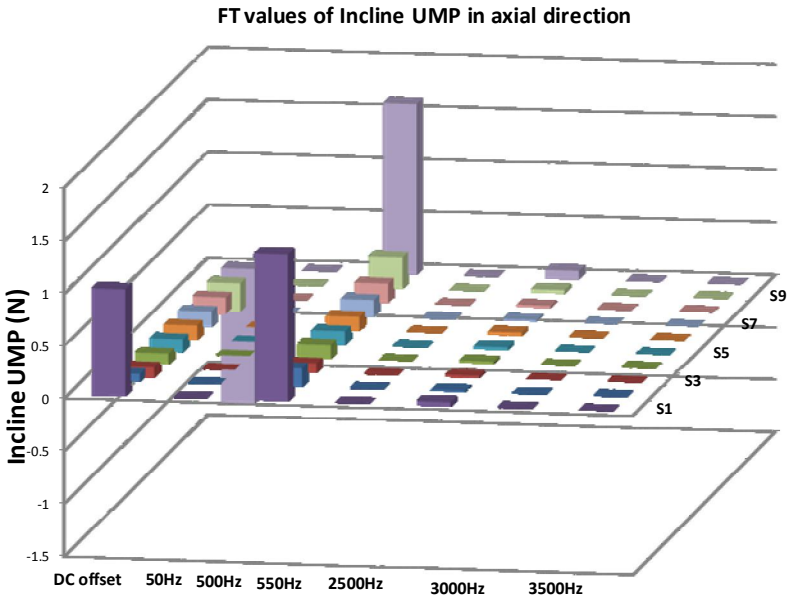

Figure 5.23: All main components of IUMP in axial direction in 12S5PP motor with 0.3mm IE fault

The detailed values of the components of the IUMP in 10 segments in x, y and z directions are listed in Tables 5.9, 5.10 and 5.11.

Table 5.9: FT main components of IUMP in the offset direction with 0.3 mm eccentricity of IE faults calculated with FEM

Frequency (Hz)	DC	50Hz	500Hz	550 Hz	2500Hz	3000 Hz	3500Hz
Segment 1	**-1.399228**	1.72E-06	**1.8107609**	1.62E-06	0.056672	7.191E-07	0.00013
Segment 2	**-1.091028**	2.68E-06	**1.4217924**	2.48E-06	0.042893	6.812E-07	0.000107
Segment 3	**-1.156632**	4.19E-06	**1.4840673**	3.89E-06	0.060188	1.19E-06	9.85E-05
Segment 4	**-1.208132**	1.16E-05	**1.5944342**	1.12E-05	0.055606	7.631E-06	9.27E-05
Segment 5	**-1.278182**	4.06E-06	**1.6679287**	3.56E-06	0.05793	3.561E-06	0.000105
Segment 6	**-1.375345**	3.15E-06	**1.779324**	2.55E-06	0.06536	2.548E-06	0.000114
Segment 7	**-1.412977**	7.14E-07	**1.8289355**	1.44E-08	0.075156	6.144E-07	0.000118
Segment 8	**-1.494201**	2.64E-06	**1.9509217**	1.84E-06	0.058705	1.839E-06	0.000145
Segment 9	**-1.498396**	6.78E-07	**1.9003392**	5.88E-07	0.08666	5.779E-07	0.00011
Segment 10	**-1.278182**	4.06E-06	**1.6679287**	3.06E-06	0.05793	3.061E-06	0.000105
Total	**-13.192**	**3.6E-05**	**17.1064**	**3.1E-05**	**0.6171**	**2.2E-05**	**0.00113**

The first column of Table 5.9 shows the DC components of the IUMP in the offset direction. It can be seen that the DC component of the IUMP is not evenly distributed throughout these 10 segments due to the three-dimensional magnetic field effect. The

third column of Table 5.9 shows the 500Hz components of the IUMP in the offset direction. It can be observed that the 500Hz components of IUMP in Segment 1~Segment 10 follow the same trend as those in the first column of Table 5.9. The IUMP is varied from Segments 1 to 10 because the air-gap is varied. Other components in Table 5.9 are as small as negligible compared to DC and 500 Hz components for motor vibration analyses in the following chapter.

Table 5.10: FT main components of IUMP in the orthogonal of the offset direction with 0.3mm eccentricity of IE faults calculated with FEM

Frequency (Hz)	DC	50Hz	500Hz	550 Hz	2500Hz	3000 Hz	3500Hz
Segment 1	**-0.100511**	1.36E-06	**0.2293099**	3.62E-07	0.008797	3.622E-07	2.83E-05
Segment 2	**-0.100009**	2.93E-06	**0.2092073**	9.3E-07	0.007714	9.3E-07	2.64E-05
Segment 3	**-0.086302**	1.18E-06	**0.2326343**	1.76E-07	0.009533	1.762E-07	1.88E-05
Segment 4	**-0.086474**	1.12E-06	**0.1953355**	1.19E-07	0.018662	1.188E-07	6.54E-06
Segment 5	**-0.071513**	4.11E-06	**0.2995234**	2.11E-06	0.020984	1.114E-06	2.22E-05
Segment 6	**-0.117012**	2.81E-06	**0.2796568**	3.12E-07	0.001096	1.812E-06	2.41E-05
Segment 7	**-0.111932**	3.94E-06	**0.310017**	1.94E-06	0.005	9.447E-07	2.41E-05
Segment 8	**-0.148075**	4.35E-07	**0.3378266**	1.35E-07	0.010142	4.351E-07	2.65E-05
Segment 9	**-0.114407**	5.33E-06	**0.3120779**	1.33E-06	0.010555	1.329E-06	2.82E-05
Segment 10	**-0.133224**	2.1E-06	**0.4048608**	2.1E-06	0.014993	9.554E-08	7.55E-06
Total	**-1.0695**	**2.5E-05**	**2.81045**	**9.5E-06**	**0.10748**	**7.3E-06**	**0.00021**

Table 5.10 shows the DC and 500Hz components of the IUMP in the orthogonal of the offset direction. Both components are much smaller than those in the offset direction in Table 5.9. It also shows that the biggest amplitude is that of the 500 Hz component, while the amplitudes of other components are as small as negligible compared with those of 500 Hz components.

Table 5.11 shows all the main components of the IUMP in the axial direction. The two large values of the DC offset component and the 500 Hz components are found in segments 1 and 10. This phenomenon may be caused by the angular effect of the misalignment of the axis end point in the IUMP condition. In the axial direction, other

order harmonic components are negligible and only DC and 500 Hz components are therefore considered as excitation forces in the vibration studies of IE faulty motor in the following chapter.

Table 5.11: FT main components of IUMP in the axial direction with 0.3mm eccentricity of IE faults calculated with FEM

Frequency (Hz)	DC	50Hz	500Hz	550 Hz	2500Hz	3000 Hz	3500Hz
Segment 1	1.016764	9.55E-06	1.3986441	9.65E-06	0.035839	8.653E-06	8.78E-05
Segment 2	0.07289	2.33E-06	0.1731078	2.63E-06	0.007316	1.526E-06	2.95E-05
Segment 3	-0.090749	7.43E-06	0.086301	7.73E-06	0.014192	6.734E-06	3.46E-05
Segment 4	-0.098056	7.31E-06	0.1291933	7.71E-06	0.015607	6.715E-06	3.6E-05
Segment 5	-0.116916	8.19E-06	0.1253041	8.69E-06	0.02077	7.686E-06	2.28E-05
Segment 6	-0.139584	8.45E-06	0.1310332	9.05E-06	0.024932	8.046E-06	3.32E-05
Segment 7	-0.146858	7.95E-06	0.1581827	8.65E-06	0.011669	7.354E-06	1.19E-05
Segment 8	-0.159625	7.39E-06	0.1786659	8.19E-06	0.015287	4.387E-06	4.8E-05
Segment 9	-0.275617	1.07E-05	0.2959474	1.16E-05	0.030433	7.729E-06	4.46E-05
Segment 10	-1.27982	5.93E-06	1.6103579	4.93E-06	0.076906	5.832E-06	0.00011
Total	**-1.2176**	**7.5E-05**	**4.28674**	**7.9E-05**	**0.25295**	**6.5E-05**	**0.00046**

Table 5.12 shows the components of the total IUMP of the ten segments with different grades of IE faults in the offset direction. It can be observed that the DC and 500 Hz components are two dominant ones in the IUMP, and in proportion to the eccentricity distance in the offset direction. The values of other order frequency components are as small as negligible.

Table 5.12: FT main components of IUMP in the offset direction with different grades of IE faults calculated with FEM

Frequency(Hz)	e=0.1mm	e=0.2mm	e=0.3mm	e=0.4mm
0	-4.3974345	-8.7948691	-13.1923036	-17.58974
50	1.1841E-05	2.36817E-05	3.55225E-05	4.7363E-05
500	5.702144	11.4042884	17.106433	22.80858
550	1.0278E-05	2.0555E-05	3.08325E-05	4.111E-05
2500	0.20570036	0.411400728	0.617101092	0.822801
3000	7.4742E-06	1.49484E-05	2.24225E-05	2.9897E-05
3500	0.00037501	0.000750017	0.001125025	0.00150003

Table 5.13 shows the components of the total IUMP of the ten segments with different grades of IE faults in the orthogonal of the offset direction. It can be seen that the DC component of the IUMP is very small compared to the offset direction. The value of the fundamental component (500 Hz) is proportional to the eccentricity distance in the orthogonal of the offset direction. The values of other orders components are as small as negligible.

Table 5.13: FT main components of IUMP in the orthogonal of the offset direction with different grades of IE faults calculated with FEM

Frequency(Hz)	e=0.1mm	e=0.2mm	e=0.3mm	e=0.4mm
0	2.40893E-05	2.40893E-05	**-1.069459**	**-1.4259454**
50	8.43896E-06	1.68779E-05	2.53169E-05	3.37558E-05
500	**0.9368166**	**1.8736332**	**2.8104497**	**3.7472663**
550	3.17229E-06	1.68779E-05	9.51688E-06	1.26892E-05
2500	0.035825537	0.071651074	**0.1074766**	**0.1433021**
3000	2.43896E-06	6.34458E-06	7.31688E-06	9.75584E-06
3500	7.08798E-05	0.071651074	0.000212639	0.000283519

Table 5.14 FT main components of IUMP in axial direction with different grades of IE faults calculated with FEM

Frequency(Hz)	e=0.1mm	e=0.2mm	e=0.3mm	e=0.4mm
0	2.2836E-05	3.3175E-05	**-1.2175708**	**-1.706427**
50	1.9773E-06	3.9546E-06	7.52628E-05	7.9092E-06
500	**0.536786**	**1.0735719**	**4.2867374**	**2.1471438**
550	1.644E-06	3.9546E-06	7.88628E-05	6.5759E-06
2500	0.02563533	1.07357191	0.252951292	0.1025413
3000	1.944E-06	3.2879E-06	6.4663E-05	7.7759E-06
3500	3.6586E-05	0.05127066	0.000458144	0.00014635

Table 5.14 shows that there is an additional 500 Hz faulty frequency component in simulation results due to the angular effect of the misalignment of the axis end point of IUMP. To simplify analytical calculation in Chapter 4, this end effect of IUMP is

ignored and the derived equations do not have any frequency component in axial direction.

Tables 5.15, 5.16 and 5.17 compare the theoretical prediction of IUMP from the analytical model in previous chapter with the numerical results from FEA simulation in this chapter in x, y and z directions respectively. These two types of results are relatively matched though negligible results are seen in the simulation. These minor anomalies would be due to the computational error. The results difference in z direction is caused by the angular effect of the misalignment of the axis end point in the simulation model.

Table 5.15: Comparison between analytical solutions and simulation results (x direction)

Frequencies	DC	50 Hz	500 Hz	550 Hz	2500 Hz	3000 Hz	3500 Hz
Analytical results	**Yes**	NO	**Yes**	NO	Yes	NO	Yes
Simulation results	**Yes**	Yes (negligible)	**Yes**	Yes (negligible)	Yes	Yes (negligible)	Yes

Table 5.16: Comparison between analytical solutions and simulation results (y direction)

Frequencies	DC	50 Hz	500 Hz	550 Hz	2500 Hz	3000 Hz	3500 Hz
Analytical results	No	NO	**Yes**	NO	Yes	NO	Yes
Simulation results	Yes (negligible)	Yes (negligible)	**Yes**	Yes (negligible)	Yes	Yes (negligible)	Yes

Table 5.17: Comparison between analytical solutions and simulation results (z direction)

Frequencies	DC	50 Hz	500 Hz	550 Hz	2500 Hz	3000 Hz	3500 Hz
Analytical results	No	NO	**No**	NO	NO	NO	NO
Simulation results	Yes	Yes (negligible)	**Yes**	Yes (negligible)	Yes	Yes (negligible)	Yes (negligible)

5.4.2. Axial Unbalanced Magnetic Pull

When the motor's rotor center is offset from its stator center in the axial direction, the Axial Unbalanced Magnetic Pull (AUMP) is generated.

Figure 5.24 shows the AUMP in the axial direction with different grades of Axial Eccentricity (AE) fault. It can be seen that the DC offset and the fundamental frequency increases with the eccentricity grade.

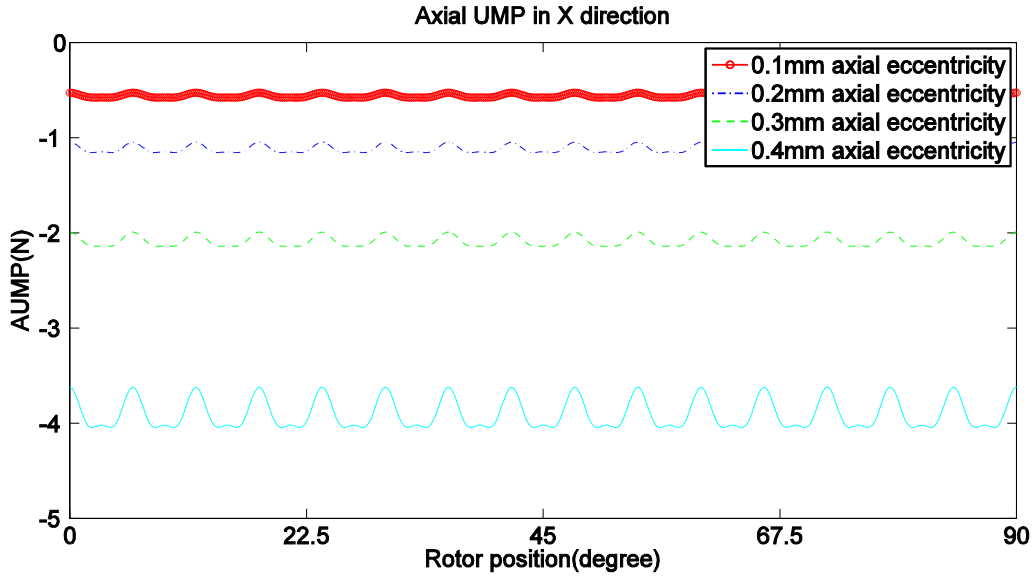

Figure 5.24: AUMP of 12S5PP motor in the axial direction with different axial eccentricity

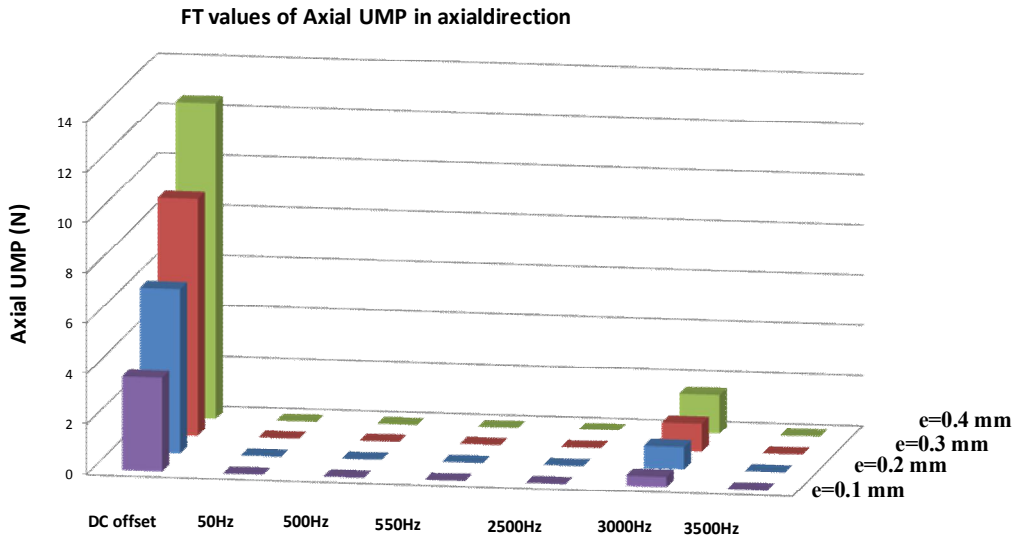

Figure 5.25: All main components of AUMP of 12S5PP motor in axial direction

Figure 5.25 shows each component of the AUMP in the axis direction. It can be observed that the DC and 3000 Hz are the largest components when they compared to the other harmonics of the components. The fundamental frequency is $60 \times$ order of the motor rotating frequency. Others can be ignored when motor vibration is simulated with FEM in the following chapter.

Table 5.18: FT main components of AUMP in the axial direction with different grades of AE faults calculated with FEM

Frequency(Hz)	e=0.1mm	e=0.2mm	e=0.3mm	e=0.4mm
0	**3.725125**	**6.556221**	**9.431234**	**12.565457**
50	3.20016E-05	8.19064E-05	8.21442E-05	0.000126182
500	7.04468E-05	7.89531E-06	9.24645E-06	1.14098E-05
550	2.78719E-06	9.32468E-06	4.1579E-05	0.000916389
2500	8.85424E-06	7.96277E-06	5.78967E-06	0.001901106
3000	**0.4125578**	**0.8752569**	**1.1246156**	**1.5618278**
3500	1.05941E-06	1.96907E-06	3.26198E-06	4.14665E-06

Table 5.18 shows the components of the AUMP in the axial direction. It can be observed that the DC and 3000 Hz components are dominant in the AUMP, and in proportion to the eccentricity distance in the offset direction. The values of other order components are negligible.

Table 5.19: Comparison between analytical solutions and simulation results

Frequencies	DC	50 Hz	500 Hz	550 Hz	2500 Hz	3000 Hz	3500 Hz
Analytical results	**Yes**	NO	NO	NO	NO	**Yes**	NO
Simulation results	**Yes**	Yes (negligible)	Yes (negligible)	Yes (negligible)	Yes (negligible)	**Yes**	Yes (negligible)

Table 5.19 compares the theoretical prediction of AUMP from the analytical model in the previous chapter with the numerical results from FEA simulation in this chapter. These two types of results are relatively matched though negligible results

are seen in the simulation. These minor anomalies would be due to the computational error.

5.5 Conclusions

In this chapter, Static Unbalanced Magnetic Pull (SUMP) and Dynamic Unbalanced Magnetic Pull (DUMP) are calculated by using 2D FEM. The Inclined Unbalanced Magnetic Pull (IUMP) and Axial Unbalanced Magnetic Pull (AUMP) are calculated by using 3D FEM.

Numerical results of SUMP validate Deduction 4.2.1 in Chapter 4 as follows: the SUMP has a constant force in the offset direction and has no any constant force in the orthogonal of the offset direction. Moreover, in one motor revolution, the lowest order of the SUMP harmonic is two times of its pole-pair number. On the contrary, numerical results of DUMP validate Deduction 4.2.2 in the previous chapter as follows: the DUMP does not have a constant force, but has a large varied force with rotor mechanical rotating speed. DUMP has 1 × and ($P+1$) × order of the rotating frequency components when Z = 12 and P = 10, Z and P stand for slot number and pole number of the DE faulty motor, respectively. Similar to the SUMP, the Numerical results of the IUMP show that the IUMP has a large constant force in the offset direction and does not have any constant force in the orthogonal of the offset direction. The second largest component of IUMP is P × order. These conclusions are the same as the contents of Deduction 4.2.3 in the previous chapter. Moreover, in the axial direction, the additional constant and P × order components of IUMP are found in the numerical model due to the angular effect of the misalignment of the axis end point. However, this effect is ignored in the analytical model of IUMP. By using

numerical approach, additional useful diagnostic information, such as $P\times$ order component in axial direction, can be utilized to distinguish the IUMP from the SUMP. When the motor has a 10-poles and 12-slots (10P12S) combination structure, the Least Common Multiple (LCM) of pole and slot number is 60. Therefore, numerical results of AUMP validate Deduction 4.2.4 in Chapter 4 as follows: the AUMP has the $LCM\times$ order frequency components in the axial direction besides its constant force in the axial eccentricity (AE) direction. The analytical and simulation results of these four types of UMPs can match quite well. However, there are some differences in these two results, which would be due to the computational error. Through analytical approach in the previous chapter and numerical approach in this chapter, the conclusion can be drawn that $1\times$, $P\times$, $(P+1)\times$, and $LCM\times$ order components are effective to be employed to distinguish different types of UMPs induced by different rotor eccentricity faults in Permanent Magnet Synchronous Motor (PMSM).

The vibration induced by UPMs and Mechanical Unbalance (MU) in PMSM will be calculated in the following chapter.

CHAPTER 6

NUMERICAL COMPUTATION OF MOTOR RESPONSE INDUCED BY UNBALANCED MAGNETIC PULL AND UNBALANCED ROTOR

In the previous chapter, Unbalanced Magnetic Pulls (UMPs) numerical models of the Permanent Magnet Synchronous Motor (PMSM) have been developed to validate the analytical results of the four types of UMPs. However, measuring the UMPs in the PMSM is difficult. In order to validate the mathematical model of PMSM and analytical models of the UMPs, the natural frequency and the vibration signals induced by Mechanical Unbalance (MU) and different types of UMPs will be calculated in this chapter.

6.1 Introduction of Finite Element Analysis on Structure studies

On structure dynamic analysis, the basic idea of Finite Element Analysis (FEA) is to decouple the domain into a finite number of sub-domains (elements), using an approximate approach to calculate the stiffness matrix *K*, damping matrix *C* and mass matrix *M*. The general dynamic equation of motion of a global system can be represented by:

$$M\{\ddot{U}\} + C\{\dot{U}\} + K\{U\} = \{f\}, \tag{6.1}$$

where U is the vector of unknowns, and f the force vector. f may be time-dependent as $f(t)$. This equation can be used to calculate the dynamic response of the motor stationary parts.

If the relative rotating speed of the actual PMSM is above 3000 rpm, the equation will have additional contributions from the gyroscopic effect [G], and the rotating damping effect [B]. The inclusion of these two effects in the rotor dynamic response can be captured in the following modified equation of motion:

$$[M]\{\ddot{U}\}+[G]+[C]\{\dot{U}\}+[B]+[K]\{U\}=\{f\}. \tag{6.2}$$

6.2 Building a FEA model of PMSM

A general motor has been modeled by the lumped mass approach in Chapter 3. Although it is a simple and fast approach, it may lead to inaccurate results due to the usage of imprecise approximations in both the location and distribution of the system mass and the inertias employed in the process of simplifying the model.

The Finite Element Analysis (FEA) method offers a numerical approach to model the PMSM. It has the following advantages over the lumped mass method used in Chapter 3:

1) Accurate modeling of the mass and inertia of the rotor and stator;
2) The ability to include stationary parts (stator core, wiring, stator case and support structure) within the full model;
3) Direct utilization of a Computer Aided Design (CAD) model to mesh and perform the simulation.

Firstly, the geometries of the parts in the PMSM are built as CAD model, which subsequently is imported into the FEA environment. Then, the materials, boundary conditions, and elements are assigned to each part of PMSM to build the FEA model.

6.3 Modal analysis in the PMSM

Modal analysis is used to determine the natural frequencies and mode shapes of a structure or a machine component. With the exclusion of the excitation force $\{f\}$, and the damping effects as represented by $[B]$ and $[C]$, the natural frequencies and mode shapes of the structure can be obtained by this simplified equation:

$$[M]\{\ddot{U}\} + [G] + [K]\{U\} = 0 . \tag{6.3}$$

In ANSYS®, the Modal analysis is selected as the dynamic analysis type to solve the equation. The natural frequencies and mode shapes of the studying PMSM can be obtained as follows.

Figure 6.1 illustrates that the rotor's first natural frequency is 65.0582 Hz and the mode shape is in the axial direction. This can be attributed to the fact that the stiffness of the preload washer in the axial direction is lower than the ball bearing in the radial direction. On the other hand, Figure 6.2 shows the natural frequency in the radial direction. It is the second mode of the rotor's natural frequency. It can be observed that the COMBI214 element is deformed in the radial direction when there is relative rotating movement between the inner race and outer race of the ball bearing.

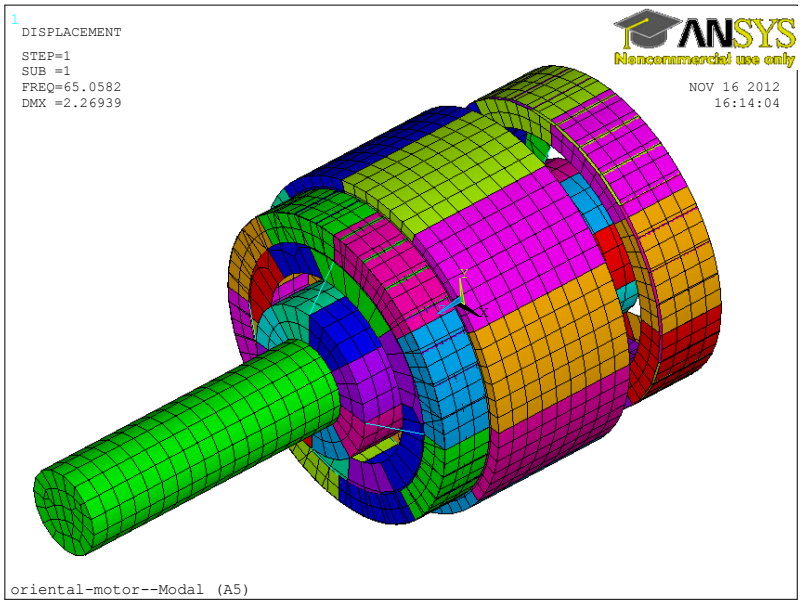

Figure 6.1: Rotor's first natural frequency in the axial translation

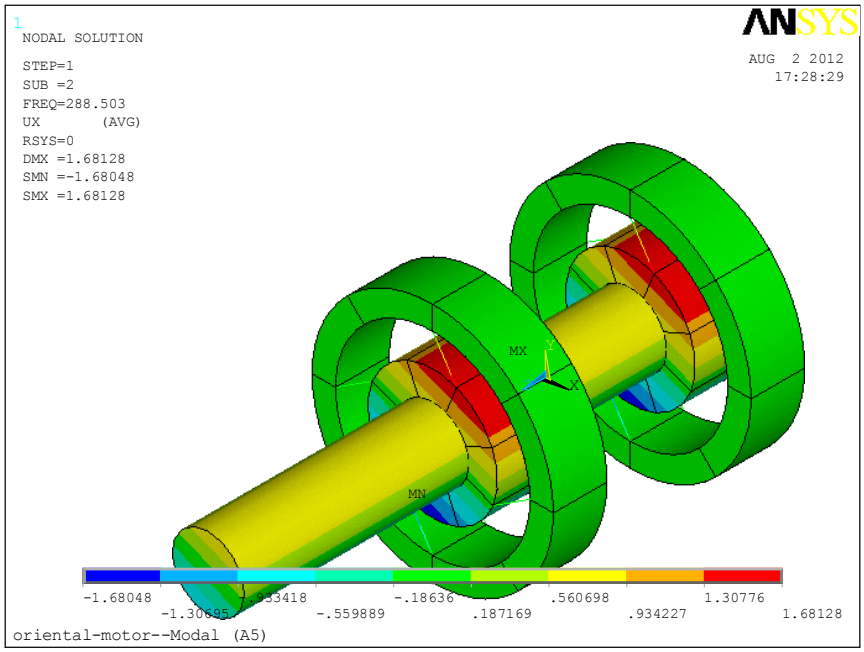

Figure 6.2: Rotor's natural frequency in first axial rotating

Figure 6.3 depicts that the rotor lateral sweep mode and mode frequency is 15504 Hz. The modal analysis results obtained by the analytical model and the simulation model are compared in Table 6.1. The difference of the first mode frequencies in axial and

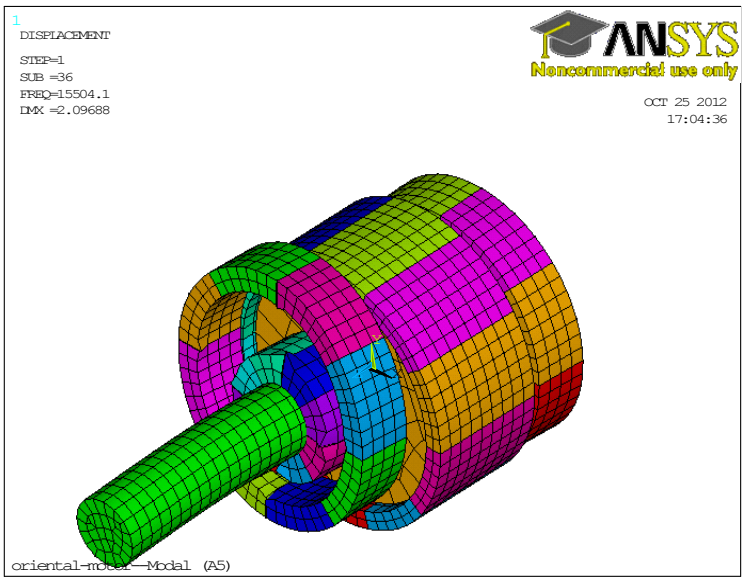

Figure 6.3: Rotor's natural frequency in first lateral translation

lateral directions is approximately 3%, implying that the analytical mode is accurate and can be used as a fast prediction of the PMSM's natural frequency when gyroscopic effect is not considered.

Table 6.1: Rotor natural frequencies comparison

Frequency	First mode (axial)	First mode (Lateral)	First backward	First forward
Analytical results	67.4 Hz	15080 Hz	246.7 Hz	305.5 Hz
Simulation results	65.058 Hz	15504 Hz	245.9 Hz	331 Hz
Difference	3.50%	2.68%	3.24%	7.70%

The first backward whirl and forward whirl frequencies are calculated based on the rotating speed of 3000 RPM. The difference of the former is also approximately 3%, implying that it can be effectively predicted by the analytical mode. However, the difference of the latter is approximately 7.7% due to using a simple lumped mass modeled as the continuous mass of rotor in the analytical model.

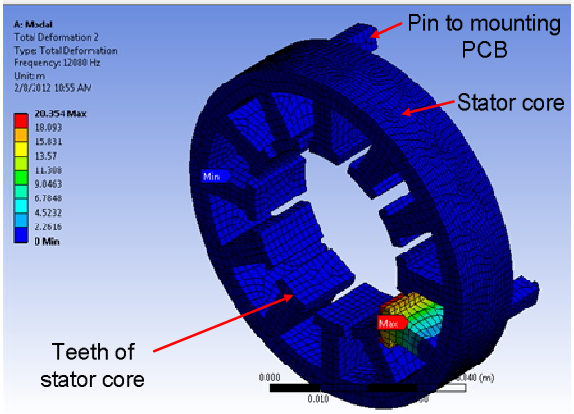

Figure 6.4: The first mode of stator teeth

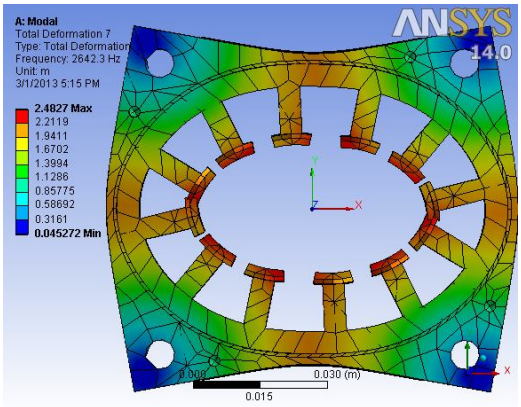

Figure 6.5: The second mode of the stator

In Figure 6.4 , it can be inspected that the lowest natural frequency of the stator teeth is in the first bending mode, and is 12080 Hz. This is in the high-frequency range compared to the excitation frequency of 50 Hz if the motor's rotating speed is 3000 RPM. The response amplitude can be speculated to be small and can be negligible.

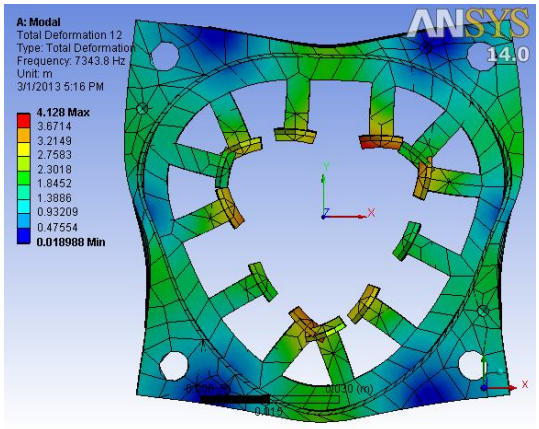

Figure 6.6: The third mode of the stator

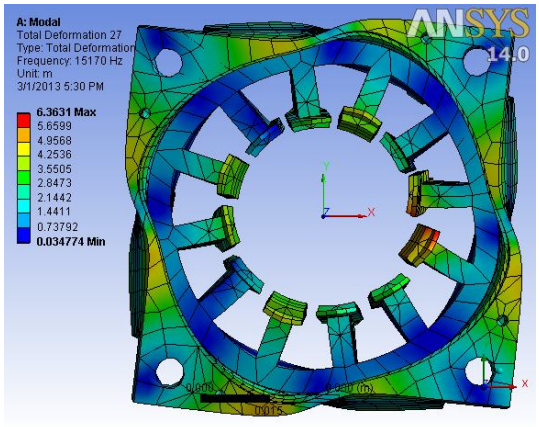

Figure 6.7: The fourth mode of the stator

Moreover, the frequencies of the second and higher modes of the stator teeth are at least 2 times greater than the fundamental frequency of the teeth, and the vibration amplitudes are much lower than the fundamental frequency of the teeth. This implies that the response signal of the teeth can be ignored for UMPs fault diagnosis purposes. Figures 6.5, 6.6 and 6.7 illustrate that the second, third and fourth modes natural frequencies of the stator core are 2642.3 Hz, 7343.8 Hz, and 11106 Hz

respectively. These frequencies should decrease if there is any crack on the motor case or motor stator. This is however beyond the scope of this thesis and may be considered in-depth for future studies.

The modal analysis results of the stator obtained by the analytical model and the simulation model are compared in Table 6.2. The difference of these four modes frequencies of stator are also less than 5%, implying that the analytical mode is effective and can be used as a first prediction of the natural frequency of the stator.

Table 6.2: Stator natural frequencies comparison

Frequency	First mode (teeth)	Second mode (stator and case)	Third mode (stator and case)	Fourth mode (stator and case)
Analytical results	11727 Hz	2666 Hz	7543 Hz	14463 Hz
Simulation results	12080 Hz	2642 Hz	7343 Hz	15170 Hz
Difference	2.92%	0.90%	2.65%	4.66%

It can be observed that either the first mode of the natural frequency of the teeth or the first few modes of the stator case's natural frequency are more than 2500 Hz. This implies that the response signal of the teeth can be ignored for UMPs fault diagnosis purposes.

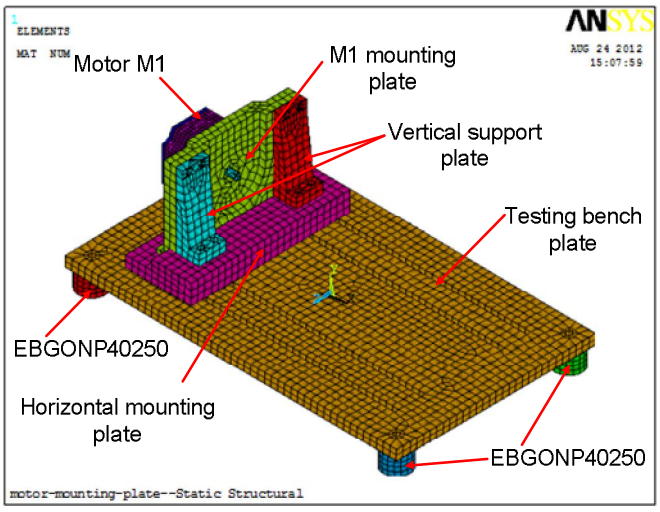

Figure 6.8: 12S5PP motor with mounting fixture meshing

In order to comprehend the PMSM vibration behaviors, the mounting fixtures of the PMSM should be elucidated. Figure 6.8 depicts the mesh of the whole model with mounting fixture. The mesh size of the PMSM is 2mm, the mesh sizes of the motor mounting plate, vertical support plate, and horizontal mounting base are increased to 5mm, and the mesh size of the testing bench plate is increased to 10mm in order to reduce the computational time.

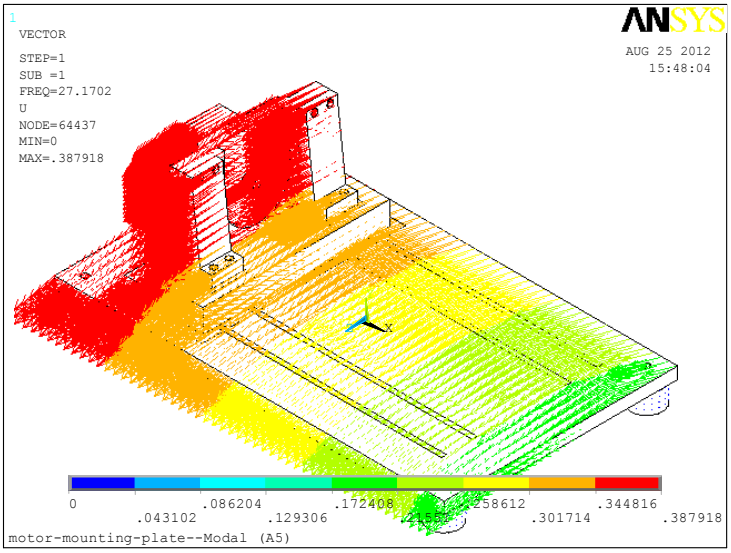

Figure 6.9: The first mode of 12S5PP motor with mounting fixture

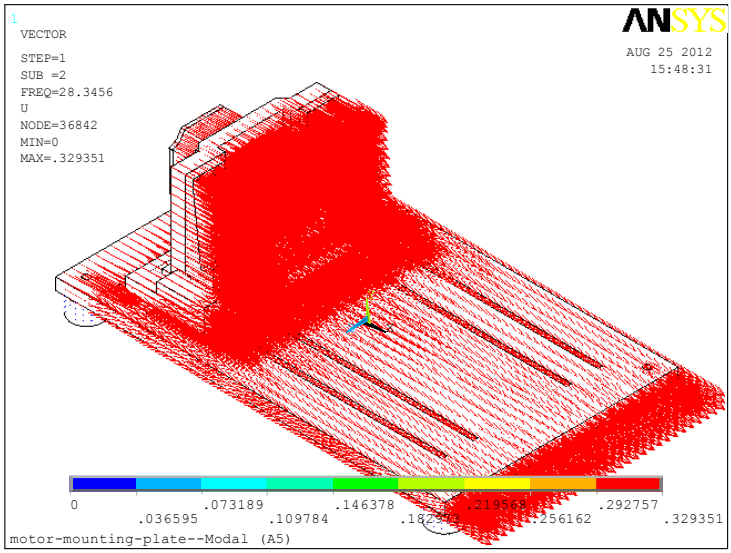

Figure 6.10: The second mode of 12S5PP motor with mounting fixtures

Figures 6.9 and 6.10 show the frequencies of the first and second modes of the whole system. The two frequencies, 27.17 Hz and 28.35Hz, are in the horizontal movement of the base with flexible mounting EBGONP40250. The stiffness of EBGONP40250 in vertical and horizontal direction is 340N•mm and 78.2 N•mm respectively.

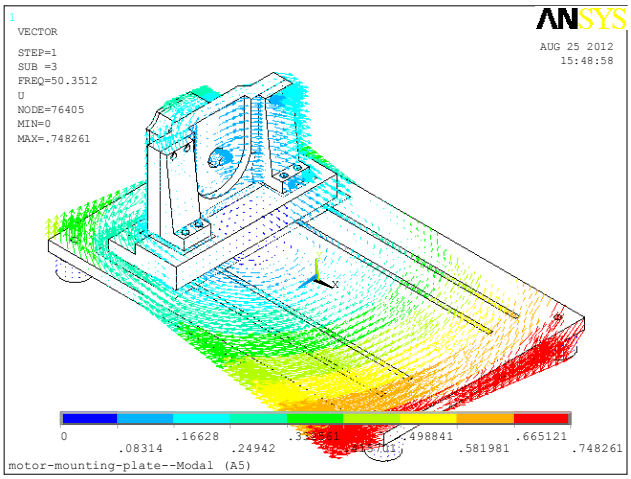

Figure 6.11: The third mode of 12S5PP motor with mounting fixtures

Figure 6.11 illustrates the first rotating mode of the whole testing system. It can be observed that the whole system with the testing bench is rotating along the y axis with a frequency of 50.3512Hz.

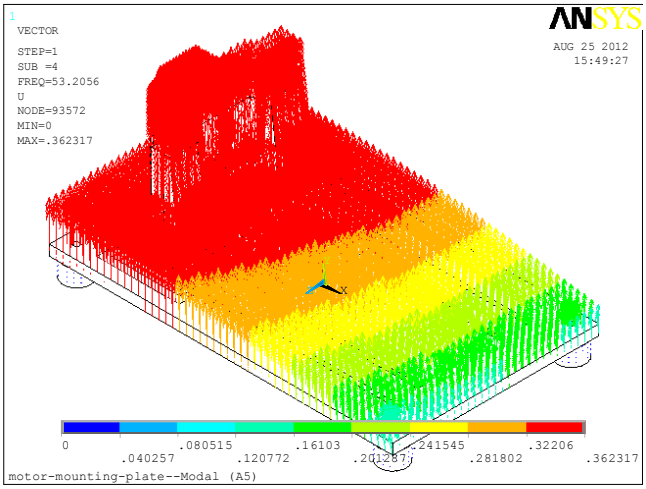

Figure 6.12: The fourth mode of 12S5PP motor with mounting fixtures

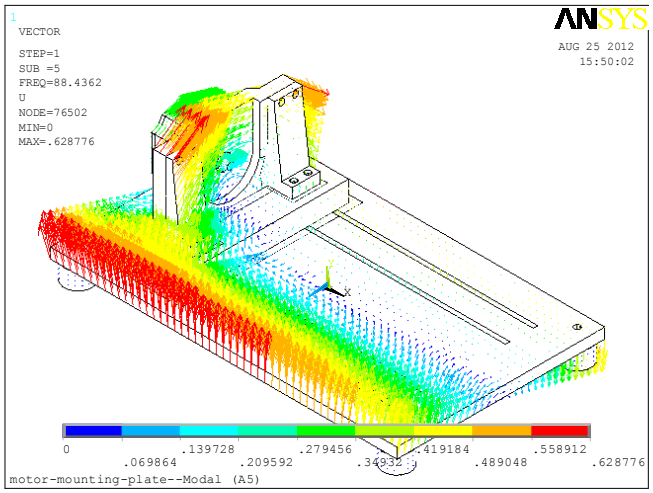

Figure 6.13: The fifth mode of 12S5PP motor with mounting fixtures

Figure 6.12 shows the frequency with 53.2056 Hz in the vertical movement of the base with flexible mounting. The frequency of the vertical movement of the whole system is higher than the frequency of the horizontal movement, the reason being that the stiffness of the EBGONP40250 anti-vibration pad in the vertical direction is higher than that in the horizontal direction.

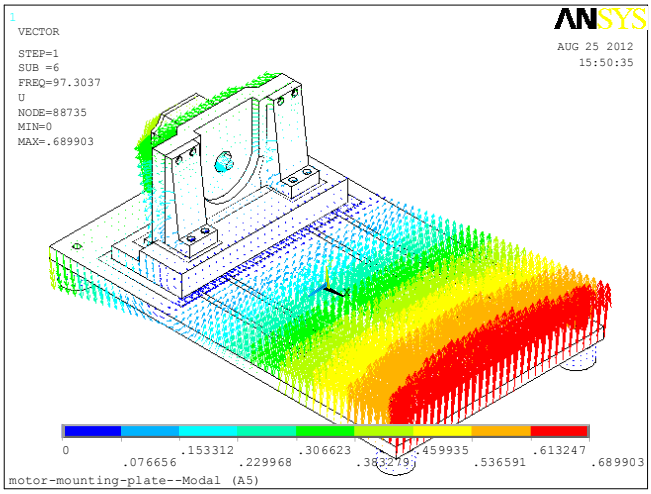

Figure 6.14: The sixth mode of 12S5PP motor with mounting fixtures

Figures 6.13 and 6.14 depict the rotating frequencies 88.43 Hz and 97.3 Hz of the whole system along the x and z axes. Although the stiffness of EBGONP40250 in

the x and z directions is the same, the rotating frequency is different in these directions because the moment of inertia of the whole system is different in these two directions. The modal analysis results of testing bench obtained by the analytical and the simulation models are compared in Table 6.3. The difference of these first two translational (in x and y) and three rotating mode is less than 6%, implying that the analytical mode in Chapter 3 is accurate and can be used as the fast prediction of testing bench's natural frequency. However, the difference of the vertical movement in z is approximately 10.5% due to using a simple lumped mass modeled as the continuous mass of the testing bench.

Table 6.3: Motor grounding natural frequencies comparison

Frequency	Lateral movement(X)	Lateral movement(Y)	Vertical movement(Z)	Rotating by XX	Rotating by YY	Rotating by ZZ
Analytical results	28.75 Hz	28.75 Hz	59.45 Hz	89.76 Hz	48.36 Hz	96.9 Hz
Simulation results	27.17 Hz	28.34 Hz	53.2 Hz	88.43 Hz	50.35 Hz	97.3 Hz
Difference	5.49%	1.43%	10.50%	1.48%	3.95%	0.41%

6.4 Transient analysis in the PMSM

In order to simulate the vibration of the PMSM induced by different types of UMPs and MU, the transient analysis should be used. The reason is that different types of UMPs studied in Chapters 4 and 5 have multiple frequencies as the excitation forces and the harmonic analysis can handle only a single frequency force vibration.

Three methods can be used to perform the transient analysis: the full method, the mode-superposition method and the reduced method [68]. The full method entails comparatively time-consuming computations. The reduced method is faster because it uses reduced (condensed) system matrices to calculate the solution. However, it is less

accurate because the reduced mass matrix is approximate. Therefore, in this thesis, the mode-superposition method is chosen for reducing computational time and improving the accuracy of analysis. The disadvantage of using the mode-superposition method is that the whole system modal analysis should be conducted as the first step, following which the mode frequencies and shapes can be used in the transient analysis. However, this modal analysis was conducted in Section 6.3 and the results can be reused to overcome the shortcomings of the mode-superposition method.

6.4.1 Dynamic responses of Mechanical Unbalance

Based on the equation (4.2) in Chapter 4, the Mechanical Unbalance (MU) is a single frequency excitation force and the dynamic responses of MU can be solved by harmonic analysis. However, transient analysis is instead employed herein to establish the consistent comparisons between the dynamic responses of MU and those of UMPs.

Table 6.4: Mechanical Unbalance force used for vibration simulation

Unbalance Mass(kg)	Unbalance mass position(m)	Motor Speed(ω)	Unbalance force(N)
0.004	0.015	314	5.91576
0.004	0.025	314	9.8596
0.004	0.035	314	13.80344
0.008	0.035	314	27.60688

Table 6.4 illustrates the MU excitation forces when the motor has four grades of Mechanical Eccentricity (ME) faults. The ME faults generate *1* × order vibration of the motor running speed; such numerical results of the vibration induced by different grades of ME faults are shown in Figure 6.15. Moreover, the amplitude of *1* × order vibration signal in the radial direction increases with eccentricity mass m_u. This numerical results demonstrate that *1* × order vibration signal could be used as the faulty feature of ME fault.

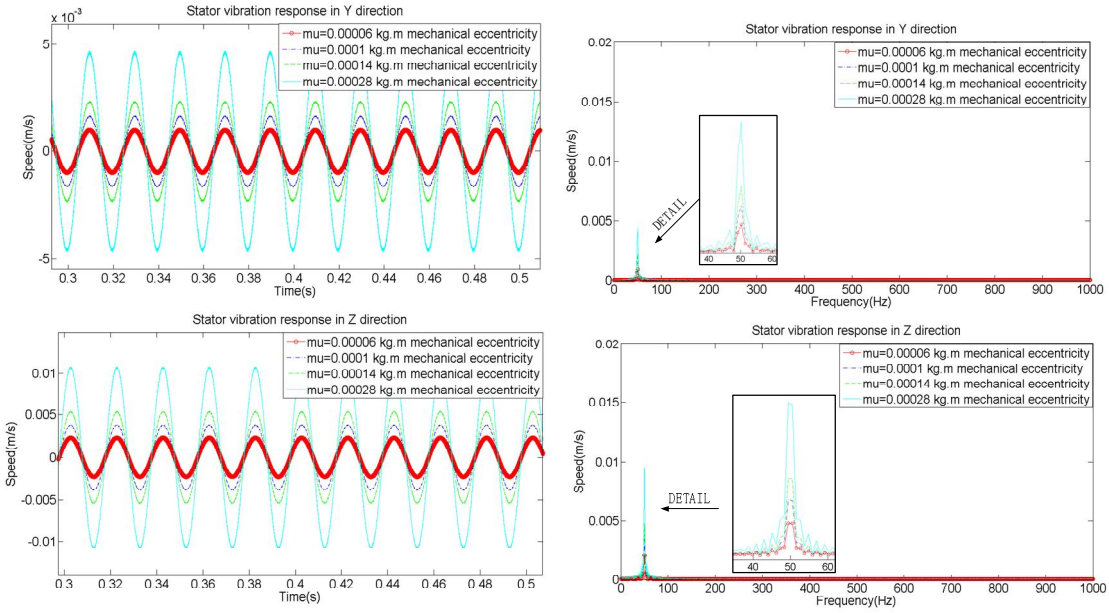

Figure 6.15: Dynamic responses with MU in time and frequency domains

6.4.2 Dynamic responses of Static Unbalanced Magnetic Pull

The numerical results of the Static Unbalanced Magnetic Pull (SUMP) obtained in Chapter 5 are used as the excitation forces in order to study dynamic responses of the motor which possesses the Static Eccentricity (SE) fault. Using approximately 20 points per cycle of SUMP, the sampling frequency is set to 10000 Hz. However, the high frequency components of the UMPs should be filtered by a low pass filter in the simulation model to prevent unconverted errors. The original and the filtered SUMP time domain signals in x and y directions are illustrated in Figures 6.16 and 6.17. The smooth signal is obtained by applying a low-pass filter. These filtered signals can then be used to build the input force table for FEM.

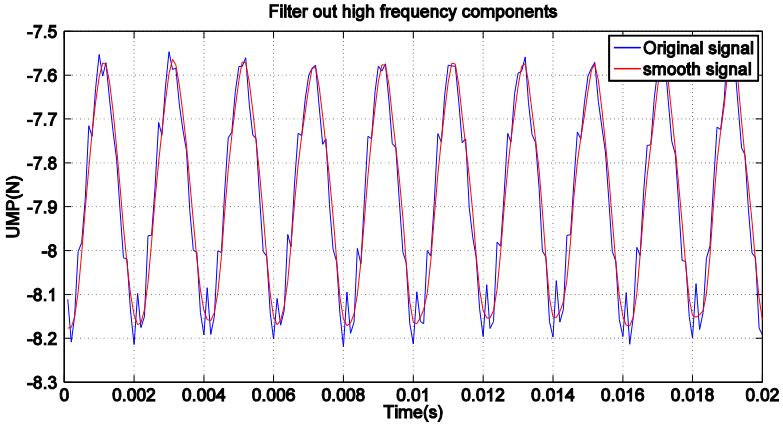

Figure 6.16: The original and filtered signals of the SUMP in y direction

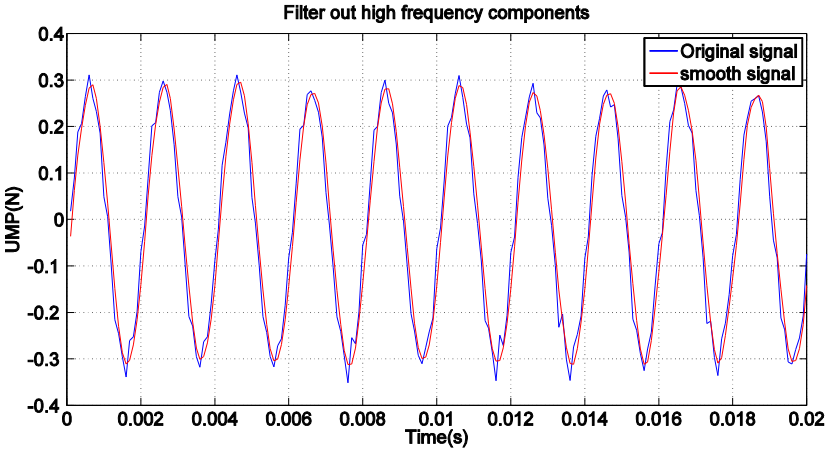

Figure 6.17: The original and filtered signals of the SUMP in z direction

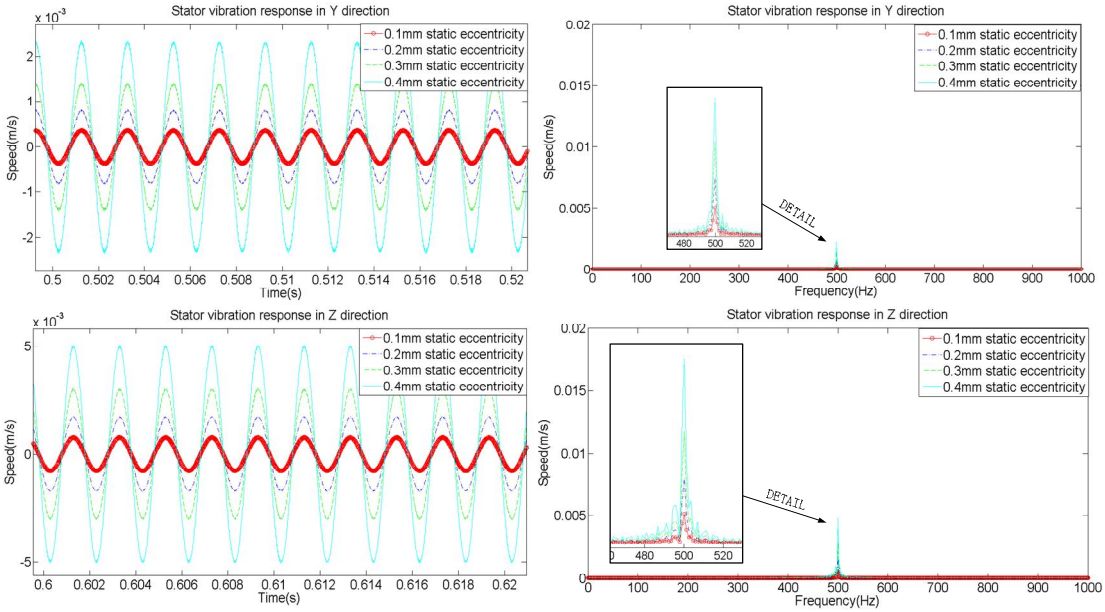

Figure 6.18: Dynamic responses of SUMP in time and frequency domains

The dynamic responses of SUMP in the radial direction with different grades of SE fault are shown in Figure 6.18. It can be observed that the vibration level in the y direction is nearly two times of that in the z direction, in terms of the time-domain or frequency domain. The reason is that the stiffness of the motor mounting fixture in the y direction is different from that in z direction. Moreover, in the time and frequency domains, the vibration level increases with faulty grades of SE. Furthermore, in the frequency domain, it can be inspected that the fundamental frequency of the vibration induced by SUMP is 500 Hz. The conclusion can be drawn that 500 Hz vibration signals can be utilized as the diagnostic feature of the SE faults.

6.4.3 Dynamic responses of Dynamic Unbalanced Magnetic Pull

The numerical results of the Dynamic Unbalanced Magnetic Pull (DUMP) obtained in the previous chapter are adopted as the excitation forces to study the dynamic responses of the motor which has the Dynamic Eccentricity (DE) fault. As with the dynamic responses of the SUMP, the high orders harmonic of DUMP should be filtered by a low pass filter to prevent unconverted errors before the force is applied on the motor in the simulation model. The original signal and filtered signal in the y and z directions are shown in Figures 6.19 and 6.20.

Figure 6.21 illustrates the transient analysis results of the motor under different grades of DE faults in the radial direction. It can be observed that the vibration amplitudes in the y and z directions increase with grades of DE faults in the time and frequency domains. The vibration amplitudes of 50 Hz and 550 Hz in y direction are smaller than those of 50 Hz and 550 Hz in z direction. In the frequency domain, it

can be inspected that the influence of the 50 Hz component of the DUMP is the strongest, with the second strongest being the 550 Hz component of the DUMP. Therefore, These numerical results prove that these two vibration signals could be adopted as the DE diagnostic feature to diagnose a DE fault in the PMSM.

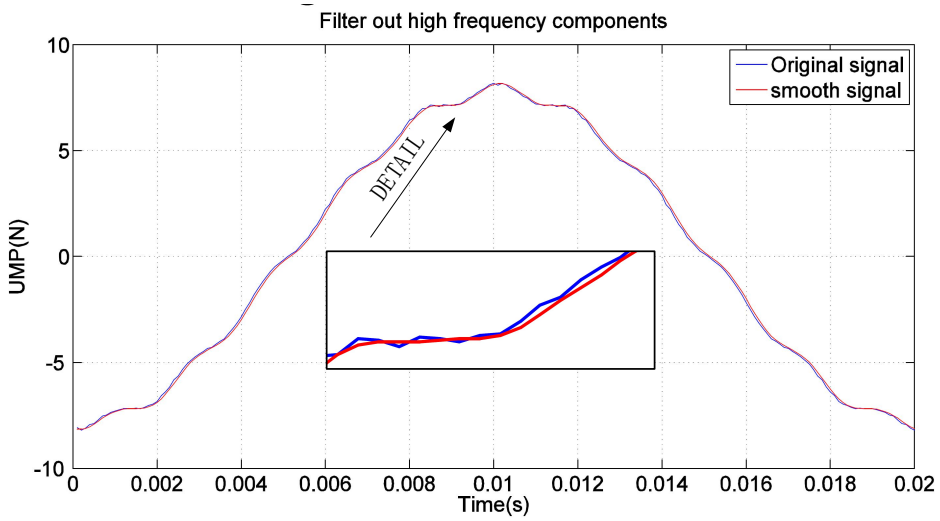

Figure 6.19: The original and filtered signals of DUMP in the y direction

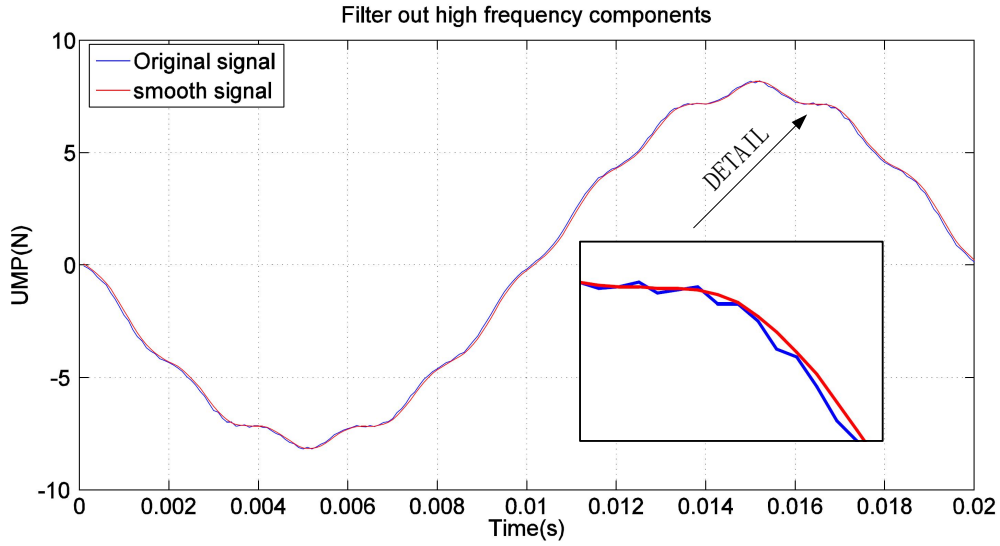

Figure 6.20: The original and filtered signals of DUMP in the z direction

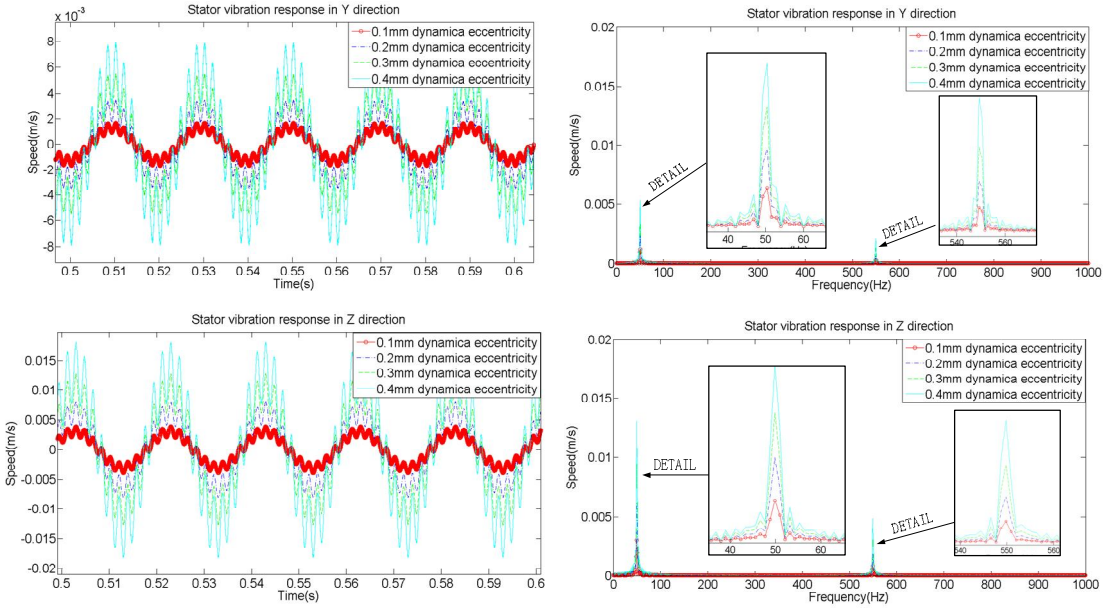

Figure 6.21: Dynamic responses with DUMP in the time and frequency domains

6.4.4 Dynamic responses of Inclined Unbalanced Magnetic Pull

The numerical results of the Inclined Unbalanced Magnetic Pull (IUMP) obtained in Chapter 5 are used as the excitation forces to study dynamic response of the motor with the Inclined Eccentricity (IE) fault.

The dynamic responses of IUMP in the x, y and z directions in the time and frequency domains are shown in Figure 6.22. It can be observed that the dominant frequency is 500 Hz in the x, y and z directions and the vibration amplitudes increase with faulty grades of the IE faults. Although the IUMP in the x direction is smaller than those in the y and z directions, the vibration level is the largest. The reason is that the motor stiffness in the x direction is smaller than the stiffness in the other two directions. The conclusion can be drawn that these three vibration signals can be adopted as the diagnostic feature for a IE fault in the PMSM.

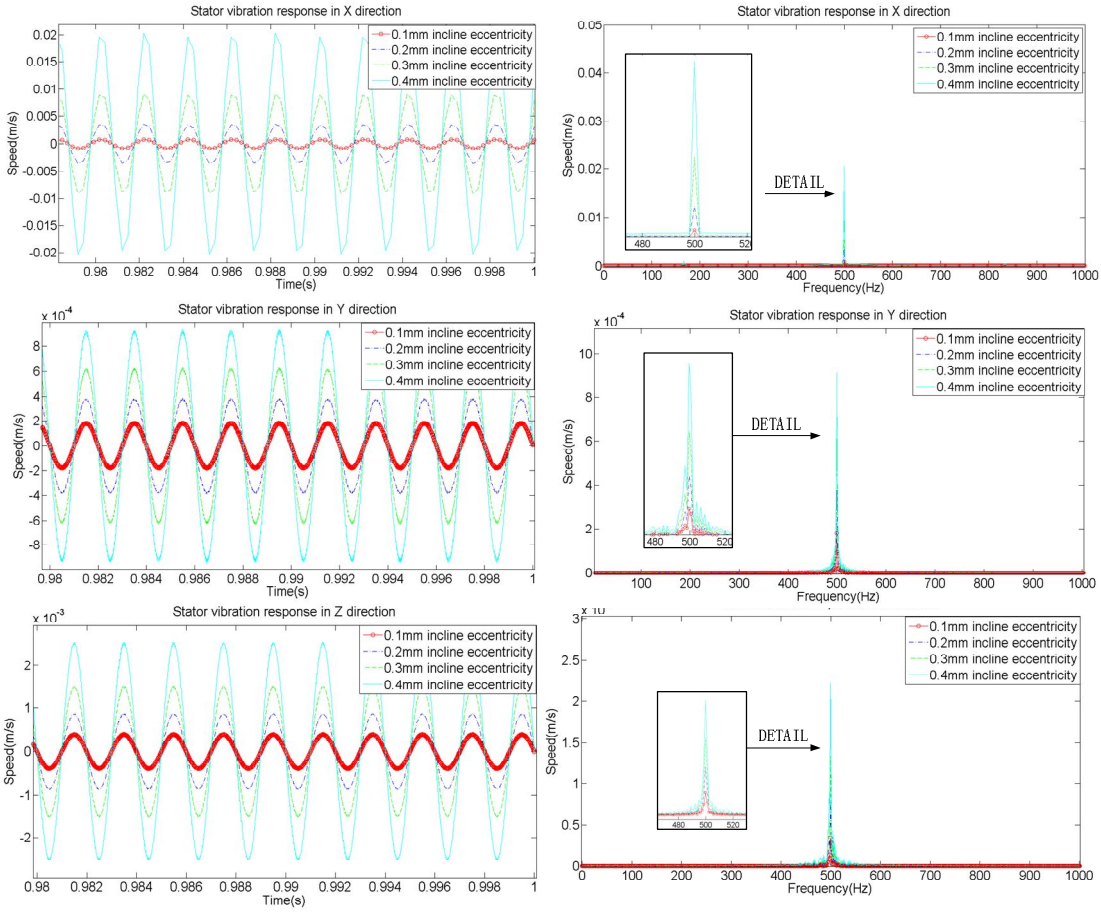

Figure 6.22: Dynamic responses with IUMP in the time and frequency domains

6.4.5 Dynamic responses of Axial Unbalanced Magnetic Pull

The numerical results of the Axial Unbalanced Magnetic Pull (AUMP) obtained in Chapter 5 are used as the excitation forces to study dynamic response of the motor which has the Axial Eccentricity (AE) fault. As with the transient analysis of SUMP, DUMP and IUMP, the low pass filter should be applied to filter out high frequencies of AUMP, in this case, the cut-off frequency of the low pass filter should be above 3000 Hz.

The dynamic responses of the AUMP with various grades of AE faults in the axial direction are shown in Figure 6.23.

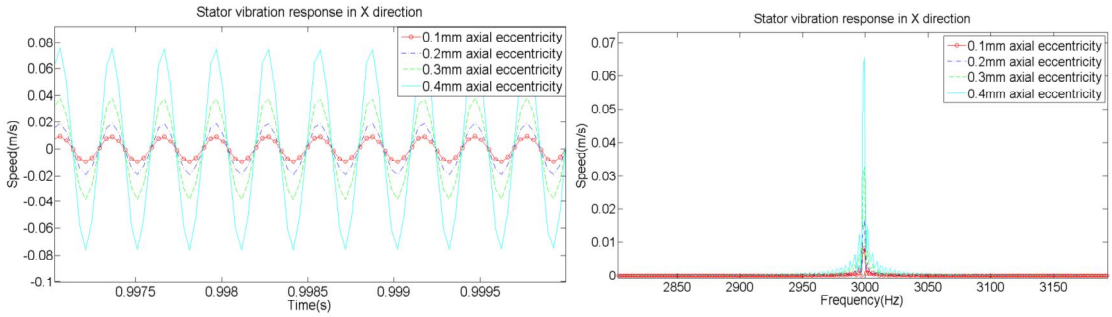

Figure 6.23: Dynamic responses with AUMP in the time and frequency domains

It can be inspected that the vibration amplitudes increase with axial eccentricity distance in the time and frequency domains. The main contribution frequency is 3000 Hz. Therefore, 3000 Hz vibration signals in the axial direction can be used as the diagnostic feature for an AE fault in the PMSM.

6.5 Conclusions

In this chapter, the rotor natural frequency, and forward and backward whirling frequencies are calculated by using finite element method. The FEM numerical results obtained confirm the effectiveness of the analytical mode presented in Chapter 3 as the difference of the most of modal analysis results between the analytical model and the numerical model is less than 5%, implying that the analytical mode is accurate and can be used as fast prediction of the PMSM's natural frequency. The vibration results induced by MU and UMPs are obtained by applying the FEM transient analysis. The transient analysis results of vibration induced by MU show that *1* × order of motor frequency is the dominant frequency and can be used as the diagnostic feature for an

ME fault. The diagnostic feature of the SE fault is the $P\times$ order frequency (where P stands for pole number). On the other hand, the diagnostic features of the DE fault are the $1\times$ and $(P+1)\times$ order frequencies. Although the fundamental frequency of the IUMP is the same as that of the SUMP, the difference between the SUMP and the IUMP is that an additional vibration in the axial direction can be found in the IE faulty motor. By using this additional feature, the IE and SE faults can be distinguished. Other than the SE, DE, IE and MU faults, the transient analysis results of vibration induced by AUMP demonstrate that the fundamental frequency of the vibration in the AUMP is the number of LCM of the number of poles and slots which are much higher than the fundamental frequencies of other types of UMP faults.

It can be concluded that the $1\times$, $p\times$, $1\times$ with $(p+1)\times$ and $LCM\times$ order vibration signals in the x, y and z directions can be utilized as the diagnostic features for the ME, SE, DE, IE and AE faults of the motor. The numerical results of the vibration induced by MU and UMPs in the PMSM will be validated by the experimental results in the following chapter.

.

CHAPTER 7

EXPERIMENTAL STUDIES ON MOTOR RESPONSE INDUCED BY UNBALANCED MAGNETIC PULL AND UNBALANCED ROTOR

In the previous chapters, analytical and simulation models have been developed to predict the vibration induced by Mechanical Unbalance (MU) and Unbalanced Magnetic Pulls (UMPs). The purpose of this chapter is to design an experimental platform and use the experimental results to validate the predicted results in the previous chapters.

7.1 Dynamic responses of healthy motor

7.1.1 Experimental platform design

Figure 7.1 demonstrates an experimental platform for measuring the vibration induced by MU, which is caused by Mechanical Eccentricity (ME) fault, UMPs-related fault, such as Static Eccentricity (SE), Dynamic Eccentricity (DE), Inclined Eccentricity (IE), and Axial Eccentricity (AE) faults on the anti-vibration table. A modified Permanent Magnet Synchronous Motor (PMSM) is mounted on a testing bench with four EBGONG40250 vibration isolator pads. The PMSM is controlled by an NI DAQ card BNC-2110 with a BLHD50K motor driver. Two Polytec OFV-5000 Laser Doppler vibrometers (LDVs) are employed to measure the velocity power spectrum of the points on the out surface of the PMSM.

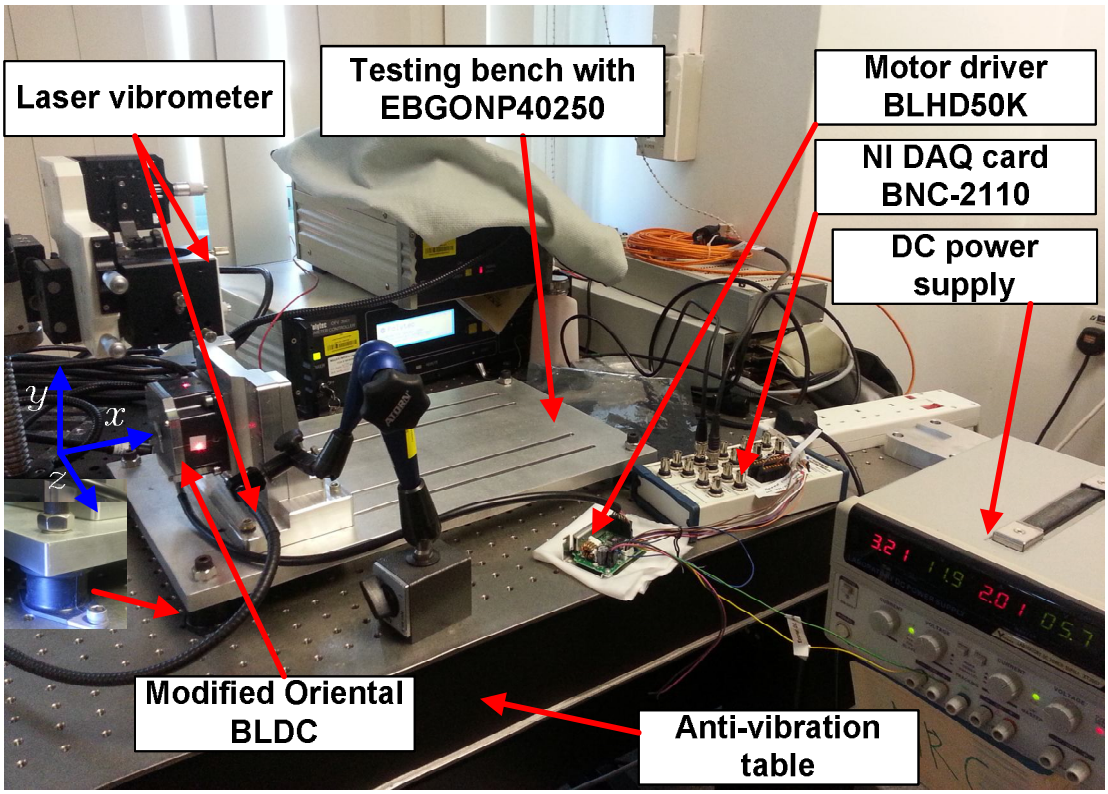

Figure 7.1: Rotor eccentricity-induction measurement setup

7.1.2. Experimental results and discussion

The data in time domain is measured by two LDVs and the results are plotted as seen in Figure 7.2. However, the vibration signal in time-domain could not reveal the clues of the faulty motor. As it was mentioned by Silva [60], the frequency-domain signals can be used for fault diagnostic work, as different machine conditions generate characteristic fault patterns that are usually detectable in the frequency domain. Therefore, some frequencies related to the PMSM rotor eccentricity faults could be extracted by applying Fourier transform (FT) and indicated as the fault frequencies. Furthermore, a frequency-domain signal with waterfall is employed to find the suitable motor diagnosis running speed. Consequently, the diagnostic feature signals studied in the previous chapter are to be validated by the experimental results in this chapter.

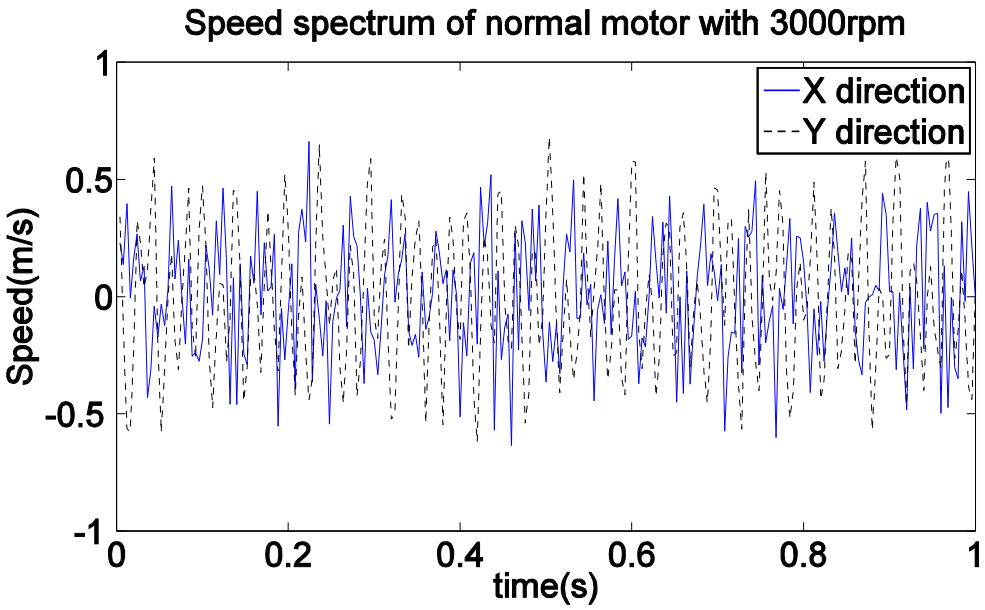

Figure 7.2: Time domain data of healthy motor in x and y directions

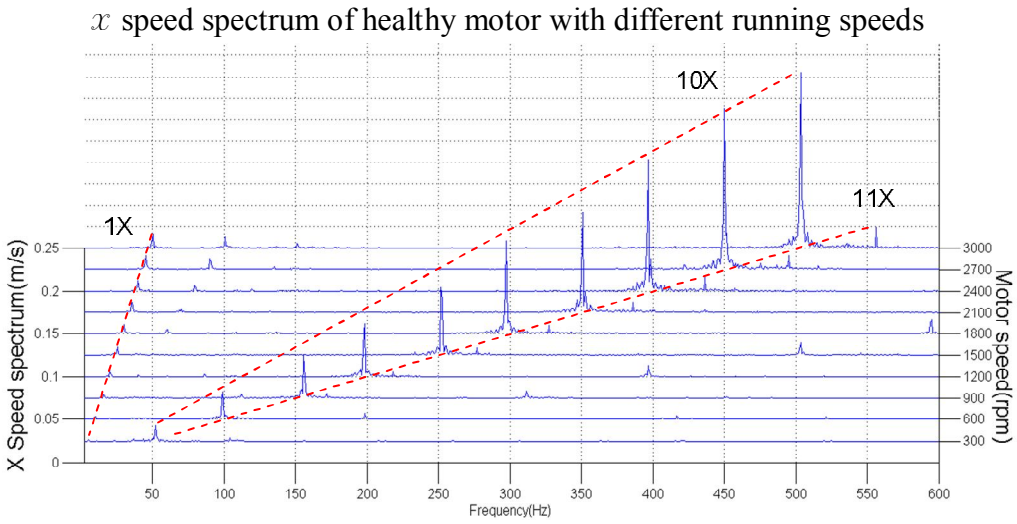

Figure 7.3: Frequency domain data of healthy motor in x direction (<600Hz)

Figures 7.3 and 7.4 show the waterfall with various speeds of a healthy motor (with no faults at all) in the x direction. In Figure 7.3, $10\times$ order harmonics have largest amplitude because the experimental motor has 10 poles and 12 stator slots. In either healthy or faulty motors, $10\times$ order signal is the driving frequency. However, the amplitude of this frequency increases if the motor has static eccentricity or inclined

eccentricity fault. In Figure 7.4, though there are many peaks show up to 4000 Hz, these frequencies may belongs to motor test bench. Those frequencies do not change when different faulty motor were used in experiment. We shall do further analyze on these frequencies in future studies by using other types of motors and testing benches. However, in these two figures, the amplitudes of the $1\times$, $10\times$, $11\times$, and $60\times$ order signals increase with motor running speed. Moreover, when the speed is 3000 RPM, the largest amplitudes of these four signals could be used as the diagnostic features if these four signals have the same trends in the ME, SE, DE, IE and AE faulty motors. Using the same approach, the waterfall in the y and z directions can be plotted. All amplitudes of these frequencies can be extracted from the waterfall and are listed in Table 7.1.

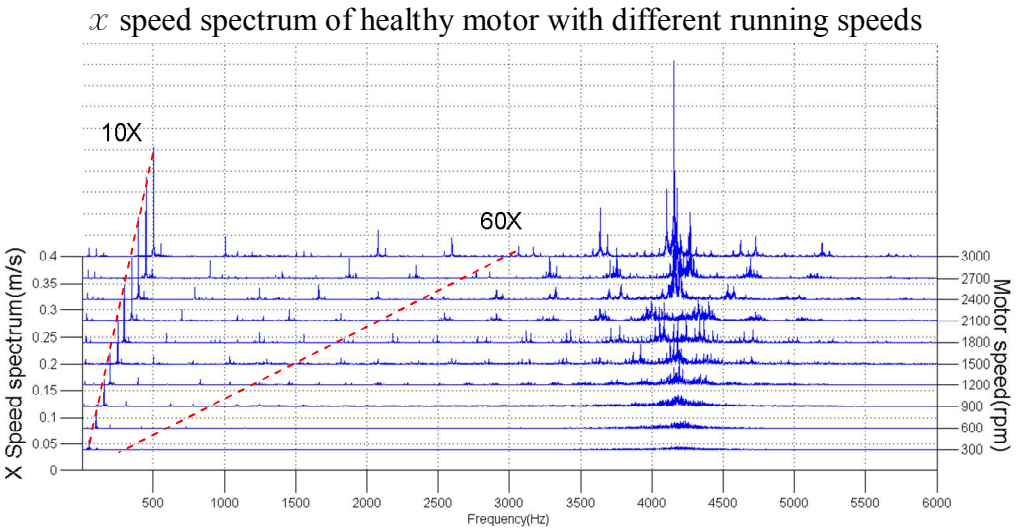

Figure 7.4: Frequency domain data of healthy motor in x direction (<6000Hz)

Table 7.1: Vibration signals of healthy motor at 3000 RPM

x				*y*				*z*			
50Hz	500Hz	550Hz	3000Hz	50Hz	500Hz	550Hz	3000Hz	50Hz	500Hz	550Hz	3000Hz
0.0166	0.2052	0.02446	0.01898	0.02898	0.1612	0.02217	0.01848	0.03477	0.1935	0.02648	0.02218

7.2 Dynamical responses of Mechanical Unbalance

7.2.1 Experimental design for Mechanical Unbalance

The Mechanical Unbalance (MU) is a common excitation source of motor vibration due to Mechanical Eccentricity (ME) fault of the motor's rotor. MU was simulated by attaching an unbalance aluminum disk to the motor rotor shaft. There were six Ø3.1 holes made symmetrically at both sides of the disk as shown in Figure 7.5, where the M3 screw and nut could be mounted to produce unbalanced mass. Based on the weight and position of the mounted screw and nut, different mass unbalance forces under different running speed can be calculated. The prototype of the unbalance disk is shown in Figure 7.6.

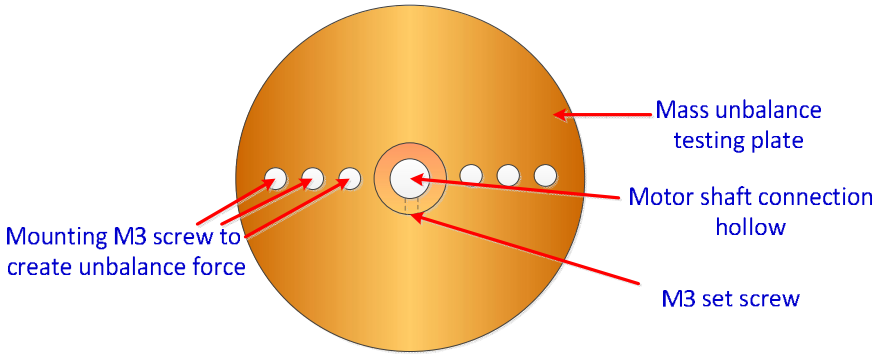

Figure 7.5: Mechanical Unbalance disk

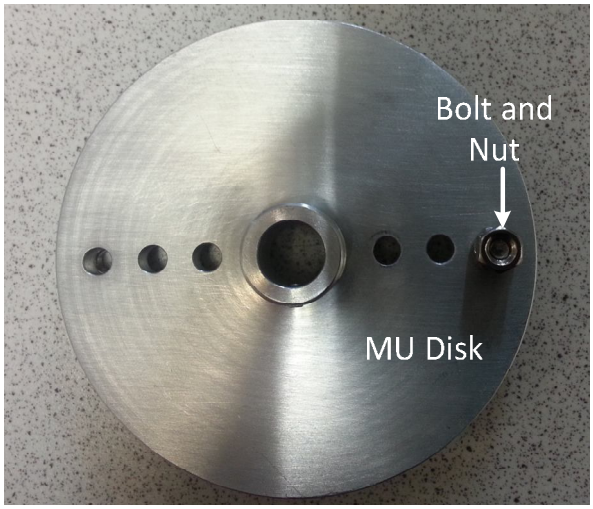

Figure 7.6: Mechanical Unbalance disk prototype

Referring to equation(4.2), the force vibration equation can be built:

$$F = mr\omega^2 \sin \omega t. \tag{7.1}$$

The mass of the M3 bolt is 1.6 g, M3 nuts is 1.4 g, and the unbalance distance is 15 mm. Using equation (7.1), the MU force due to different grades of ME can be calculated when the motor is running under 3000 RPM.

Table 7.2: MU under different grades of ME fault

Faulty grades	Unbalance Mass(kg)	Unbalance mass position(m)	Motor Speed(ω)	Unbalance force(N)
e1	0.004	0.015	314	5.91576
e2	0.004	0.025	314	9.8596
e3	0.004	0.035	314	13.80344
e4	0.008	0.035	314	27.60688

7.2.2 Experimental results and discussion for MU

The experimental results of the vibration induced by MU under various grades of ME faults at 3000 RPM are summarized in Table 7.3. It can be observed that only 50 Hz signals in y and z directions are significantly changed.

Table 7.3: Experimental results of vibration induced by MU with different grades of ME faults

Faulty grades	x (m/s)				y (m/s)				z (m/s)			
	50Hz	500Hz	550Hz	3000Hz	50Hz	500Hz	550Hz	3000Hz	50Hz	500Hz	550Hz	3000Hz
e0	0.016600	0.205200	0.024460	0.018980	**0.028980**	0.161200	0.022170	0.018480	**0.034770**	0.193500	0.026480	0.022180
e1	0.016623	0.205234	0.024498	0.019010	**0.029965**	0.161233	0.022189	0.018512	**0.037000**	0.193519	0.026513	0.022219
e2	0.016638	0.205239	0.024483	0.019014	**0.030830**	0.161222	0.022206	0.018507	**0.038330**	0.193536	0.026484	0.022208
e3	0.016623	0.205235	0.024502	0.019045	**0.031500**	0.161219	0.022197	0.018522	**0.039690**	0.193526	0.026515	0.022212
e4	0.016625	0.205226	0.024498	0.019009	**0.033820**	0.161212	0.022218	0.018499	**0.044620**	0.193534	0.026529	0.022212

Figure 7.7 compares the experimental and simulation results at 50Hz in the y and z directions. It can be observed that the experimental results match quite well with the simulation results when the motor has different grades of ME faults at 3000 RPM. Although the mechanical eccentricity forces in the y and z directions are the same, the vibration amplitudes are different as the system structure is different in the y and z directions. The 50 Hz components increase in y and z directions with ME faulty

grades. Therefore, the 50Hz frequency components in the radial direction can be utilized as the diagnostic features for ME fault.

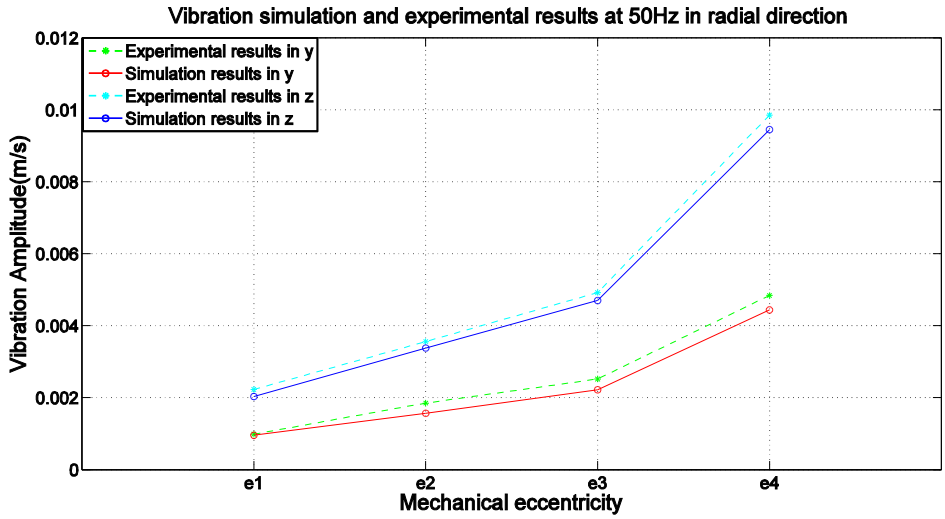

Figure 7.7: Comparison between the experimental and simulation results with 4 faulty grades of ME faults at 3000 RPM

7.3 Dynamical responses of Static Unbalanced Magnetic Pull

7.3.1 Experimental design for Static Unbalanced Magnetic Pull

The Static Unbalanced Magnetic Pull (SUMP) is generated by static eccentricity (SE) fault of the motor's rotor. The average air-gap in the healthy motor used in this study is 0.5mm. Therefore, the offset distance between the center of the inner race and outer race of the SE ring were designed and made in the range of 0.1 to 0.4mm as shown in Figures 7.8 and 7.9. The slot at the ring is designed to ensure that both sides of the static eccentricity remain in the same direction, and prevent the outer race of the bearing from moving when the rotor rotates.

Using the SE ring, geometrical center of the rotor has been offset to the center of the stator core. However, both the offset direction and distance are not changed in the rotor's rotation. The assembly design and prototype are shown in Figures 7.10 and

7.11. In these two figures, a uniform inner ring is interference-fit between the rotor shaft and inner race of the ball bearing. The outer race of the ball bearing is transition-fit to the SE ring.

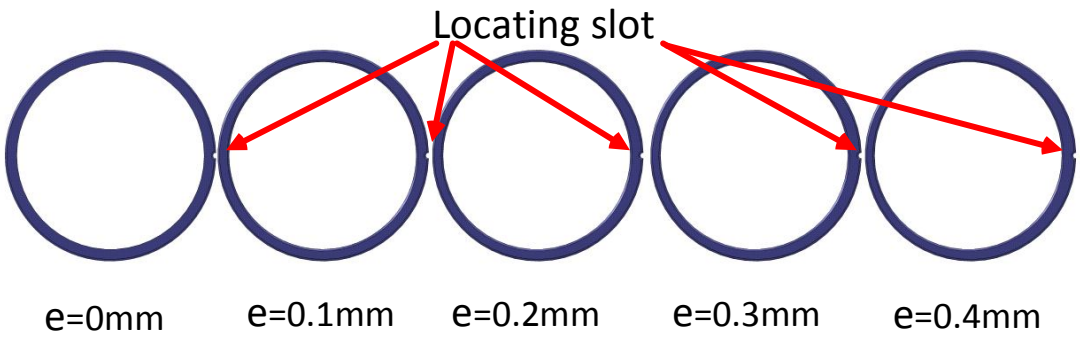

Figure 7.8: SE rings with 4 faulty grades structures

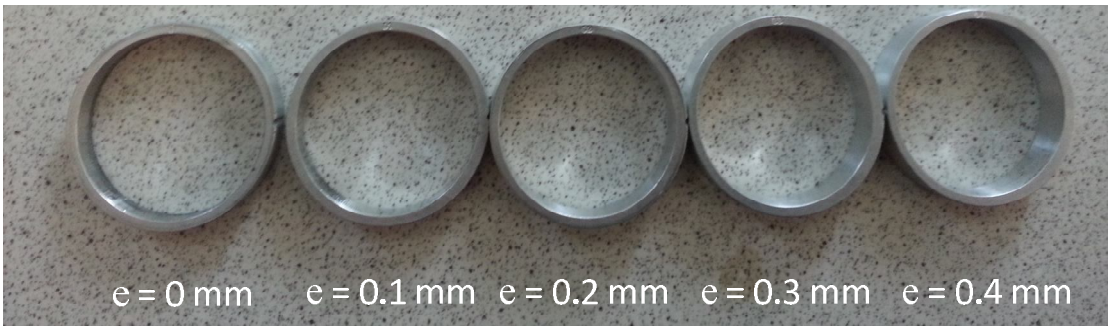

Figure 7.9: Prototype of SE rings with 4 faulty grades structures

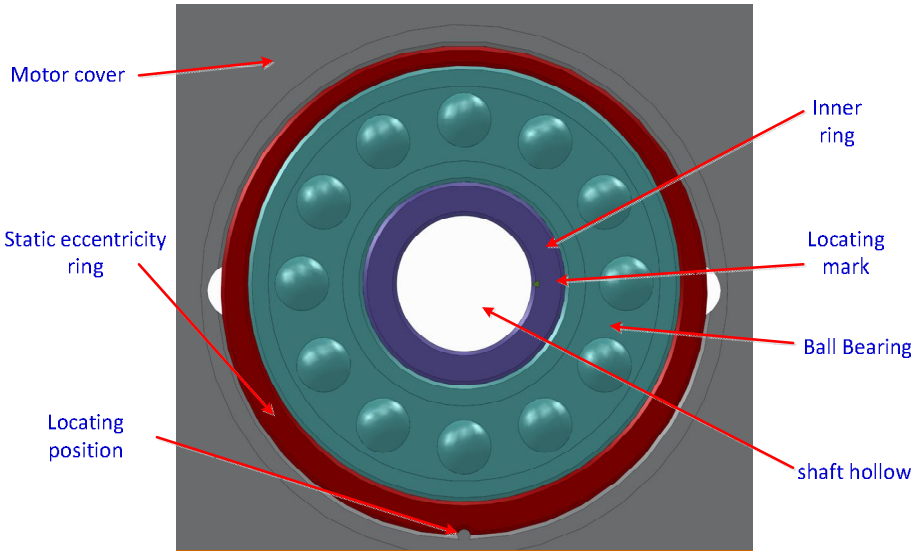

Figure 7.10: Structure design to simulate motor SUMP fault

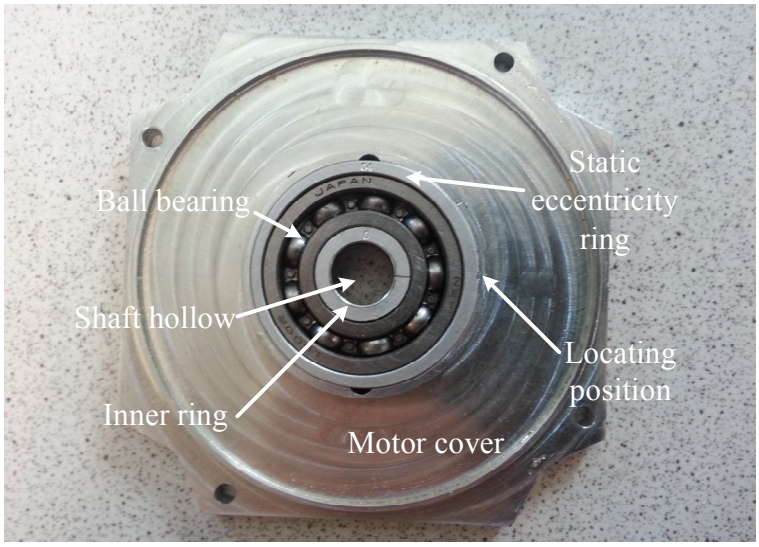

Figure 7.11: Prototype of structure design to simulate motor SUMP fault

7.3.2 Experimental results and discussion for SUMP

As with the testing procedure for monitoring the ME fault, the vibration data in time domain is collected first. Next, using FT technologies, the vibration data are used to generate a waterfall plot in the frequency domain under different motor running speeds. The motor largest vibration amplitudes under 3000 RPM are extracted and shown in Table 7.4. Compared to other field data in Table 7.4, the data in the field at 500Hz in the *y* and *z* directions increase with SE fault grades. This is expected as the 500 Hz components are the diagnostic features of the SE fault.

Table 7.4: Experimental results induced by SUMP with different grades of SE faults

Faulty grades	x (m/s)				y (m/s)				z (m/s)			
	50Hz	500Hz	550Hz	3000Hz	50Hz	500Hz	550Hz	3000Hz	50Hz	500Hz	550Hz	3000Hz
e0	0.016600	0.205200	0.024460	0.018980	0.028980	**0.161200**	0.022170	0.018480	0.034770	**0.193500**	0.026480	0.022180
e1	0.016622	0.205255	0.024504	0.019021	0.028991	**0.161657**	0.022212	0.018514	0.034798	**0.194342**	0.026505	0.022202
e2	0.016626	0.205217	0.024473	0.019011	0.029006	**0.162148**	0.022205	0.018507	0.034803	**0.195244**	0.026529	0.022200
e3	0.016628	0.205231	0.024509	0.019033	0.029002	**0.162625**	0.022210	0.018501	0.034810	**0.196455**	0.026508	0.022214
e4	0.016625	0.205216	0.024479	0.019038	0.029002	**0.163222**	0.022209	0.018516	0.034804	**0.198356**	0.026508	0.022226

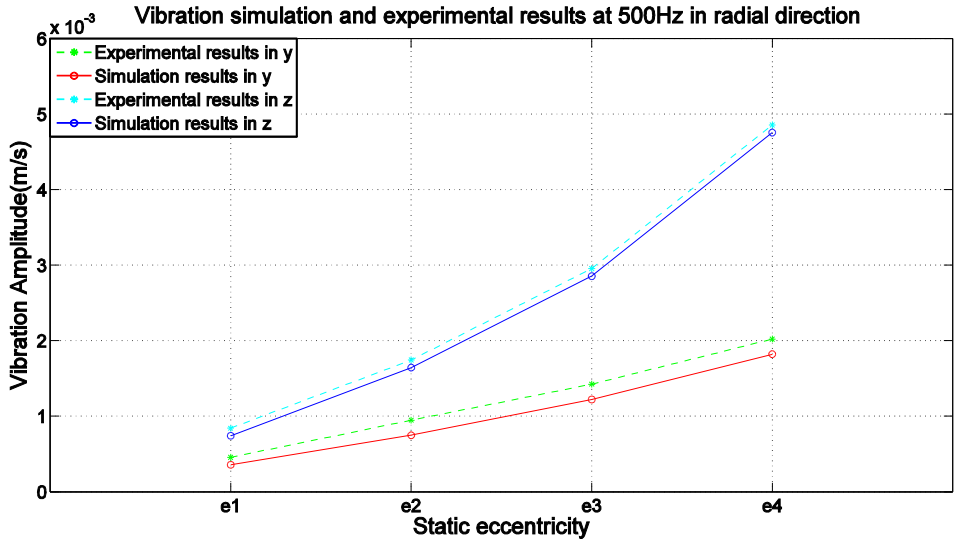

Figure 7.12: Comparison between the experimental and simulation results with 4 faulty grades of SE faults at 3000 RPM

Figure 7.12 compares the simulation results obtained in Chapter 6 to the experimental results in Table 7.4. It can be observed that the experimental results tally with the simulation results when the motor has different grades of SE faults and set operating at 3000 RPM. Moreover, both results show that the vibration responses increase with SE fault grades. Therefore, the 500 Hz frequency components in the radial direction can be utilized as the diagnostic features for the SE fault.

7.4 Dynamical responses of Dynamic Unbalanced Magnetic Pull

7.4.1. Experimental design for Dynamic Unbalanced Magnetic Pull

The Dynamic Unbalanced Magnetic Pull (DUMP) is generated by the motor's rotor dynamic eccentricity (DE) fault. DE fault can be simulated by attaching an eccentricity ring between the ball bearing and the motor shaft. The dynamic ring design and prototype with different dynamic eccentricity grades are illustrated in Figures 7.13 and 7.14.

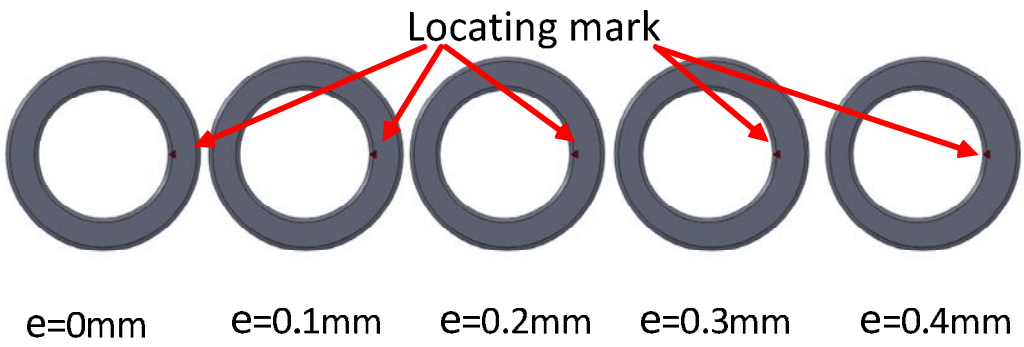

Figure 7.13: DE rings with 4 faulty grades structures

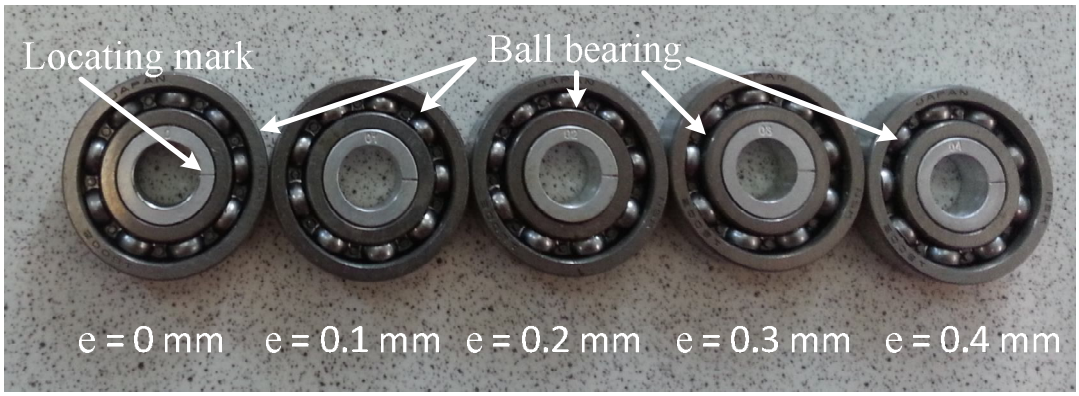

Figure 7.14: Prototype of DE rings with 4 faulty grades structures

The function of the locating mark on the eccentricity ring is to align the datum line marked on the rotor shaft; see Figures 7.15 and 7.16. Therefore, the datum lines at both sides should be fine and collinear with each other to confirm the dynamic eccentricity at both sides in the same phase.

In order to reuse the bearing and bearing cover, an even SE ring with e = 0 mm, which as shown in Figure 7.9 is also fitted between the bearing and bearing cover as demonstrated in Figure 7.17. The prototype with DE fault is shown in Figure 7.18.

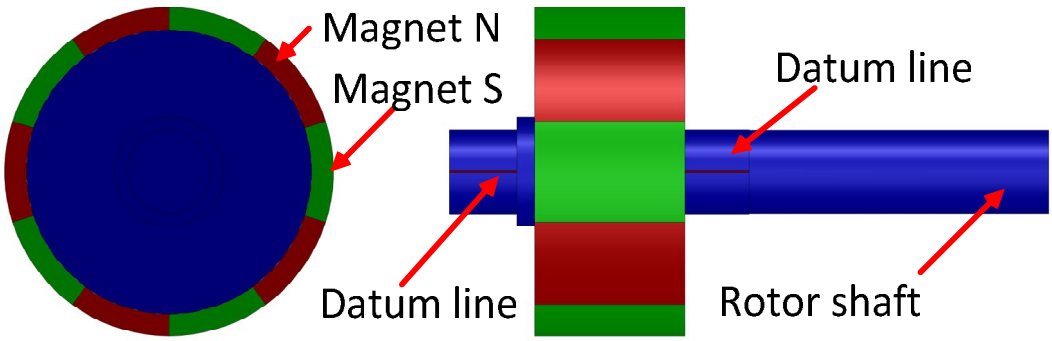

Figure 7.15: Rotor structure with datum line on rotor shaft

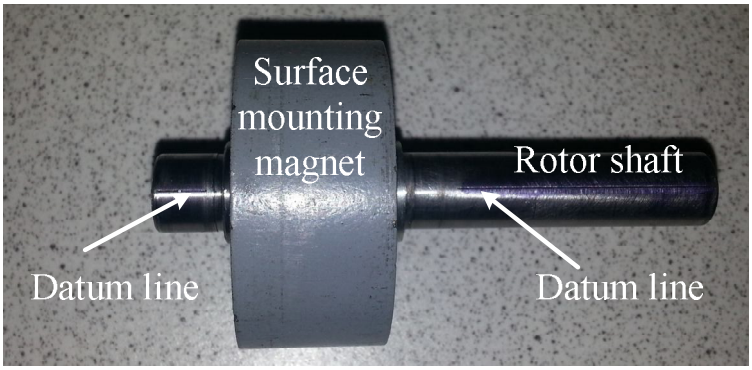

Figure 7.16: Prototype of rotor structure with datum line on rotor shaft

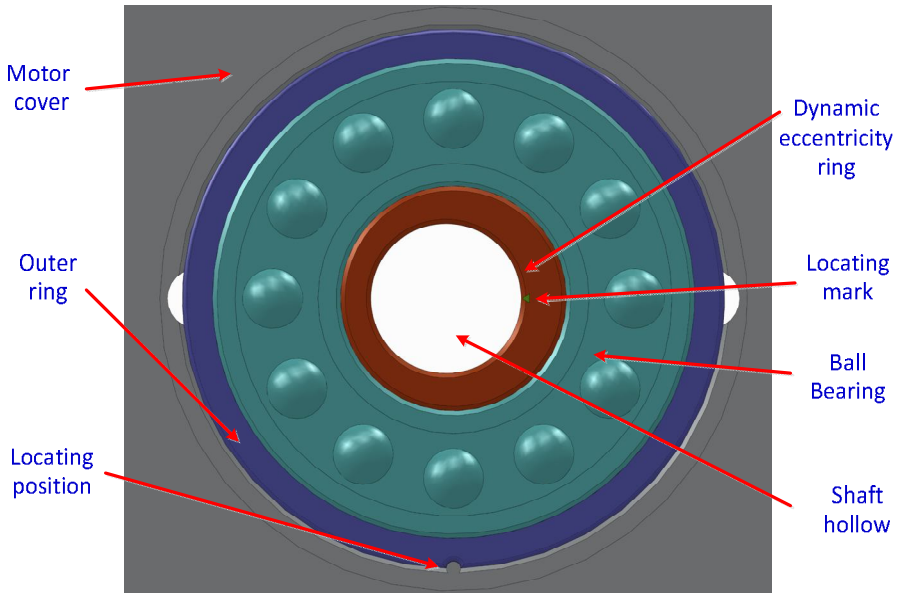

Figure 7.17: Structure design to simulate motor DUMP fault

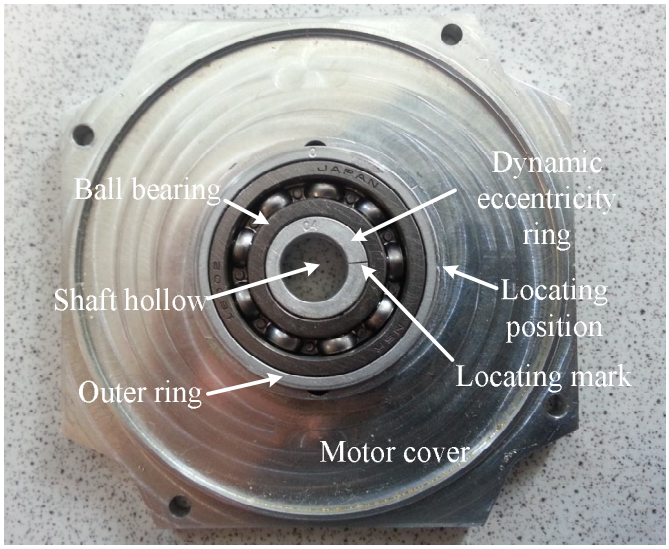

Figure 7.18: Prototype of structure design to simulate motor DUMP fault

7.4.2 Experimental results and discussion for DUMP

After the motor with dynamic eccentricity ring is assembled on the testing bench shown in Figure 7.7, the PMSM is driven up to 3000 RPM. Using the same approach, the experimental results of the PMSM with different grades of DE faulty are obtained and listed in Table 7.5. It can be observed that other than the MU and SE faults, the two columns of field data (at 50Hz and 550Hz in y and z) increase obviously with increasing DE grades in the y and z directions.

Table 7.5: Experimental results induced by DUMP with different grades of DE faults

Faulty grades	x (m/s)				y (m/s)				z (m/s)			
	50Hz	500Hz	550Hz	3000Hz	50Hz	500Hz	550Hz	3000Hz	50Hz	500Hz	550Hz	3000Hz
e0	0.016600	0.205200	0.024460	0.018980	**0.028980**	0.161200	**0.022170**	0.018480	**0.034770**	0.193500	**0.026480**	0.022180
e1	0.016639	0.205237	0.024496	0.019026	**0.030511**	0.161242	**0.023701**	0.018507	**0.034790**	0.038013	**0.029723**	0.022201
e2	0.016643	0.205217	0.024480	0.018995	**0.031675**	0.161222	**0.024865**	0.018528	**0.034797**	0.041140	**0.032850**	0.022212
e3	0.016605	0.205220	0.024474	0.018997	**0.033013**	0.161217	**0.026203**	0.018519	**0.034814**	0.044440	**0.036150**	0.022226
e4	0.016628	0.205238	0.024498	0.018995	**0.034479**	0.161229	**0.027669**	0.018509	**0.034815**	0.048080	**0.039790**	0.022211

Figure 7.19 compares the experimental and simulation results of 50 Hz signal in the PMSM with different grades of DE faults. The former tally with the latter as both

increase with the DE grade in the y and z directions. The experimental and the simulation results of 550 Hz signal are compared in Figure 7.20. Although the similar trends are observed as in Figure 7.19, 550 Hz is the second most dominant component in the DUMP faulty motor and it is smaller than 50 Hz signal. However, in order to distinguish DE faulty motor from ME faulty motor, 50 Hz and 550 Hz signals should be used as the diagnostic features for DE fault.

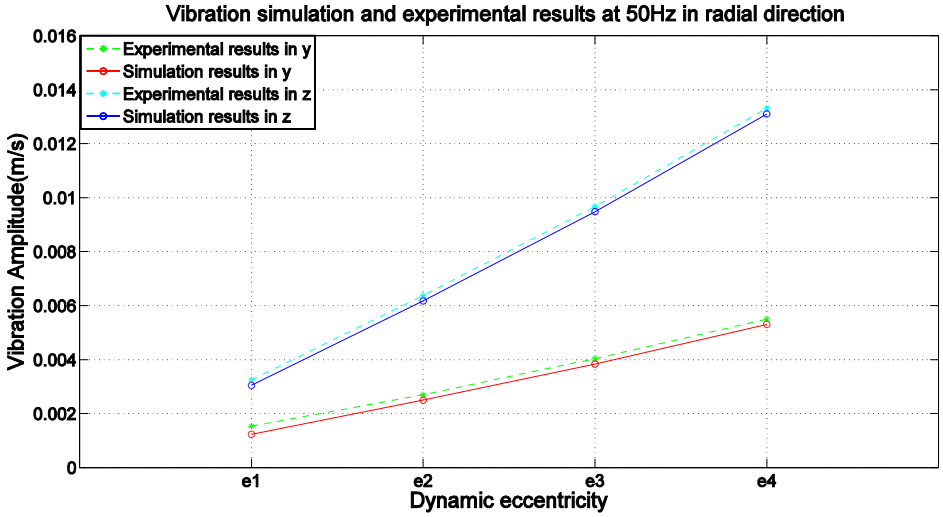

Figure 7.19: Comparison between the experimental and simulation results with 4 faulty grades of DE faults at 50 Hz

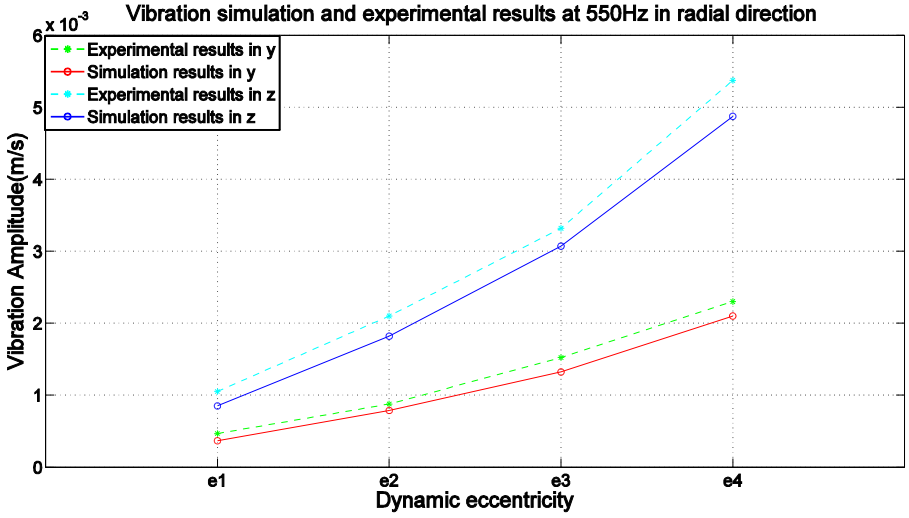

Figure 7.20: Comparison between the experimental and simulation results with 4 faulty grades of DE faults at 550 Hz

7.5 Dynamic responses of Inclined Unbalanced Magnetic Pull

7.5.1 Experimental design for Inclined Unbalanced Magnetic Pull

Inclined Unbalanced Magnetic Pull (IUMP) is generated due to the radial direction Inclined Eccentricity (IE) fault, whereby one side of the rotor is generally offset downward from the stator center, while the other side of the rotor is offset upward from the stator center as shown in Figure 7.21.

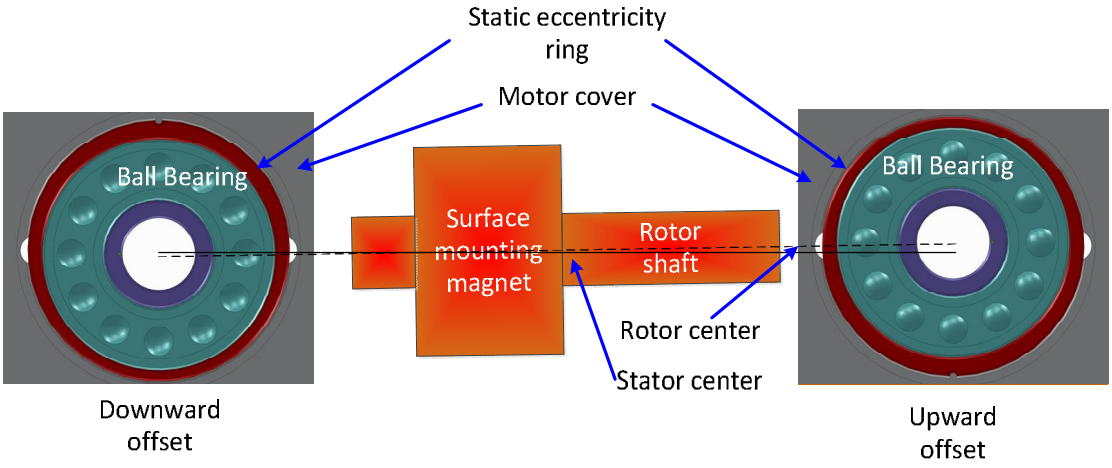

Figure 7.21: Structure design to simulate motor IUMP fault

7.5.2 Experimental results and discussion for IUMP

The experimental data with different IUMP faulty grades are listed in Table 7.6. Figure 7.22 compares the experimental and simulation results of the PMSM with different grades of IE faults. It can be observed that, both in the simulation and experimental results, the vibration amplitudes of 500 Hz in the x direction is larger than those in the y and z directions, though the x component of the IUMP is smaller than the ones in the y and z directions. This is because the stiffness of the preload washer of the bearing is much lower than that of the ball bearing in the radial

direction. Therefore, 500 Hz components in x, y, and z directions could be used to distinguish IE fault from SE fault and as the IE diagnostic features.

Table 7.6: Experimental results induced by IUMP with different grades of IE faults

Fault grades	x (m/s)				y (m/s)				z (m/s)			
	50Hz	500Hz	550Hz	3000Hz	50Hz	500Hz	550Hz	3000Hz	50Hz	500Hz	550Hz	3000Hz
e0	0.016600	**0.205200**	0.024460	0.018980	0.028980	**0.161200**	0.022170	0.018480	0.034770	**0.193500**	0.026480	0.022180
e1	0.016635	**0.205948**	0.024486	0.019016	0.029009	**0.161429**	0.022194	0.018504	0.034789	**0.193866**	0.026503	0.022203
e2	0.016627	**0.209270**	0.024492	0.019013	0.029003	**0.161625**	0.022205	0.018510	0.034810	**0.194233**	0.026507	0.022201
e3	0.016634	**0.214970**	0.024482	0.019014	0.029013	**0.161861**	0.022200	0.018537	0.034803	**0.195034**	0.026495	0.022206
e4	0.016629	**0.227510**	0.024477	0.019001	0.029034	**0.162219**	0.022200	0.018499	0.034807	**0.196220**	0.026501	0.022201

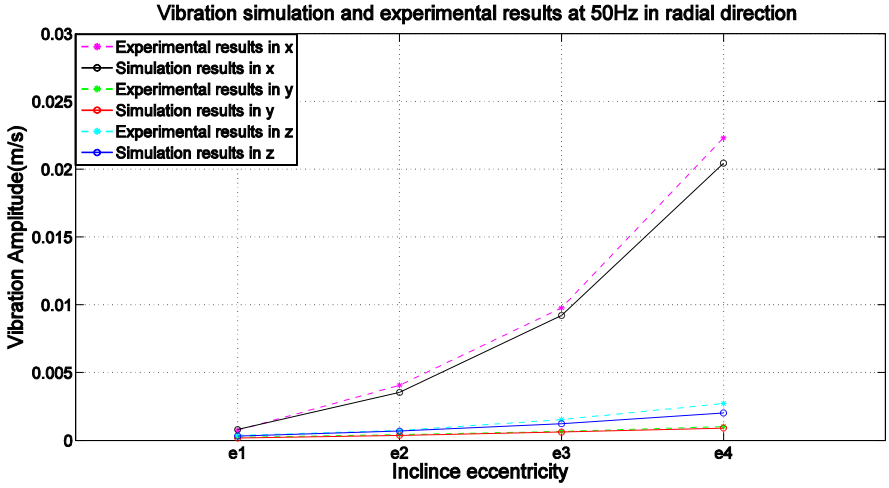

Figure 7.22: Comparison between the experimental and simulation results with 4 faulty grades of IE faults at 500Hz

7.6 Dynamical responses of Axial Unbalanced Magnetic Pull

7.6.1 Experimental design for Axial Unbalanced Magnetic Pull

Axial Unbalanced Magnetic Pull (AUMP) is generated by the rotor axial eccentricity (AE) fault due to the unaligned stator and rotor cores in the axial direction. This type of UMP always exists in motors with Hall sensors. This is because, in order to detect the rotor's magnetic field, the rotor core is longer than the stator core at the

hall sensor side. In order to eliminate the free movement of the rotor shaft between the two support bearings, the preload spring washer is always added.

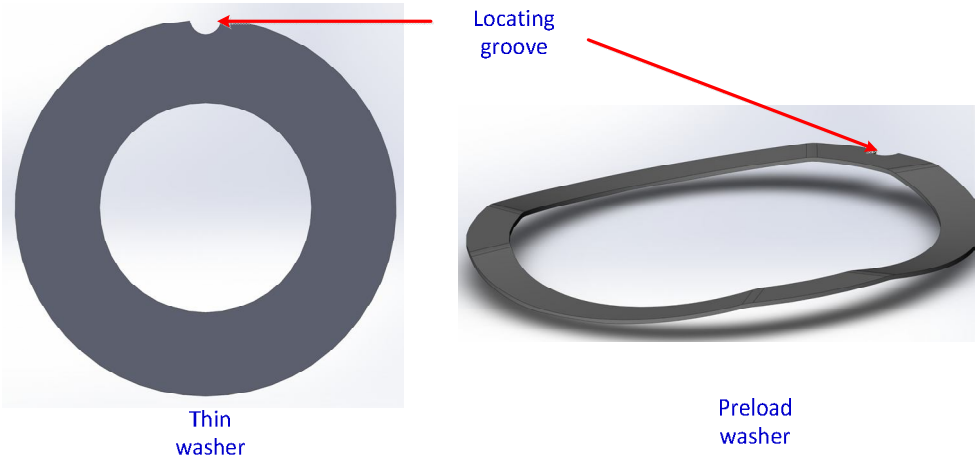

Figure 7.23: Thin washer and bearing preload washer

Figure 7.24: Prototype of Thin washer and bearing preload washer

In order to simulate the AUMP, twenty pieces of thin washer of 0.1mm thickness and one piece of preload washer were made; the design and prototype of the washers are shown in Figures 7.23 and 7.24. The function of the locating hole is to prevent the washer from rotating in the bearing cavity, which generates additional vibration and acoustic noise.

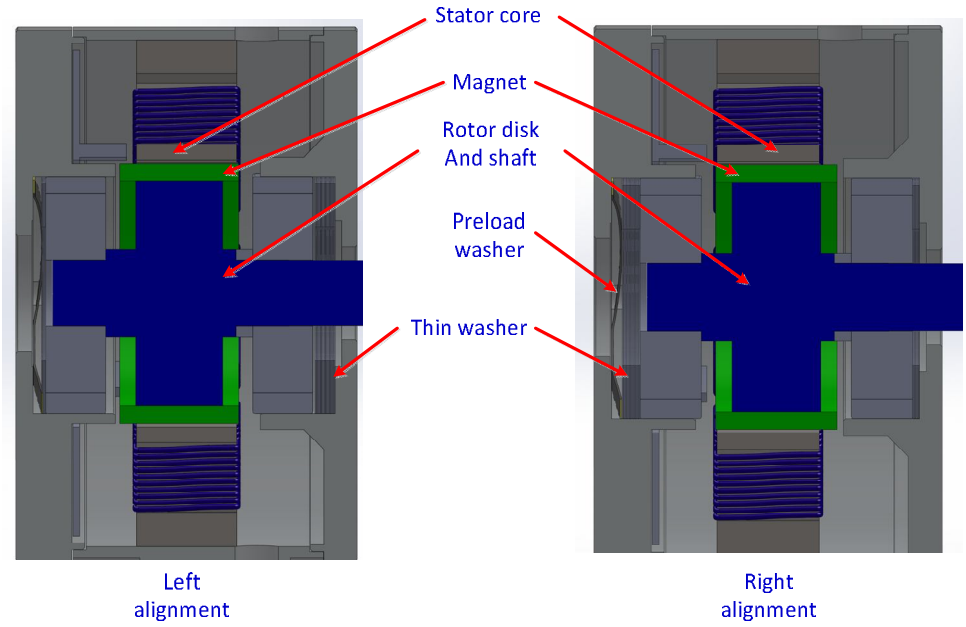

Figure 7.25: Structure design to simulate motor AUMP fault

Figure 7.25 shows the experimental setup to simulate the rotor axial eccentricity (AE) fault. After pieces of thin washer were reduced at the bearing preload washer side and the same amount of thin washer was added at the opposite side, the motor had axial left alignment fault and AUMP, which pointed to the right was generated. On the other hand, if the pieces of thin washer were added at the bearing preload washer side and the same amount of thin washer was reduced at the opposite side, the motor had axial right alignment fault and AUMP, which pointed to the left, was generated.

7.6.2 Experimental results and discussion for AUMP

The experimental results with different grades of AE faults are shown in Table 7.7. Although the amplitudes in the x direction at 3000 Hz are smaller than those at

500Hz in the x, y and z directions, the changes of the former are bigger than those of the latter.

Table 7.7: Experimental results induced by AUMP with different grades of AE faults

Fault grades	x (m/s)				y (m/s)				z (m/s)			
	50Hz	500Hz	550Hz	3000Hz	50Hz	500Hz	550Hz	3000Hz	50Hz	500Hz	550Hz	3000Hz
e0	0.016600	0.205200	0.024460	**0.018980**	0.028980	0.161200	0.022170	0.018480	0.034770	0.193500	0.026480	0.022180
e1	0.016622	0.205255	0.024504	**0.028925**	0.028991	0.161231	0.022212	0.018514	0.034798	0.193533	0.026505	0.022202
e2	0.016626	0.205217	0.024473	**0.039770**	0.029006	0.161251	0.022205	0.018507	0.034803	0.193531	0.026529	0.022200
e3	0.016628	0.205231	0.024509	**0.058460**	0.029002	0.161223	0.022210	0.018501	0.034810	0.193522	0.026508	0.022214
e4	0.016625	0.205216	0.024479	**0.097040**	0.029002	0.161227	0.022209	0.018516	0.034804	0.193538	0.026508	0.022226

Figure 7.26 compares the experimental and simulation results at 3000 Hz in the x direction. It can be observed that the experimental results with different eccentricity grades are well matched with the simulation results of the same grades faults. Although the AUMP is small, the vibration in the x direction significantly increases with the AE grades because the stiffness of the preload is the lowest in the radial and axial directions. Therefore, that vibration signals at 3000 Hz in the x direction could be utilized as the diagnostic feature for AE fault.

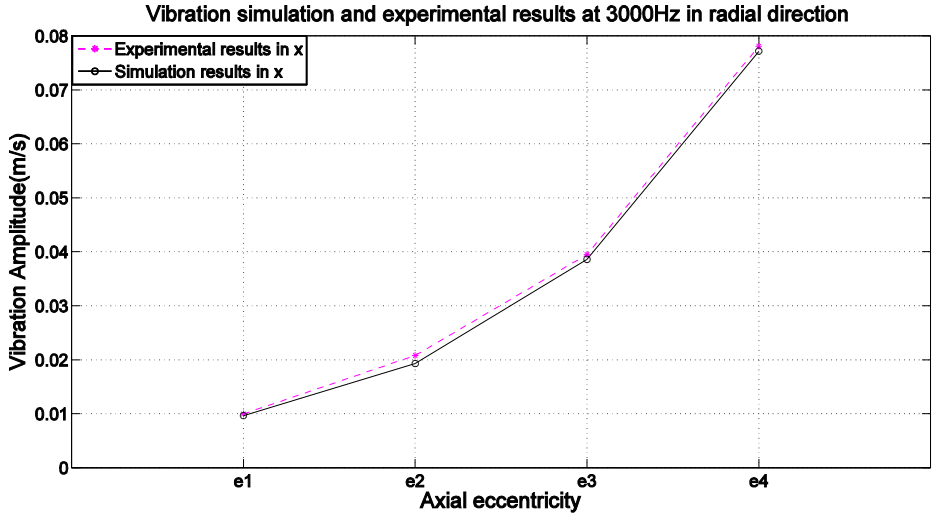

Figure 7.26: Comparison between the experimental and simulation results with 4 faulty grades of AE faults at 3000 Hz

7.7 Conclusions

In this chapter, the experimental fault diagnostic platform is presented, including the anti-vibration table, the Laser Doppler velocimetry (LDV), the modified PMSM with different types of faults, the motor speed control algorithm and the signal measurement algorithm.

Faulty motors with Mechanical Eccentricity (ME), Static Eccentricity (SE), Dynamic Eccentricity (DE), Inclined eccentricity (IE) and Axial eccentricity (AE) are designed and prototyped. The frequency domain vibration signals with waterfalls are used to extract optimized motor running speed and the diagnostic features of each type of faults.

Additional mass is attached to a MU disk to simulate the ME faults. 50 Hz signals are the dominant vibration frequency in the radial direction, and this phenomena is confirmed both in the experimental and numerical simulation results. An SE ring is designed and made to simulate the motor SE fault, and is attached between the motor's end cover and the outer surface of the bearing. 500 Hz signals are the dominant signals in the waterfall. The increasing trends of the experimental results are the same as that of the simulation results with SE faults. A DE ring is designed and made to simulate the motor DE fault, and is attached between the inner surface of the bearing and the rotor shaft. The vibration components at 50 Hz and 550 Hz frequencies are dominant in the radial direction, which are matched well with the simulation and analytical results. To simulate the IE fault, an SE ring is attached upward on one side and the other SE ring is attached downward on the other side. Although the faulty frequency is the same as that of the SE in the radial direction, there is an additional 500 Hz component in the axial direction. Therefore, the IE fault

can be distinguished from the SE fault using this additional diagnostic feature. These experimental results tally well with the simulation results. A group of thin disk-type washers are attached between the motor cover and the bearing in the axial direction to simulate the AE faults. Increasing or decreasing the number of the thin washers can be used to simulate different grades of AE faults. The dominant frequency of the AE is 3000 Hz. As with aforementioned faults, these experimental results of the dominant frequency component also tally well with the simulation results.

In this chapter, the ME fault and four types of UMPs-related fault experimental data are collected and studied. These five types of motor faulty vibration signals obtained by experiment tally with the predicted results in the previous chapter. When the motor has a 10-pole and 12-slot structure, p is 10, the Least Common Multiple (LCM) of the rotor pole number and stator slot number is 60. The experimental studies in this chapter further demonstrate that $1\times$, $p\times$, $(p+1)\times$ and $LCM\times$ order are the effective frequency which can be employed to distinguish different types of rotor eccentricity faults. The experimental results also show that the faulty frequencies of vibration signals are the same as UMPs. Therefore, the UMPs induced vibration can be used to diagnose UMPs-related eccentricity faults, instead of measuring the UMPs. Moreover, the faulty frequencies of vibration signal can be used to distinguish MU fault from UMPs related faults.

CHAPTER 8

CONCLUSIONS AND FUTURE WORKS

8.1 Conclusions

The purpose of this research is to advance the field of electromagnetic analysis and diagnosis in the Permanent Magnet Synchronous Motors (PMSMs). Due to its advantages, the PMSM is witnessing fast-growing use in normal applications and critical applications. In areas of critical applications, such as power stations, aerospace, transport systems, and healthcare systems, the reliability of the motor is very important, and the motor needs to be constantly monitored, and any problems quickly diagnosed. PMSM electrical faults are not covered in this dissertation as it can be easily detected by a motor current signals. The research focuses on the diagnosis of mechanical and electromagnetic faults related to the PMSM.

A. Dynamic structure studies

In order to study the mechanical dynamic characteristics in detail, dynamic structure models of the PMSM have been built using the lumped mass method. The dynamic models of the rotor mounted on fixed and flexible supports are built with gyroscopic effects. The stator teeth and stator core are modeled, respectively, as a cantilever beam and a hollow cylinder. The frequencies of the motor mounting

foundation are studied using a mass-spring-damping system. The main contributions of this research are:

(1) Mathematical models have been developed;

(2) parametric studies of the dynamic structure have been conducted to predict the natural frequencies; and

(3) numerical calculations have been carried out to validate the effectiveness of the proposed mathematical models.

All these mechanical modes are validated with experiment results, and the effectiveness of the modes are thus be confirmed.

B. Vibration excitation forces studies

Besides the MU Mechanical Unbalance (MU) force, there are also different types of Unbalanced Magnetic Pulls (UMPs) acting on the rotor core due to the actions of electromagnetic fields. In this dissertation, a detailed study on the mechanism of the electromagnetic forces developed in the PMSM is presented. The main contributions of this research are:

(1) Analytical models of four types of UMPs have been developed;

(2) parametric studies of the UMPs are conducted to predict the faulty frequencies;

(3) and computer simulations have been carried out to validate the effectiveness of the proposed faulty frequency prediction model.

The effectiveness of all these electromagnetic modes is validated with special designed experiment results.

C. Faulty motor experimental design

To investigate the vibration signals in various motor fault conditions, and verify the mechanical and electromagnetic modes developed, the faulty motors have been designed and tested with carefully devised experimental programs. The experimental platform developed can realize and control the faulty conditions of the PMSM, and can thus be used to verify effectively the validity of the analytic fault prediction models developed.

D. Motor other fault studies

The aforementioned faults can be defined as the motor inner faults. Besides these faults, the motor may have other faults such as loose grounding and cooling fan faults (refer to Appendix B). The blade of the cooling fan may experience fatigue cracks due to the air-flow excitation forces. The first bending mode frequency decreases with crack size, because the first bending stiffness of the blade also decreases with crack size. However, difference from the MU and UMPs-related faults, the blade crack faulty frequency is independent on the motor rotating speed; therefore, the blade crack fault can be distinguished from aforementioned faults by changing the motor running speed.

8.2 Future Works

With the accomplishment of the experimental platform to validate the analytical and simulated models, it can be envisioned that the approach can be extended to diagnose other types of faults in PMSM or other types of motor. Utilizing the analysis methods presented, more effective approaches can be further developed to handle these new challenges.

- Diagnose with other sensors

In the real application of PMSM, LDV may be difficult to be used in the fault detection, We will develop a new algorithm with other types of sensors, such as piezoelectric (PZT), accelerometer sensor, to diagnose cracked rotor. However, To develop a new approach to firmly mount them on the motor is a new challenge.

- Diagnose uniform and partial demagnetization fault in PMSM

PMSMs are using the high energy magnet, like NdFeB and SmCo, and motor power range has been increased in these years. The motor/generator performance is thus sensitive to the magnet status. With the accomplishment in the fault diagnosis for PMSM, the model for analysing the uniform demagnetization (UD) and partial demagnetization (PD) can also be built, and the fault diagnosis approaches can also be developed.

- Diagnose of other types motors

Following the fast development of electric machines, materials and production technologies, many new types of electrical machines will enter market in the coming years, and the electric machine diagnosis will become more and more important. With the accomplishment of the experimental platform to validate the analytical and

simulated models, it can be envisioned that the approach can be extended to diagnose other types of faults in electric machines, e.g., switched reluctance motor (SRM), can also be developed.

APPENDIX A

IUMP TOTAL FORCE AND ACTION POSITION

In order to calculate the Inclined Unbalanced Magnetic Pull (IUMP) correctly, the stator is divided into 10 segments in the axis direction; in the radial direction, each section is divided into 4 sections.

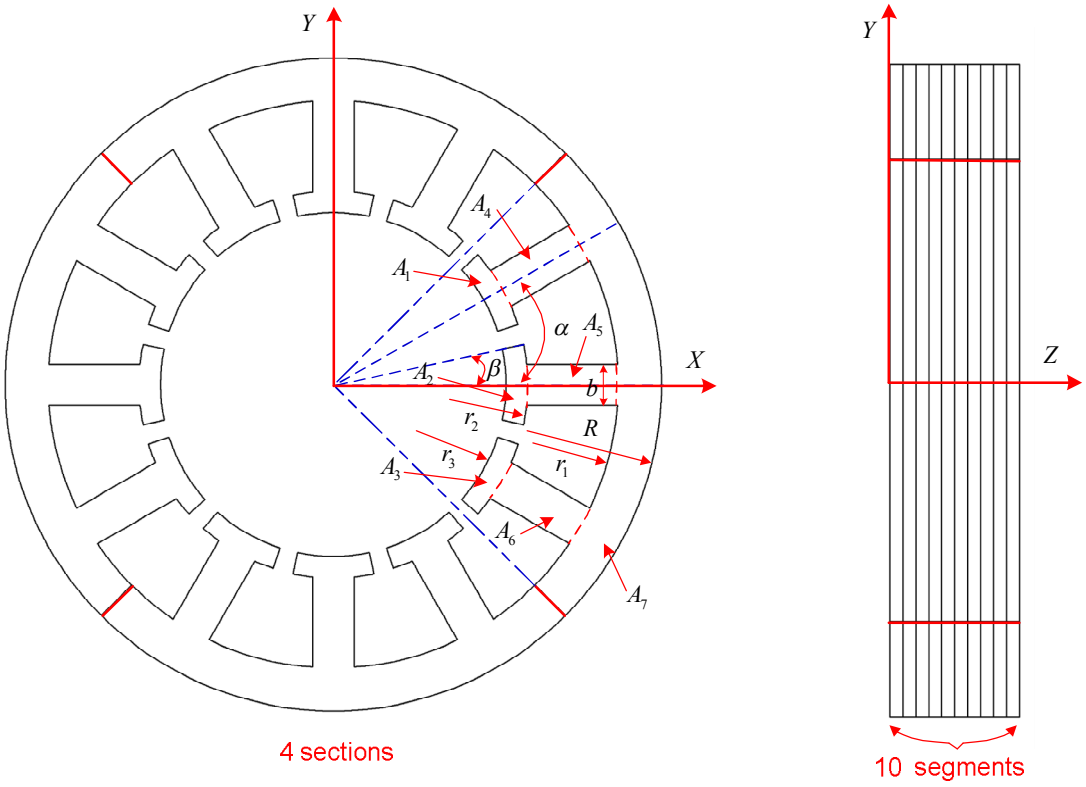

Figure A.1: Divided sections and segments of the stator core for IUMP calculation

The divided stator core is shown Figure A.1. The individual stator segments are assumed to be symmetrical, and therefore only a geometrical center of one segment

needs to be calculated, as those of the other three can be calculated based on the results of the first geometry.

In Figure A.1, it is known that the y coordinate of the geometrical center of these segments is zero because the geometry center is also symmetrical in the y direction. This segment is also divided into seven areas, A_1, A_2,...A_7, and the x coordinates of their geometry centers are calculated. The x coordinate of the whole segment can then be obtained. The x coordinate of the geometry center can be calculated by:

$$C_x = \frac{\int x \cdot y(x) d_x}{\int y(x) d_x} \quad \text{(A.1)}$$

In Figure A.1, R=38mm; r_1=33mm; r_2=22.5mm; r_3=20mm; b=4.8mm; α=30°; β=11°. With reference to equation (A.1) and Figure A.1, the x coordinates C_{x2}, C_{x5},... C_{x7} of A_{x2}, A_{x5},... A_{x7} can be calculated as:

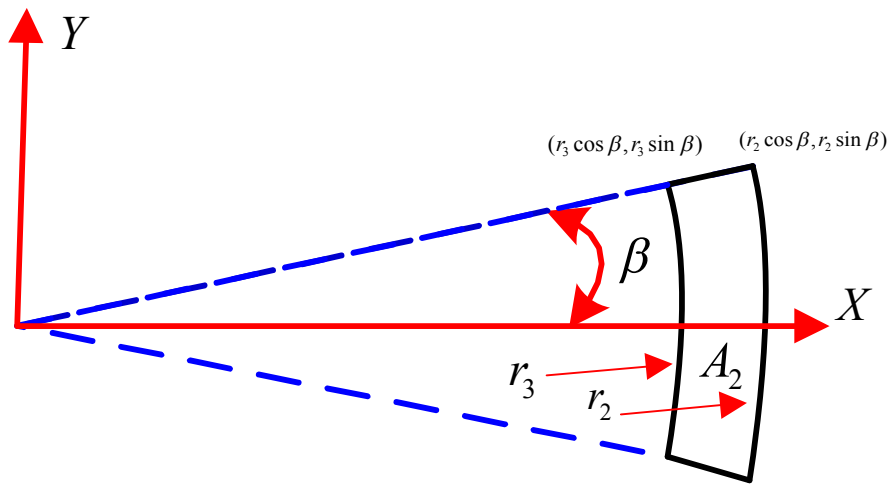

Figure A.2: Geometry of area A2 in Figure A.1

Based on the shape in Figure A.2 , the geometry center C_{x2} can be expressed as:

$$C_{x2}=\frac{2\int_{r_3\cos[\beta]}^{r_3}x(x\cdot tg[\beta]-\sqrt{r_3^2-x^2})d_x+\int_{r_3}^{r_2\cos[\beta]}x(x\cdot tg[\beta])d_x]+\int_{r_2\cos[\beta]}^{r_2}x(\sqrt{r_2^2-x^2})d_x]}{2[\int_{r_3\cos[\beta]}^{r_3}(x\cdot tg[\beta]-\sqrt{r_3^2-x^2})d_x+\int_{r_3}^{r_2\cos[\beta]}(x\cdot tg[\beta])d_x]+\int_{r_2\cos[\beta]}^{r_2}(\sqrt{r_2^2-x^2})d_x]} \quad (A.2)$$

In order to simplify equation.(A.2), we can separate the numerator and denominator of C_{x2} and it can be described as:

$$\begin{cases} num=\int_{r_3\cos[\beta]}^{r_3}x(x\cdot tg[\beta]-\sqrt{r_3^2-x^2})d_x+\int_{r_3}^{r_2\cos[\beta]}x(x\cdot tg[\beta])d_x]+\int_{r_2\cos[\beta]}^{r_2}x(\sqrt{r_2^2-x^2})d_x \\ den=\int_{r_3\cos[\beta]}^{r_3}(x\cdot tg[\beta]-\sqrt{r_3^2-x^2})d_x+\int_{r_3}^{r_2\cos[\beta]}(x\cdot tg[\beta])d_x]+\int_{r_2\cos[\beta]}^{r_2}(\sqrt{r_2^2-x^2})d_x \end{cases} .(A.3)$$

So,

$$num=tg[\beta](\frac{r_3^3(1-\cos^3[\beta])}{3})-\frac{1}{3}(r_3^2-r_3^2Cos[\beta]^2)^{3/2}+tg[\beta](-\frac{r_3^3}{3}+\frac{r_2Cos[\beta]^3}{3})+\frac{1}{3}(r_2\sin[\beta])^3, \quad (A.4)$$

and

$$den=\frac{11}{360}\pi(r_2^2-r_3^2) \ . \quad (A.5)$$

As it is known that r_2=22.5mm, r_3=20mm, and β=11°, num in equation (A.4) and den in equation (A.5) can be calculated as:

$$num=215.65(mm^2) \quad (A.6)$$

and

$$den=10.2(mm) \quad (A.7)$$

C_{x2} can be obtained by dividing equation (A.6) by equation :

$$C_{x2}=\frac{num}{den}=21.14(mm) \quad (A.8)$$

The shape of A_5 can simply be considered a rectangle, and C_{x5} can be calculated by:

$$C_{x5}=\frac{r_1+r_2}{2}=27.75(mm) \quad (A.9)$$

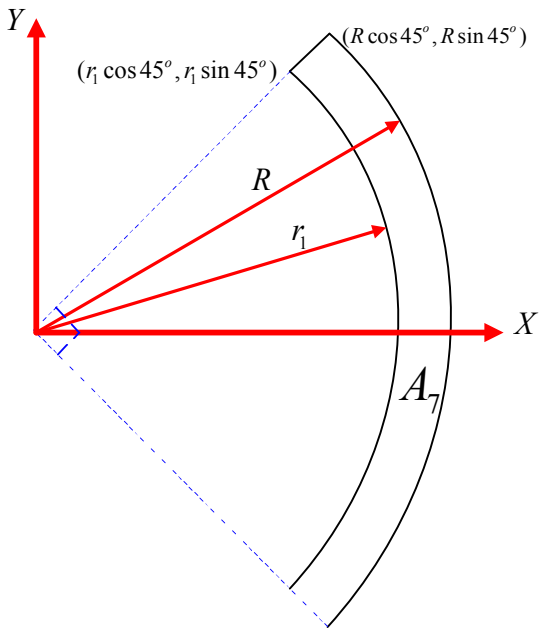

Figure A.3 : Geometry of A7 in Figure A.1

Figure A.3 shows the geometry of $A7$; based on the shape, the geometry center C_{x7} can be expressed as:

$$C_{x7}=\frac{2[\int_{r_1\cos 45^\circ}^{R\cos 45^\circ} x(x\cdot tg45^\circ-\sqrt{r_1^2-x^2})d_x+\int_{R\cos 45^\circ}^{r_1} x(\sqrt{R^2-x^2}-\sqrt{r_1^2-x^2})d_x+\int_{r_1}^{R} x(\sqrt{R^2-x^2})d_x]}{2[\int_{r_1\cos 45^\circ}^{R\cos 45^\circ} (x\cdot tg45^\circ-\sqrt{r_1^2-x^2})d_x+\int_{R\cos 45^\circ}^{r_1} (\sqrt{R^2-x^2}-\sqrt{r_1^2-x^2})d_x+\int_{r_1}^{R} (\sqrt{R^2-x^2})d_x]} \quad \text{(A.10)}$$

In order to simplify equation (A.10), the numerator and denominator of C_{x7} are separated:

$$\begin{cases} num=\int_{r_1\cos 45^\circ}^{R\cos 45^\circ} x(x\cdot tg45^\circ-\sqrt{r_1^2-x^2})d_x+\int_{R\cos 45^\circ}^{r_1} x(\sqrt{R^2-x^2}-\sqrt{r_1^2-x^2})d_x+\int_{r_1}^{R} x(\sqrt{R^2-x^2})d_x \\ den=\int_{r_1\cos 45^\circ}^{R\cos 45^\circ} (x\cdot tg45^\circ-\sqrt{r_1^2-x^2})d_x+\int_{R\cos 45^\circ}^{r_1} (\sqrt{R^2-x^2}-\sqrt{r_1^2-x^2})d_x+\int_{r_1}^{R} (\sqrt{R^2-x^2})d_x \end{cases} \quad \text{(A.11)}$$

After calculation and integration, “num” and “den” can be simplified as:

$$num=\frac{R^3-r_1^3}{3\sqrt{2}} \quad , \quad \text{(A.12)}$$

and

$$den = \frac{1}{8}\pi R^2 - \frac{1}{8}\pi (r_1)^2 \quad . \tag{A.13}$$

As it is known that R=38mm and r_1=33mm, "num" of equation (A.12) and "den" in equation (A.13) can be obtained as:

$$num = 4463 \quad , \tag{A.14}$$

and

$$den = 139.4 \quad . \tag{A.15}$$

Therefore, C_{x7} can be calculated by:

$$C_{x7} = \frac{num}{den} = \frac{4463}{139.14} = 32.075(mm) \tag{A.16}$$

Due to the symmetrical structure of the stator core in the motor (refer to Figure A.1), C_{x1}, C_{x3}, C_{x4}, and C_{x6} can be simply calculated by:

$$\begin{aligned} C_{x1} &= C_{x3} & C_{x4} &= C_{x6} \\ &= C_{x2}\cos\alpha & &= C_{x5}\cos\alpha \\ &= 21.14\times\cos 30^\circ & &= 27.75\times\cos 30^\circ \\ &= 18.308(mm) & &= 24.03(mm) \end{aligned} \tag{A.17}$$

So the geometry center of the section A in one segment can be calculated by:

$$C_x = \frac{A_1C_{x1} + A_2C_{x2} + A_3C_{x3} + A_4C_{x4} + A_5C_{x5} + A_6C_{x6} + A_7C_{x7}}{A_1 + A_2 + A_3 + A_4 + A_5 + A_6 + A_7} \tag{A.18}$$

Inputting the geometry values generates

$$C_x = 28.383(mm) \tag{A.19}$$

The IUMP in each segment of one section is assumed to apply to the center of the geometry of A, B, C, and D. The coordinates of the four points are (28.383,0), (0,28.383), (-28.383,0), and (0,-28.383) respectively. Based on the centers of these

four points and the calculated force which is applied to these four points, the applied point of the IUMP can be calculated.

Figure A.4 shows the coordinates of these four points. IUMPs that are assumed to apply to A, B, C, and D are (F_{Ax}, F_{Ay}), (F_{Bx}, F_{By}), (F_{Cx}, F_{Cy}), (F_{Dx},F_{Dy}), and the coordinates of A, B, C, and D are (X_A, Y_A), (X_B, Y_B), (X_C, Y_C), and (X_D, Y_D); based on this the coordinates of the point which the total IUMP is applied to are:

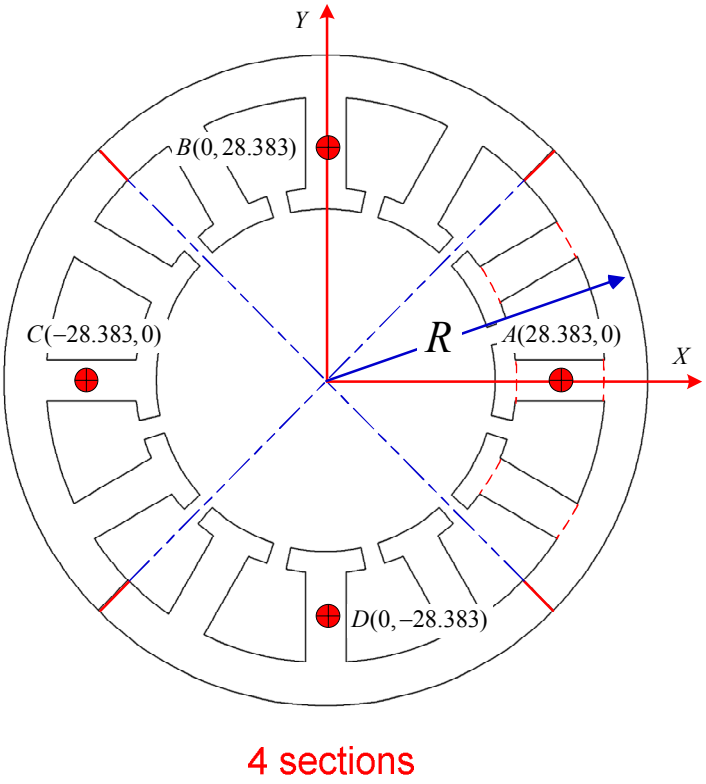

Figure A.4: Geometry centers of each section on one segment of stator

$$\begin{cases} X_{o'} = \dfrac{F_{Ax}X_A + F_{Bx}X_B + F_{Cx}X_C + F_{Dx}X_D}{F_{Ax} + F_{Bx} + F_{Cx} + F_{Dx}} \\ Y_{o'} = \dfrac{F_{Ay}Y_A + F_{By}Y_B + F_{Cy}Y_C + F_{Dy}Y_D}{F_{Ay} + F_{By} + F_{Cy} + F_{Dy}} \end{cases}, \tag{A.20}$$

equation (A.20) can be simplified by applying the coordinates of A, B, C, D:

$$\begin{cases} X_{o'} = \dfrac{28.383 \times (F_{Cx} - F_{Ax})}{F_{Ax} + F_{Bx} + F_{Cx} + F_{Dx}} \\ Y_{o'} = \dfrac{28.383 \times (F_{By} - F_{Dy})}{F_{Ay} + F_{By} + F_{Cy} + F_{Dy}} \end{cases} \tag{A.21}$$

and $Z_{O'}$ is the center of each section.

APPENDIX B

LOAD FAULTS IN PMSM

In the previous chapter, a motor fault diagnosis platform is developed to distinguish the healthy motor from faulty motor and classify different types of faulty motor with testing results. But the platform is developed only based on the motor without load fault condition. To ensure the platform is valid with load fault, the motor cracked blade, one common load fault is studied in this chapter.

B.1 Introduction of blades and blade faults

The blade is an important device in many applications, for example, dispensing the motor's inner heat to extend the motor's lifecycle. The blade used for motor cooling is attached to one end of the motor's rotor and rotates at the same running speed as the motor. After the motor has been used for a number of years, a number of cracks may appear at the root of the blade due to degradation of the blade material, or accidents. The cracks in the blade can increase rapidly, and some blades will break if the cracks are invisible and hence cannot be detected in time. Moreover, the motor may also be damaged due to over-heating, or the whole system may break down. This is the main reason a number of researchers study this problem and try to detect this fault at the early stage [45]-[54].

B.2 Numerical simulation approach

Due to the complexity of the blade structure, the blade model rendered as a radial rotating cantilever beam structure is inaccurate if the analytical approach is used [69]. The numerical approach is a better option because the computing cost is significantly reduced and the computing efficient and accuracy are higher. To improve the research efficiency, an electrical fan is used in the analysis. As the structure of the fan is symmetrical, the displacement of the fan can be simplified, using a finite element model, as:

$$\begin{bmatrix} u_r(r,\theta,z,t) \\ u_\vartheta(r,\vartheta,z,t) \\ u_z(r,\vartheta,z,t) \end{bmatrix} = \sum_{n=0}^{\infty} \begin{bmatrix} \cos(n\vartheta) & 0 & 0 \\ 0 & \sin(n\vartheta) & 0 \\ 0 & 0 & \cos(n\vartheta) \end{bmatrix} \begin{bmatrix} u_{rn}^s(r,z,t) \\ u_{\vartheta n}^s(r,z,t) \\ u_{zn}^s(r,z,t) \end{bmatrix}, \quad \text{(B.1)}$$

where r , θ and z are three vectors in spherical coordination. n the circumferential wave-number and s the symmetrical term with respect to θ. For each value of n, the eigen frequencies and mode shapes are obtained with the harmonic beam element.

Finite Element Method (FEM) is used for the modeling and simulation of the fan. In this research, the 3D geometry model is composed to describe the fan blades, electrical motor with slide bearing, and fan frame, as shown in Figure B.1. The FEM model is constructed with hexagonal brick-type elements, and final mesh is applied around crack edges, as shown in Figure B.2. In this research, a wind speed meter is used to measure front and rear side wind speeds when the fan is running at a full speed. The pressure difference between the front and rear sides of the rotating fan can be obtained from the Equation below:

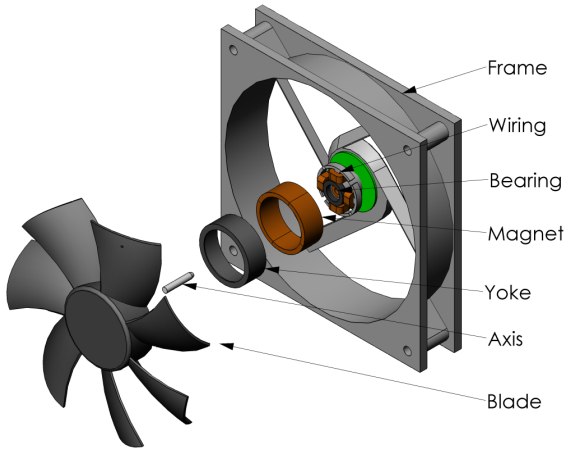

Figure B.1: Radial magnetic field motor with blade

$$\nabla \mathrm{P} = \frac{1}{2}\rho\left(v_1^2 - v_2^2\right), \tag{B.2}$$

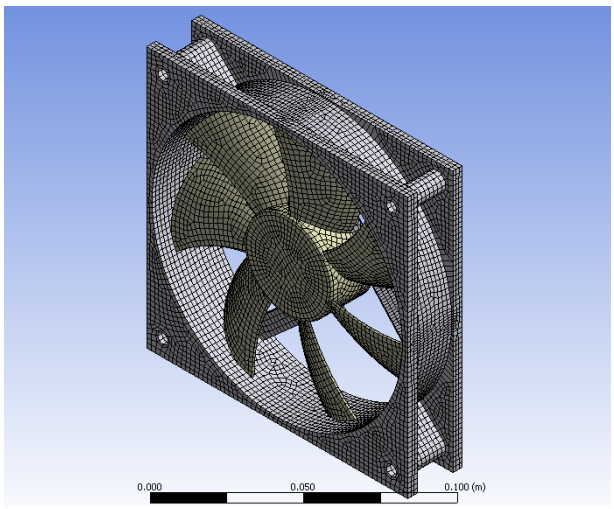

Figure B.2: Finite element model of radial magnetic field motor with blade

where v_1 and v_2 are the speeds of the front and rear sides respectively, and ρ is the density of the air. The air density ρ is 1.237 kg/m^3, and v_1 and v_2 as measured are 3m/s and 1.7m/s respectively. So, based on the above Equation, ∇P is 3.8pa. This pressure will be added to the blade's front surface as an excitation force during the dynamics simulation.

Resonance frequency and amplitude in the x, y and z directions can be obtained respectively using Fourier analysis, and the results are shown in Figures B.3, B.4 and B.5. It can be seen that the resonance frequency decreases when the crack size increases, at the same time, the amplitude of the resonance frequency increases when the crack size increases. This is due to the stiffness matrix of the blade decreasing with the crack size of the blade. Although the amplitudes of the same resonance frequency in the x, y and z directions are different, the resonance frequency is the same in the x, y and z directions with the same crack size.

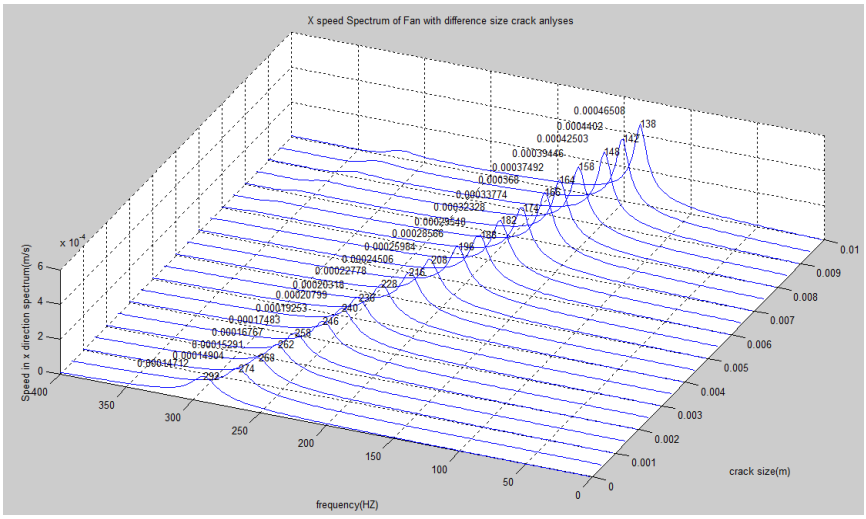

Figure B.3: Vibration velocity in x direction with different crack sizes (0-10mm on blade root)

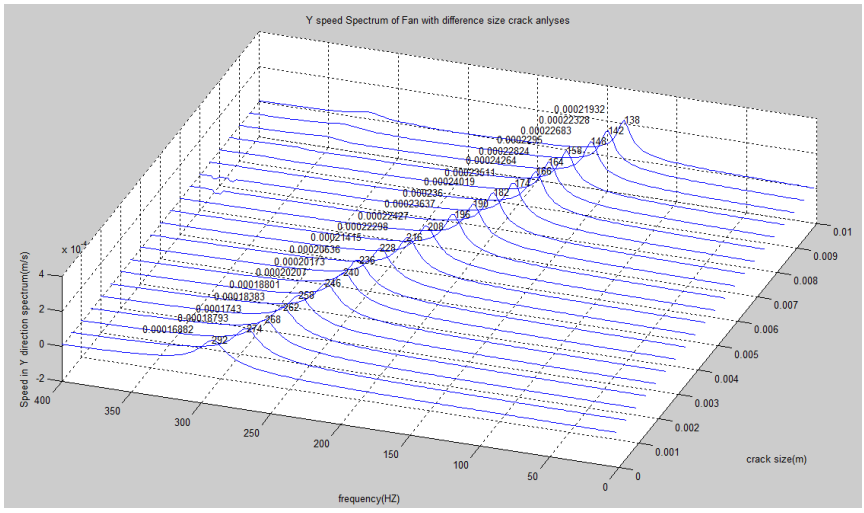

Figure B.4: Vibration velocity in y direction with different crack sizes (0-10mm on blade root)

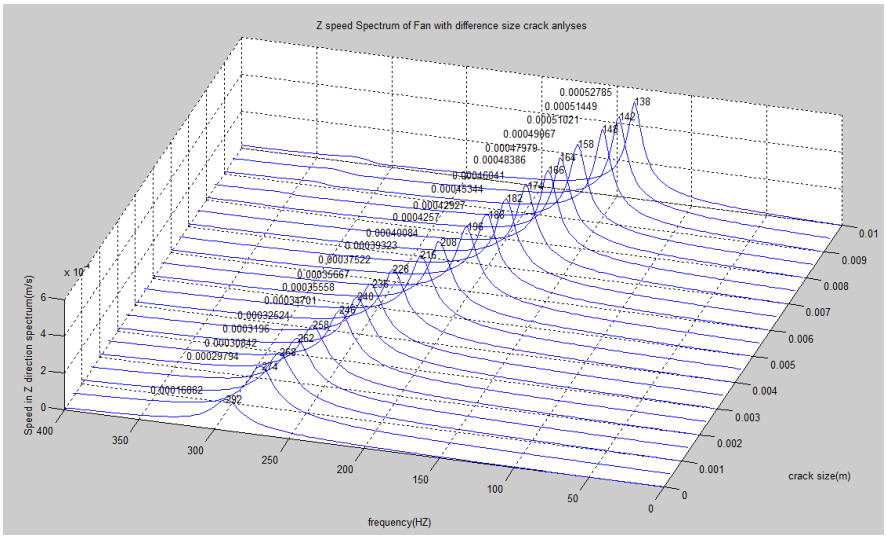

Figure B.5: Vibration velocity in z direction with different crack sizes (0-10mm on blade root)

Table B.1: Simulation results of resonance speed amplitude and frequency in x direction with different crack sizes

Crack Size(mm)	Resonance Frequency(HZ)	Resonance Speed in X direction(m/s)
0	292	0.000147121
0.5	274	0.000149039
1	268	0.000152906
1.5	262	0.000167671
2	258	0.000174826
2.5	246	0.000192528
3	240	0.000207988
3.5	236	0.000203176
4	228	0.000227778
4.5	216	0.00024506
5	208	0.000259845
5.5	196	0.000285656
6	188	0.00029548
6.5	182	0.000323
7	176	0.00033511
7.5	166	0.000368004
8	164	0.00037492
8.5	158	0.000394465
9	148	0.000425034
9.5	142	0.000440201
10	138	0.000465082

Table B.2: Simulation results of resonance speed amplitude and frequency in y direction with different crack sizes

Crack Size(mm)	Resonance Frequency(HZ)	Resonance Speed in Y direction(m/s)
0	292	0.000168819
0.5	274	0.000187928
1	268	0.000174298
1.5	262	0.000183828
2	258	0.000188013
2.5	246	0.000202073
3	240	0.000206358
3.5	236	0.000201732
4	228	0.000214152
4.5	216	0.000398902
5	208	0.000224275
5.5	196	0.00023637
6	188	0.000229884
6.5	182	0.00024
7	176	0.000232875
7.5	166	0.000242642
8	164	0.000228238
8.5	158	0.000229502
9	148	0.000226831
9.5	142	0.00022328
10	138	0.000219319

Table B.3: Simulation results of resonance speed amplitude and frequency in z direction with different crack sizes

Crack Size(mm)	Resonance Frequency(HZ)	Resonance Speed in Z direction(m/s)
0	292	0.000290841
0.5	274	0.000297941
1	268	0.000308423
1.5	262	0.000319598
2	258	0.000325235
2.5	246	0.000347008
3	240	0.000355578
3.5	236	0.000356666
4	228	0.000375219
4.5	216	0.000393226
5	208	0.000400842
5.5	196	0.000425698
6	188	0.000429266
6.5	182	0.000453
7	176	0.000456426
7.5	166	0.000483862
8	164	0.000479789
8.5	158	0.000490669
9	148	0.000510207
9.5	142	0.000514494
10	138	0.000527848

From Table B.1 to Table B**.3**, it can be seen that the resonance frequency decreases as the crack size in the blade increases. However, the power spectrum of the velocity in the x direction does not gradually increase at each crack size as it is a general assumption that the speed spectrum increases when crack size increases. Therefore, prediction of crack size cannot be dependent on the spectrum amplitude, but on the resonance frequency shifting.

B.3 Experimental measurement approach

Figure B.6 shows the experimental setup of the fan's air flow induction vibration on the Guzik spin stand [10]. A Lodestar DC power supply 8102A drives the blow fan to full speed, and air will be blown to the top experimental fan, which has a difference-sized crack. A Polytec CLV3000 three dimensional Laser Doppler vibrometer (3D-LDV) and HP 35670A dynamic signal analyzer (DSA) are employed to measure the velocity power spectrum of a point on the cracked fan blade. The distance between the measured point and the axis of the fan is 100mm.

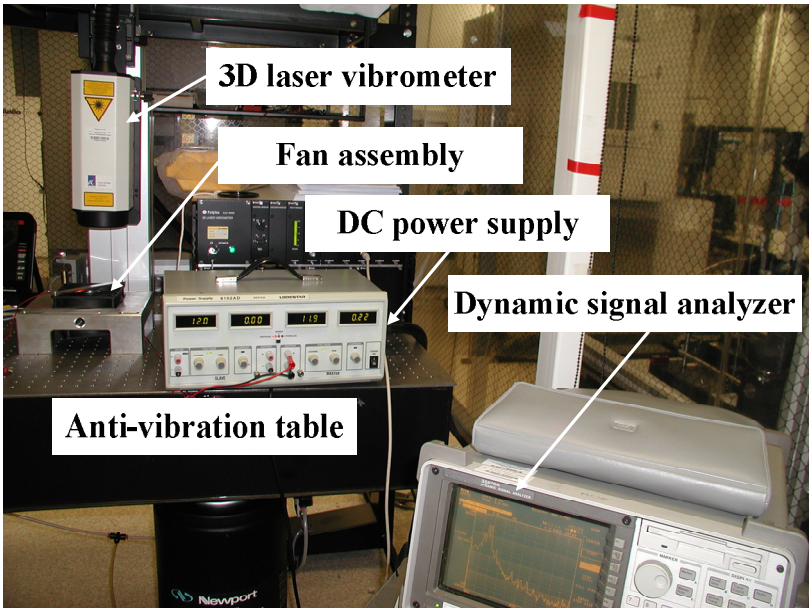

Figure B.6: Experimental setup of air-induction vibration measurement

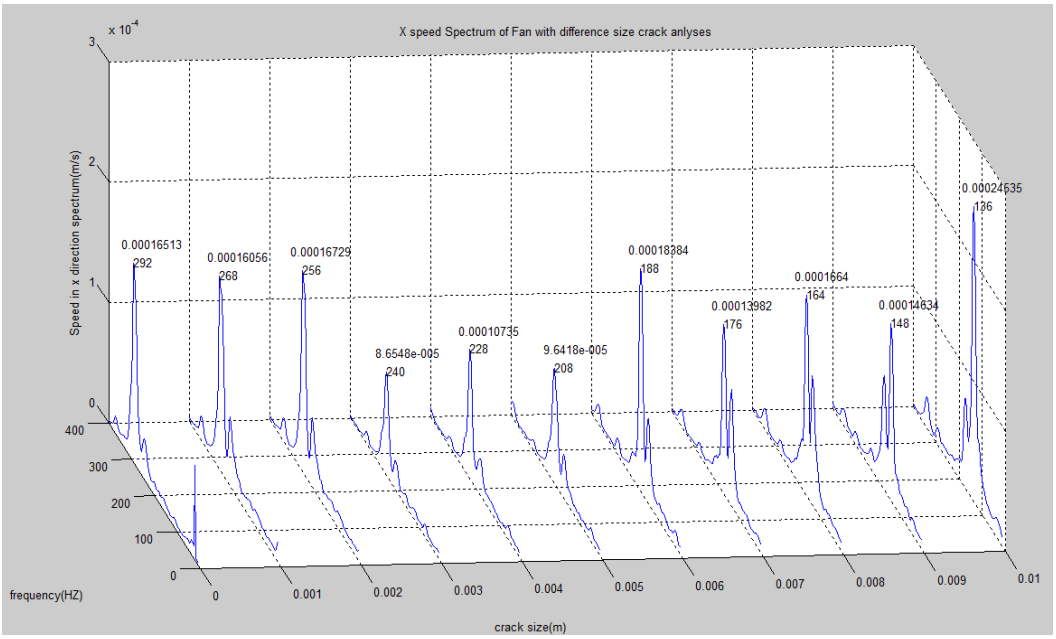

Figure B.7: Experimental results of speed Spectrum in x direction with different crack sizes on blade (0-10mm on blade root)

The experiments were processed with the 3D-LDV to verify the analysis results. Figures B.7, B.8 and B.9 show the x, y and z directions velocity spectrums of the blade with difference crack sizes, respectively.

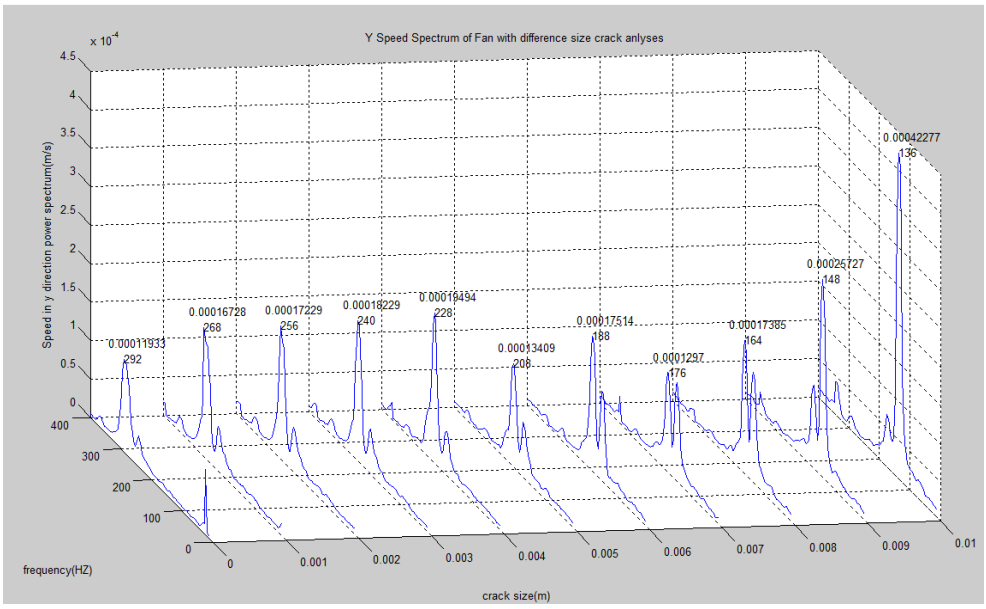

Figure B.8: Experimental results of speed Spectrum in y direction with different crack sizes on blade (0-10mm on blade root)

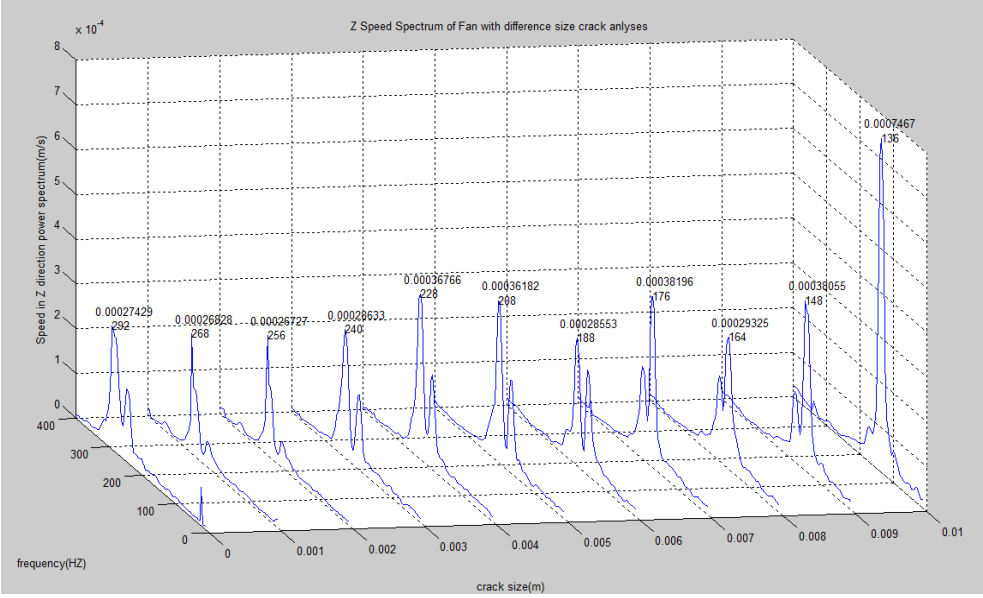

Figure B.9: Experimental results of speed Spectrum in z direction with different crack sizes on blade (0-10mm on blade root)

Table B.4: Experimental results of resonance speed amplitude and frequency in x direction with different crack sizes

Crack Size(mm)	Resonance Frequency(HZ)	Resonance Speed in X direction(m/s)
0	292	0.00016513
1	268	0.00016056
2	256	0.00016729
3	236	0.000086548
4	228	0.00010735
5	208	0.000096418
6	188	0.00018384
7	176	0.00013982
8	164	0.0001664
9	148	0.00014634
10	136	0.00024535

The experimental resonance speed and frequency in the x, y and z directions with different crack sizes can be obtained from Figures B.7, B.8 and B.9, and are also listed in Table B.4, B.5 and B.6. It can be observed that the experimental frequency results in Figures B.7, B.8 and B.9 and are listed in Table B.4, B.5 and B.6 are

agreeable with the simulation frequency results in Figures B.3, B.4 and B.5 and Tables B.1, B.2 and B.3. However, the speed spectrum is not consistent in both simulation and the experimental results.

Table B.5: Experimental results of resonance speed amplitude and frequency in y direction with different crack sizes

Crack Size(mm)	Resonance Frequency(HZ)	Resonance Speed in Y direction(m/s)
0	292	0.00011933
1	268	0.00016728
2	256	0.00017229
3	236	0.00018229
4	228	0.00019494
5	208	0.00013409
6	188	0.00017514
7	176	0.0001297
8	164	0.00017385
9	148	0.00025727
10	136	0.00042277

Table B.6: Experimental results of resonance speed amplitude and frequency in z direction with different crack sizes

Crack Size(mm)	Resonance Frequency(HZ)	Resonance Speed in Z direction(m/s)
0	292	0.00027429
1	268	0.00026828
2	256	0.00026727
3	236	0.00028633
4	228	0.00036766
5	208	0.00036182
6	188	0.00028553
7	176	0.00038196
8	164	0.00029325
9	148	0.00038055
10	136	0.0007467

Although the amplitudes of the measurement signal differ from the simulation results, the frequency changes in the experimental data are well-matched with the simulation

results. Therefore, we can use the frequency shift to detect the crack on the rotor blades, and predict crack size using simulation results.

B.4 Conclusions

In Appendix B, blade cracks are studied in detail. Blade cracks between 1 and 10 mm are analyzed in the simulation model and real blade. The resonance frequencies with different crack sizes are calculated in the simulation model and it can be seen that the resonance frequency decreases as crack size increases, due to the decreasing stiffness matrix of the blade. A novel methodology is used in the experimental setup. In order to focus the layer beams of 3D-LDV on the blade, the testing blade is fixed, and the other electrical fan of the same size and type is used to blow the air to simulate the excitation force of the blade. This is similar to the principle of testing airplanes using air tunnels. It can be observed that the simulation results agree very well with experimental results. The crack size on the blade is accurately predicted using the vibration signal. The vibration induced by cracked blade is related to crack size and not relate to motor pole and slot number and the rotating speed, the cracked blade faulty frequency pattern is also different with those of UMPs and MU fault when the cracked blade is excited by external Sources. Therefore, the MU and UMPs fault diagnosis platform developed in the Chapter 7 is valid when the motor is under this load fault condition.

BIBLIOGRAPHY

[1] S. J. Salon, "Finite element analysis of electric machinery" Computer Applications in Power, IEEE, vol. 3, no. 2, pp. 29- 32, 1990.

[2] http://www.toshiba-elevator.co.jp/elv/infoeng/technology/tec07.jsp

[3] Yinglei Xu, Qun-zhan Li, Liyan Zhang, Qingan Ma, "Development of permanent magnet synchronous motor for electric vehicle", Sustainable Power Generation and Supply, 2009. SUPERGEN '09. International Conference on 6-7, April, 2009. pp.1-5,2009.

[4] http://mathworld.wolfram.com/FastFourierTransform.html.

[5] A. J. Kassab, C. A. Brebbia, E. A. Divo&S.Hernandez, "Fluid Structure Interaction VI", WIT press 2011.

[6] A. Muszynska, "Rotordynamics", Taylor & Francis, 1st edition, 2005.

[7] G. N. D. S. Sudhakar and A. S. Sekhar, "Identification of unbalance in a rotor bearing system," Journal of Sound and Vibration, vol. 330, no. 10, pp. 2299–2313, 2011.

[8] D. G. Huang, "Characteristics of torsional vibrations of a shaft with unbalance", Journal of sound and vibration, vol. 308, pp. 692-698. 2007.

[9] C. Concari, C. Tassoni, A. Toscani," A New Method to Discern Mechanical Unbalances from Rotor Faults in Induction Machines", XIX International Conference on Electrical Machines - ICEM 2010, Rome. 2010.

[10] Arun Kr.Jalan, A. R. Mohanty, “Model based fault diagnosis of a rotor–bearing system for misalignment and unbalance under steady-state condition”, Journal of Sound and Vibration, vol. 327, pp. 604–622, 2009.

[11] H. Kim, "On-line mechanical unbalance estimation for permanent magnet synchronous machine drives", IET Electr. Power Appl, vol. 3, no.3, pp. 178-186, 2009.

[12] I. Y. Shen, "Recent vibration issues in computer hard disk drives", Journal of Magnetism and Magnetic Materials vol. 209, no. 1, pp. 6-9. 2000.

[13] T. Jintanawan, I. Y. Shen, K. Tanaka,” Vibration analysis of fluid dynamic bearing spindles with rotating-shaft design”, IEEE Transactions on Magnetics, vol. 37, no. 2, pp. 799 – 804, 2001.

[14] T. L. Wu, I. Y. Shen, F. Okamoto, T. Asada,” Vibration of 1.8-In HDD Spindle Motors at Various Ambient Temperatures”, Asia-Pacific Magnetic Recording Conference, pp. 1 – 2, 2006.

[15] J. Yoon, I. Y. Shen,” A numerical study on rotating-shaft spindles with nonlinear fluid dynamic bearings”, Asia-Pacific Magnetic Recording Conference, 2004, pp.34 – 35, 2004.

[16] J. Y. Shen, C. W. Tseng, I. Y. Shen, ”Vibration of rotating disk/spindle systems with flexible housing/stator assemblies”, Journal of Sound and Vibration, vol. 271, pp. 725–756, 2004.

[17] J. Fisher-Hinnen, “Dynamo design”. Van Nostrand, 1899.

[18] R. C. Robinson, "The calculation of unbalanced magnetic pull in synchronous and induction motors". AIEE Transactions, vol. 62, pp. 620-624. 1943.

[19] N. R. Garrigan, W. L. Soong, C. M. Stephens, A. Storace, T. A. Lipo, "Radial force characteristics of a switched reluctance machine". Industry Applications Conference, Thirty - fourth IAS Annual Meeting, October 3-7, vol. 4, pp. 2250-2258, 1999.

[20] K. P. Kovacs, "Two-pole induction-motor vibrations caused by homopolar alternating fluxes". IEEE Transactions on Power Apparatus and Systems, vol. 96, no. 4, pp. 1105-1108, 1977.

[21] R. Belmans, A. Vandenput, W. Geysen,"Determination of the parameters of the radial vibrations of large electric motors". Symposium on Electromechanics and Industrial Electronics Applied to Manufacturing Processes, pp. 113-119, 1985.

[22] U. Werner,"Theoretical analysis of shaft vibrations in two-pole induction machines considering static rotor eccentricity", SPEEDAM 2010 Internation Symposium on Power Electronics, Electrical Drives, Automation and Motion, 2010.

[23] A. Khoobroo, B. Fahimi," Detection of Static Rotor Eccentricity in Permanent Magnet Synchronous Drives using Field Reconstruction Method", in Proc. 2010 IEEE Vehicle Power and Propulsion Conf., pp. 1-7, 2010.

[24] C. Bi, N. L. H. Aung, Q. Jiang, and S. Lin," Influence of Rotor Eccentricity to Unbalanced-Magnetic-Pull in PM Synchronous Motor", ICEMS2006.

[25] B. A. T. Iamamura, Y. Le Menach, A.Tounzi, N.Sadowski, E.Guillot, "Study of Synchronous Generator eccentricities using analytical approach and FEM", in 2010 XIX Electrical Machine(ICEM) Conf., pp. 1-6,2010.

[26] M. V. K.Chari, P. P. Silvester, "Finite elements in electrical and magnetic field problems", J. Wiley & Sons, New York 1980.

[27] M. Chari, A. Konrad, M. Palmo, J. D'Angelo, "Three-dimensional vector potential analysis for machine field problems". IEEE Trans. on Magnetics, vol. 18, no. 2, pp. 436-446, 1982.

[28] C. G. C. Neves, R.Carlson, N.Sadowski, J.P.A.Bastos, N.S.Soeiro, S.N.Y.Gerges, "Vibrational behavior of switched reluctance motors by simulation and experimental procedures". IEEE Trans. On Energy Conversion, vol. 34, no. 5, pp. 3158-3161. 1998.

[29] C. Bi, Q. Jiang, S. Lin,"Unbalanced-magnetic-pull induced by the EM structure of PM spindle motor", Electrical Machines and Systems, ICEMS 2005 Proceedings of the Eighth international conference, vol. 1, pp.183-187, 2005.

[30] C. Bi, N. L. H. Aung, Q. Jiang, S. Lin, "Unbalanced-magnetic-pull induced by driver current in PM-BLDC motor operation", ICEMS, pp.780-785,2007.

[31] H. Nejjari and M. Benbouzid, “Monitoring and Diagnosis of Induction Motors Electrical Faults Using a Current Park’s Vector Pattern Learning Approach”, IEEE Transactions on Industry Applications - IEEE Trans. On Induction Applications, vol. 36, no. 3, pp. 730-735, 2000.

[32] L. El Menzhi and A. Saad, “Induction Motor Electrical Fault Diagnosis Using Voltage Spectrum of an Auxiliary Winding”, Electrical Insulation, ISEI 2008. Conference Record of the 2008 IEEE International Symposium, pp. 620-623, 2008.

[33] R. Bayir, “Condition Monitoring and Fault Diagnosis of Serial Wound Starter Motor with Learning vector Quantization Network”, Journal of Applied Sciences vol. 8, no. 18, pp.3148-3156, 2008.

[34] P. Dietl, "Damping and stiffness characteristics of rolling element bearings". PhD thesis, Technical University of Vienna, Austria, 1997.

[35] D. A. Glasgow and H. D. Nelson, "Stability analysis of rotor-bearing systems using component mode synthesis". Trans. of the ASME, Journal of Mechanical Design, vol.102, pp.352-359, 1980.

[36] P. K. Gupta, "Dynamics of rolling element bearings" part III: Ball bearing analysis & part IV: Ball bearing results. ASME Journal of Lubrication Technology, vol. 101, no. 3, pp.312-326. 1979.

[37] R. T. W. M. Hendrikx, G. C. V. Nijen, and P. Dietl, "Vibrations in household appliances with rolling element bearings". Proc. ISMA23 Noise and Vibration Engineering, vol. 3, pp.1537-1544. 1998.

[38] L. D. Meyer, F. F.Ahlgren, and B.Weichbrodt, "An analytical model for ball bearing vibrations to predict vibration response due to distributed defects". Journal of Mechanical Design, vol.102, no. 2, pp.205-210, 1980.

[39] Arun Kr. Jalan, A. R. Mohanty, “Model based fault diagnosis of a rotor–bearing system for misalignment and unbalance under steady-state condition”, Journal of Sound and Vibration vol.327, no.5, pp.604–622, 2009.

[40] S. Rajagopalan, W. le Roux, T. G. Habetler, and R. G. Harley,” Dynamic Eccentricity and Demagnetized Rotor Magnet Detection in Trapezoidal Flux (Brushless DC) Motors Operating Under Different Load Conditions”, IEEE Trans. On Power Electronics, vol. 22, no. 5, 2007.

[41] F. Gu , Y. Shao , N. Huc, A. Naid , A. D. Ball, ”Electrical motor current signal analysis using a modified bispectrum for fault diagnosis of downstream mechanical equipment”, Mechanical Systems and Signal Processing 25 (2011) 360-372 estimation for permanent magnet synchronous machine drives”, IET Electr. Power Appl., vol. 3, no.3, pp. 178-186, 2009.

[42] S. Rajagopalan, T .G. Habetler , R. G. Harley, J. M. Aller, and J. A. Restrepo , "Diagnosis of Rotor Faults in Brushless DC (BLDC) Motors Operating Under Non-Stationary Conditions Using Windowed Fourier Ridges", vol.1, IAS 2005.

[43] I.Y. Shen, “Vibration of Rotationally Periodic Structures”, Journal of Sound and Vibration", vol. 172, no. 4, pp. 459-470, 1994.

[44] Z. Hameeda, Y.S. Honga, "Condition monitoring and fault detection of wind turbines and related algorithms: A review", renewable and sustainable energy reviews, vol. 13, no.1, pp. 1-39, 2009.

[45] B. W. Huang, J. H. Kuang, "Variation in the stability of a rotating blade disk with a local crack defect", Journal of Sound and Vibration, vol. 294, no.3, pp. 486–502, 2006

[46] Y. J. Chiu, S. C. Huang, "The influence on coupling vibration of a rotor system due to a mistuned blade length", International Journal of Mechanical Sciences, vol.49, no. 4, pp.522–532, 2007.

[47] B. W. Huang, "Effect of number of blades distribution of cracks on vibration localization in a cracked pre-twisted blade system", International Journal of Mechanical Sciences, vol.48, no.1, pp. 1-10, 2006.

[48] X. Fang, J. Tang, E. Jordan and K. D. Murphy "Crack induced vibration localization in simplified blade-disk structures", Journal of sound and vibration, vol. 291, no.2, pp.395-418, 2006.

[49] N. Roy, R. Ganguli, "Helicopter rotor blade frequency evolution with damage growth and signal processing", Journal of sound and vibration, vol.283, no.4, pp. 821-851, 2005.

[50] J. H. Kuang and B. W. Huang, "The effect of blade crack on mode localization in rotating bladed disks", Journal of sound and vibration, vol.227, pp. 85-103, 1999.

[51] C. C. Chang, L. W. Chen, "Damage detection of cracked thick rotating blades by spatial wavelet based approach", Applied Acoustics, vol. 65, no.11, pp.1095-1111, 2004.

[52] S. Kumer, N. Roy, R. Ganguli, "Monitoring low cycle fatigue damage in turbine blade using vibration characteristics", mechanical systems and signal processing, vol. 21,no. 1, pp. 480-501, 2007.

[53] R. Parker, "Acoustic resonances and blade vibration in axial flow compressors", Journal of sound and vibration, vol. 92, no. 4, pp.529-539, 1984.

[54] J. Srinivas, B .S .N. Murthy, S. H. Yang, "Damage prediction of rotating blades using displacement residuals", Journal of sound and vibration, vol.316, no. 1, pp. 25-31, 2008.

[55] K. Matsuoka, S. Obata, H. Kita, and F. Toujou, "Development of FDB Spindle Motors for HDD Use", IEEE Trans. On Magnetics, vol. 37, no. 2, 2001.

[56] I. Y. Shen, E. M. Ladd, W. Yang, “Estimating Bearing Coefficients of Fluid-Dynamic Bearing Spindle Motors: A Theoretical Treatment and Feasibility Study”, IEEE Trans. On Magnetics, vol. 47, no.7, pp.1918 – 1922, 2011.

[57] J. S. Park, I.Y. Shen, C.-P.R Ku,” Experimental and theoretical studies of fluid-dynamic bearing (FDB) spindles with rotating-shaft design”, Magnetics Conference, 2002. INTERMAG Europe 2002, 2002.

[58] I. Y. Shen, E. M. Ladd, "Estimating bearing coefficients of fluid-dynamic spindle motors using sub-resonant frequency response", APMRC, 2010 Digest, pp. 1 – 2, 2010.

[59] I.Y.Shen, M. J. Liu, G. Feng, L. C. Wee, W. Z. Lin, E. H. Ong, " Extraction of bearing coefficients of fluid-dynamic bearing spindle motors", APMRC, 2012 Digest, pp. 1 – 2, 2012.

[60] Clarence W. de Silva. "Vibration and Shock Handbook", Taylor & Francis Group, LLC 2005.

[61] F. Ishibashi, K. Kamimoto, T. Hayashi, S. Noda and K. ltomi, "Natural frequency of stator core of small induction", IEE Proc.-Electr. Power Appl., vol. 150, no. 2. pp. 210-214, 2003.

[62] L. Bouzek," Natural Frequency of Stator Core of Asynchronous Machine", Mechatronica, 201, 14th International Symposium, pp.13-15, 2011.

[63] http://www.nbcgroup.co.uk/bearings.aspx?PageID=40

[64] R. Krishnan, "Permanent Magnet Synchronous and Brushless DC Motor Drives ", Taylor & Francis Group, an informa business, 2010.

[65] E. Madenci I. Guven, "The Finite Element Method and Application in Engineering Using ANSYS", Springer 2005.

[66] N. Bianchi. Electrical Machine Analysis Using Finite Elements. Taylor & Francis Group, 2005.

[67] M. Yilmaz, P. T. Krein, "Capabilities of finite element analysis and magnetic equivalent circuits for electrical machine analysis".

[68] R. Fotouhi, "Dynamic analysis of very flexible beams", Journal of Sound and Vibration, vol. 305, no. 3, pp. 521-533, 2009.

[69] S. Putter, H. Manor, "Natural frequencies of radial rotating beams", Journal of Sound and Vibration, vol. 56, pp. 175–185, 1978.

AUTHOR'S PUBLICATIONS

Patents

[1] **Yinquan Yu**, Chao BI, Quan Jiang, "Apparatus to Spindle motor with clamping structure", DSI Ref.No: FY12/0247/DDS, IPOS . Ref.No: 2013031026/130503/TMFSL/7719.

[2] Quan Jiang, **Yinquan Yu**, Chao BI, Song Lin, " Apparatus to measure quality of motor coil PCBs", Ref.No: FY12/0249/DDS, IPOS . Ref.No: 2013031026/130520/TMHAS/1909.

[3] Quan Jiang, Song Lin, Chao BI, **Yinquan Yu**, "Fluid Dynamic Bearing Flying Height Measurement with A Single Sensor and An Integrated Motor Controller", Ref.No: FY12/0265/DDS, ETPL . Ref.No: DSI/Z/07694 (TD)

Journal Papers

[1] **Yinquan Yu**, Chao BI, Hla Nu Phyu, Quan Jiang, Song Lin, Nay Lin Htun Aung, A.Al.Mamun, "Incline Unbalanced Magnetic Pull induced by Misalignment Rotor in PMSM," IEEE Trans. On Magnetics, VOL.49, NO 6. JUNE 2013, p2709-2714.

[2] **Yinquan Yu**, Chao BI, Quan Jiang, Song Lin, Hla Nu Phyu, Nay Lin Htun Aung, A.Al.Mamun, "Vibration Study and Classification of Rotor Faults in PM Synchronous Motor," Microsystem Technologies 2014, DOI 10.1007/s00542-014-2206-8.

[3] Nay Lin Htun Aung, Chao BI, A.Al.Mamun, Soh cheng Su, **Yinquan Yu** "A Demodulation Technique for Spindle Rotor Position Detection with Resolver," IEEE Trans. On Magnetics.

[4] Chao BI, Quan Jiang, Soh cheng Su, , Hla Nu Phyu, **Yinquan Yu**, Nay Lin Htun Aung, Song Lin, "Influence of Neutral Line to The Optimal Drive Current of PMAC motor", IEEE Trans. On Magnetics, VOL.49, NO 6. JUNE 2013, p2483-2488.

Conference Papers

[1] **Yinquan Yu**, Chao BI, Quan Jiang, Song Lin, Hla Nu Phyu, Nay Lin Htun Aung, A.Al.Mamun, "Aanlytical and Numerical Study on Rotor Faults in PM Synchronous Motor," Information Storage and Processing Systems Conference (ISPS2013), Santa Clara, California, USA, 24th-25th JUNE, 2013.

[2] **Yinquan Yu**, Chao BI, Quan Jiang, Song Lin, Nay Lin Htun Aung, A.Al.Mamun, "Vibration Study and Classification of Rotor Faults in PM Synchronous Motor," Information Storage and Processing Systems Conference (ISPS2013), Santa Clara, California, USA, 24th-25th JUNE, 2013.

[3] **Yinquan Yu**, Chao BI, Hla Nu Phyu, Quan Jiang, Song Lin, Nay Lin Htun Aung, A.Al.Mamun, "3D influence of Unbalanced Magnetic Pull induced by Misalignment Rotor in PMSM," Aisa-Pacific Magnetic Recording Conference (APMRC2012), 31 Oct-2Nov, 2012.

[4] **YinQuan Yu**, Chao BI, A.Al,Mamun," Diagnosis of Crack of Rotor Blades with Genetic Method", the 9th international Power and Energy Conference (IPEC2010), 27-29 Oct, 2010.

[5] **Y.Q.Yu**, C.W.De Silva, A. N. Poo, Chao Bi, Abdullah Al Mamun and K. K. Tan, "Design Optimization of a Green Environment Liner-less Thermal Head Printer using Genetic Programming and Linear Graphs", the 4th Asia International Symposium on Mechatronics (AISM2010), 15-18, Dec, 2010.

[6] **Yinquan Yu**, Chao BI, Quan Jiang, Song Lin, Nay Lin Htun Aung, A.Al.Mamun, "Natural Frequency of stator core of PM Synchronous Motor," Information Storage and Processing Systems Conference (ISPS2014), Santa Clara, California, USA, 23th-24th JUNE, 2014 (accepted).

[7] Chao Bi; Phyu Nu Hla; **YinQuan Yu**; Cheng Su Soh; Quan Jiang," Influence of axial asymmetrical rotor in PMAC motor operation",Electrical Machines and Systems (ICEMS), 2011 International Conference on 20-23 Aug. 2011. Page(s): 1-5.

[8] J.Q.Mou, L.Martua, **Y.Q.Yu**, Z.M.He, C.L.Du, J.L.Zhang, E.H.Ong, "Structure Health Monitoring Using PZT Transducer Network and Lamb Waves", Proc, ASME 44250, Volume 1:Advance in Aerospace Technology 1(January 1, 2010). Doi: 10.1115/IMECE2010-37653

[9] Landong Martua, Yopie Adrianto, **Yu Yinquan**, Lin Wuzhong, Ong EngHong," Active Vibration Supression using Efficient and Robust PZT-Actuated Suspension", 2009 JSME-IIP/ASME-ISPS Joint Conference on Micromechatronics for Information and Precision Equipment, 17-20 Jun, 2009.